جامعة البحرين
المكتبة
LIBRARY
UNIVERSITY OF BAHRAIN

UNIVERSITY OF BAHRAIN

Study of Fluid Flow and Heat Transfer Around a Hemispherical Body

A Thesis Submitted in Partial Fulfillment of the Requirements for the Master's Degree in Mechanical Engineering

Submitted by

Fadhel Abbas Salman Yusuf Ahmed Al-Afoo

Academic Number: 20013012

Supervised by

Dr. Moh'd Nabhan

Associate Professor in Mechanical Engineering
University of Bahrain

Kingdom of Bahrain

June 2014

University of Bahrain
Graduate Studies Council

Thesis Discussion Committee Decision

Student Name: Fadhel Abbas Al-Afoo	Student ID: 20013012
Department: Mechanical Eginneering	College: Engineering
Program: M.Sc in Mechanical Engineering	
Thesis Title: Study of fluid flow and heat transfer around a hemispherical body.	
Supervisor Name: Dr. Moh'd Nabhan	Student GPA: 3.56

The Discussion Committee met on Thursday (day and date) 19/6/14 in Hall no. 14-162 (hall/room no.) /. Upon discussing the student whose details are stated above in public, the discussion committee recommends the following:

The student awarded grade A In the thesis subject Mechanical Engineering

☑ Without making any changes to the thesis
☐ After making the modifications attached with this decision

Discussion Committee Members Approval:

Name	Signature
1. Dr. Moh'd Nabhan (Advisor)	
2. Prof. Teoman Ayhan (Internal Examiner)	
3. WALID CHAKROUN (External Examiner)	

ABSTRACT

The airflow and forced convective heat transfer characteristics over the smooth wall surface of a heated and tilted aluminium hemisphere immersed in a fully developed flow in a sub-sonic wind tunnel have been investigated experimentally and numerically.

The hemispherical model is studied at three different tilt angles, namely; $\alpha = 0°$, $30°$ and $52°$, and inclined vertically to the y-axis. The investigation is performed at air velocities ranging from 5 to 25 m/s, in increments of 5 m/s. An experimental method involved maintaining a constant surface heat flux to the hemisphere by means of power supply and filament heater. K-type thermocouples are used to analyze the flow structure for different regions of flow domain around the front and back surfaces of the model. Obtained results are presented in the form of dimensionless temperatures distribution over front (stream-wise and span-wise) directions, and on the back surface. The total drag and lift forces over the hemisphere are experimentally measured in the tunnel with electronic balance sensors at the test flow velocity. The results of total drag and lift coefficients have shown dependency on the inclination of the hemisphere. The pressures in the wake region downstream of the hemisphere are also measured in the tunnel with electronic manometer bank. The results of wake pressure variations become significant at high Reynolds number, $Re \geq 2.0\times10^5$. A smoke flow visualization technique is also carried out in order to obtain qualitative information concerning the flow field structure adjacent to the model surfaces.

A two dimensional (2D) numerical computational fluid dynamics (CFD) model was adopted to simulate the fluid flow field and heat transfer, and to visualize the flow reversal, separation, horseshoe vortices, and recirculation zone downstream and back surface of the hemisphere and to validate the experimental results. It is shown that the flow characteristics vary on the stream-wise and back surfaces as the flow becomes transitional and unsteady. It is found that as Reynolds number increases, the local Nusselt number over front and back surfaces increases. The local and average Nusselt number shows a strong dependence on the oncoming flow velocity. It is found that the total heat transfer rate over hemisphere surfaces (front and back) is enhanced as the tilt angle, α increases, wherein the increase was found to be about (6% ~ 8.3%) and (5% ~ 9%) in comparison to that in $\alpha = 0°$ and $30°$, respectively. A comparison between obtained experimental and numerical total average Nusselt number over entire surfaces of the hemisphere is carried out, and the results are closely match namely at higher range of Reynolds number, between $2.0\times10^5 \leq Re \leq 2.5\times10^5$. The results obtained in numerical simulations are also validated by comparing with the published correlations.

DEDICATION

I dedicate my dissertation work to my father and mother, without them this could not have been possible

ACKNOWLEDGMENTS

I would like to express my gratitude and thanks to my thesis supervisor Dr. Moh'd Nabhan for his great support, guidance and assistance in the thesis work. I would also like to thank the laboratory technician Mr. Ebrahim Faqihi who provided me with all facilities in the laboratory to complete the project successfully.

Very special thanks go to my family for their constant support and motivations provided for me to reach to where I am today.

TABLE OF CONTENTS

Subject	Page
THESIS DISCUSSION COMMITTEE DECISION	i
ABSTRACT	ii
DEDICATION	iii
ACKNOWLEDGMENTS	iv
TABLE OF CONTENTS	v
LIST OF TABLES	viii
LIST OF FIGURES	ix
LIST OF APPENDICES	xv
NOMENCLATURE	xvi
CHAPTER 1: INTRODUCTION	
CHAPTER 1: INTRODUCTION	2
1.1 Literature Review	2
1.1.1 Aerodynamic Flow Characteristics	2
1.1.2 Heat Transfer Characteristics	5
1.2 Overview of Literature	6
1.3 Organization of the Thesis	7
1.4 Aim of Research	8
CHAPTER 2: THEORY AND COMPUTATIONAL SIMULATION	
2.1 Force Analysis on the Hemispherical Model	11
2.1.1 Analysis of total Drag & Lift Coefficients on a Hemisphere at $\alpha = 0°$	12
2.1.2 Analysis of total Drag & Lift Coefficients on a Hemisphere at $\alpha > 0°$	16
2.2 Fluid Flow and Heat Transfer Analysis	19
2.2.1 The Hemispherical Model	19
2.2.2 Governing Equations in Steady State Heating	22
2.2.3 Boundary Conditions in Steady State Heating	23
2.2.4 Evaluation of Heat Transfer	24
2.2.5 Numerical Computation and Meshing	25
2.2.6 Basic Overview of the $k - \varepsilon$ Turbulence Model	29
CHAPTER 3: EXPERIMENTAL APPARATUS AND PROCEDURES	
3.1 Introduction	34

3.2	Experimental Apparatus	40
3.2.1	The Preparation of Model	40
3.2.2	Wind Tunnel Setup	45
3.2.2.1	Electrical Interface Console	45
3.2.2.2	Electronic Manometer Bank	46
3.2.2.3	Lift and Drag Electronic Balance Device	48
3.2.2.4	Wake Survey Rake	50
3.2.3	Control System and Data Acquisition Software	51
3.2.3.1	Hardware and Software Control System	51
3.2.3.2	Power Supply System	54
3.3	Experimental Procedure and Uncertainty	56
3.4	Flow Visualization System	65
CHAPTER 4: RESULTS AND DISCUSSIONS		
4.1	Experimental Results	69
4.1.1	Drag and Lift Coefficient	69
4.1.2	Temperature Distribution Over Hemisphere Surface	72
4.1.2.1	Stream-wise Direction	72
4.1.2.2	Span-wise Direction	75
4.1.2.3	Back Surface of the Hemisphere	79
4.1.3	Wake Pressure Measurements	82
4.1.4	Experimental Average Nusselt Number	86
4.2	Numerical Results	89
4.2.1	Mean Surface Pressure Coefficient	89
4.2.2	Shear Stress	99
4.2.3	Local Nusselt Number	102
4.2.3.1	Stream-wise Direction	102
4.2.3.2	Back Surface of the Hemisphere	105
4.2.4	Average Nusselt Number	108
4.2.5	Velocity Contour	113
4.2.6	Validation of Numerical Results	122
4.2.7	Comparison of Numerical and Experimental Average Nusselt Number	124
CHAPTER 5: CONCLUSIONS AND RECOMMENDATIONS		
5.1	Conclusions	127

5.2 Recommendations	130
5.3 Publication	131
LIST OF REFERENCES	132
APPENDICES	135
ملخص البحث	166

LIST OF TABLES

Number	Table	Page
1	Computational domain information	27
2	Front surface thermocouples tip location angles	42
3	Experimental tests and parameters performed for the hemisphere at a constant heat flux	61
A-1	Uncertainty analysis results at an angle of attack, $\alpha = 0°$ for cold condition tests	145
A-2	Uncertainty analysis results at an angle of attack, $\alpha = 30°$ for cold condition tests	145
A-3	Uncertainty analysis results at an angle of attack, $\alpha = 52°$ for cold condition tests	146
A-4	Uncertainty analysis results for total average Nusselt number, Nu_{Total} at an angle of attack, $\alpha = 0°, 30° \& 52°$ for hot condition tests	146

LIST OF FIGURES

Number	Figure	Page
1	Notation for the integration of pressure and shear stress distributions over a hemispherical body (front and back surfaces) for $\alpha = 0°$	12
2	Forces on an element of the hemispherical body front surface, $\alpha = 0°$, (a) side view, and (b) end view	14
3	Notation for the integration of pressure and shear stress distributions over a hemispherical body (front and back surfaces) for $\alpha > 0°$	17
4	Forces on an element of hemispherical body front surface, $\alpha > 0°$	18
5	(3-D) three dimensional schematic of a hemispherical model during forced convection	20
6	(2-D) Cross sectional schematic of the computational domain for the flow around a hemisphere in stream-wise direction, for hemisphere tilt angle $\alpha = 0°$	21
7	Computational domain of unstructured quadrilateral grid arrangements for the hemisphere at three orientations (a) 0°, (b) 30°, (c) 52°	32
8	Working section velocity profile upstream and downstream from the hemispherical model installed at $\alpha = 0°$ (hot condition)	36
9	Hemisphere examined at three different tilt angles (α) in the tunnel working section (a) $\alpha = 0°$, (b) $\alpha = 30°$and (c) $\alpha = 52°$	37
10	Schematic of the hemispherical model positioned at ($\alpha = 0°$) tilt angle in the test tunnel working section with reference coordinates system	39
11	Experimental control system utilized for the heating of the hemisphere surfaces, the measurements of local temperatures over the hemisphere front & back surfaces, drag & lift forces and pressures in the wake region	39

Number	Figure	Page
12	(a) Front surface of an aluminum hemispherical model and (b) back surface (disc)	40
13	Arrangement of thermocouples slots locations (a) front surface stream-wise direction (b) front surface span-wise direction and (c) back surface	42
14	Hemisphere front surface stream-wise & span-wise arrangements in the tunnel working section	43
15	Preparation steps of hemisphere for hot condition experiments, (a) filament heater, (b) bonding of the heating element & thermocouples into internal surfaces of hemisphere & disc, (c) bonding of back disc to the hemisphere body, (d) final assembly arrangement	44
16	Wind tunnel experimental setup assembly	45
17	IFD7 Electrical Interface console	46
18	Static pressure sensor	47
19	Wind tunnel software mimic diagram screen	48
20	Electronic manometer bank	48
21	Measurements of rotation, lift and drag forces by (a) Electronic balance device, (b) device and hemisphere assembly mounted in the working section, (c) stainless steel rod tightened through hemisphere base	50
22	Wake survey rake, (a) stainless steel tubes arrangement (b) survey rake mounting position in the tunnel section	51
23	(a) PC to control wind tunnel fan speed, measure lift and drag forces, rotation of hemisphere, tunnel working section static head pressure, hemisphere downstream head pressures, (b) Laptop to monitor and record temperature distributions on the hemisphere surfaces. (c) Thermocouple Data Logger (TC-08) to measure the temperatures readings from the K-type Thermocouples	54
24	Temperature measurements data acquisition software screen	54

Number	Figure	Page
25	Power supply FARNELL DC utilized for the heat input to the hemisphere surfaces through filament heater	55
26	Thermocouples & filament heater coils connections pass through rear roof tapping	58
27	Hemisphere positioned at three tilt angles (a) $\alpha = 0°$, (b) $\alpha = 30°$, (c) $\alpha = 52°$	64
28	Flow visualization apparatus (a) smoke generator (b) smoke probe, and (c) hand light	66
29	Wind tunnel working section covered with black sheets paper (a) front and top walls, (b) back wall with small access for fluid flow monitoring	67
30	Comparison of total drag coefficient for hemisphere in cold and hot conditions at different Reynolds numbers with hemisphere tilt angles, ($\alpha = 0°$, $\alpha = 30°$, $\alpha = 52°$)	70
31	Comparison of lift coefficient for hemisphere in cold condition at different Reynolds numbers with tilt angles, ($\alpha = 0°$, $\alpha = 30°$, $\alpha = 52°$)	71
32	Frontal hemisphere stream-wise dimensionless temperature variations at $\alpha = 0°$ hemisphere tilt angle	73
33	Frontal hemisphere stream-wise dimensionless temperature variations at $\alpha = 30°$ hemisphere tilt angle	74
34	Frontal hemisphere stream-wise dimensionless temperature variations at $\alpha = 52°$ hemisphere tilt angle	75
35	Frontal hemisphere span-wise dimensionless temperature variations at $\alpha = 0°$ hemisphere tilt angle	76
36	Frontal hemisphere span-wise dimensionless temperature variations at $\alpha = 30°$ hemisphere tilt angle	77
37	Frontal hemisphere span-wise dimensionless temperature variations at $\alpha = 52°$ hemisphere tilt angle	78
38	Hemisphere back end dimensionless temperature variations for hemisphere tilt angle $\alpha = 0°$	80

Number	Figure	Page
39	Hemisphere back end dimensionless temperature variations for hemisphere tilt angle $\alpha = 30°$	81
40	Hemisphere back end dimensionless temperature variations for hemisphere tilt angle $\alpha = 52°$	82
41	Dimensionless wake pressure variations with hemisphere tilt angle ($\alpha = 0°$)	83
42	Dimensionless wake pressure variations with hemisphere tilt angle ($\alpha = 30°$)	85
43	Dimensionless wake pressure variations with hemisphere tilt angle ($\alpha = 52°$)	86
44	Experimental variations of total average Nusselt number, $Nu_{(Total)}$ with Reynolds number of the hemisphere surfaces (front and back) for three different tilt angle ($\alpha = 0°$, $\alpha = 30°$ and $\alpha = 52°$)	88
45	Pressure coefficient variations, *Cp* along hemisphere stream-wise front surface at $\alpha = 0°$	90
46	Velocity vectors on the trailing edge at Re = 2.5×10^5 for $\alpha = 0°$	90
47	Smoke generated flow visualization around hemisphere at $\alpha = 0°$ taken from two views (a) side, (b) front	91
48	Pressure coefficient variations, Cp along hemisphere stream-wise front surface at $\alpha = 30°$	93
49	Velocity vectors over hemisphere (a) trailing edge, and (b) leading edge at $Re = 2.5\times10^5$ for tilt angle $\alpha = 30°$	94
50	Smoke generated flow visualization around hemisphere showing separation flow on the trailing surface, taken from two views for tilt angle $\alpha = 30°$	95
51	Pressure coefficient variations, Cp along hemisphere stream-wise front surface at $\alpha = 52°$	97
52	Velocity vectors over hemisphere (a) trailing edge, and (b) leading edge at $Re = 2.5\times10^5$ for tilt angle $\alpha = 52°$	98

Number	Figure	Page
53	Smoke generated flow visualization around hemisphere showing separation flow on the trailing surface, for tilt angle $\alpha = 52°$	98
54	Shear stress variations, τ_{wf} along hemisphere stream-wise front surface at $\alpha = 0°$	99
55	Shear stress variations, τ_{wf} along hemisphere stream-wise front surface at $\alpha = 30°$	100
56	Shear stress variations, τ_{wf} along hemisphere back surface at $\alpha = 52°$	101
57	Local Nusselt number variations along hemisphere stream-wise front surface at $\alpha = 0°$	103
58	Local Nusselt number variations along hemisphere stream-wise front surface at $\alpha = 30°$	104
59	Local Nusselt number variations along hemisphere stream-wise front surface at $\alpha = 52°$	105
60	Local Nusselt number variations along hemisphere back surface at $\alpha = 0°$	106
61	Local Nusselt number variations along hemisphere back surface at $\alpha = 30°$	107
62	Local Nusselt number variations along hemisphere back surface at $\alpha = 52°$	108
63	Variations of average Nusselt number, Nu_f with Reynolds number of the hemisphere stream-wise direction of front surface for three different orientations ($\alpha = 0°$, $\alpha = 30°$ and $\alpha = 52°$)	109
64	Correlation between stream-wise average Nusselt number, Nu_f and Reynolds number at different hemisphere tilt angle ($\alpha = 0°$, $\alpha = 30°$ and $\alpha = 52°$)	111
65	Variations of average Nusselt number, Nu_b with Reynolds number of the hemisphere back surface for three different orientations ($\alpha = 0°$, $\alpha = 30°$ and $\alpha = 52°$)	112

Number	Figure	Page
66	Variations of total average Nusselt number with Reynolds number over hemisphere front and back surface for three different orientations ($\alpha = 0°$, $\alpha = 30°$ and $\alpha = 52°$)	112
67	Velocity magnitude contours plot at various Reynolds number (a-e) for hemisphere positioned at $\alpha = 0°$ tilt angle	117
68	Velocity magnitude contours plot at various Reynolds number (a-e) for hemisphere positioned at $\alpha = 30°$ tilt angle	119
69	Velocity magnitude contours plot at various Reynolds number (a-e) for hemisphere positioned at $\alpha = 52°$ tilt angle	121
70	Numerical average Nusselt number over front surface compared with (Drake & Backer, 1952), (Ahmed & Yovanovich, 1994) and (Achenbach, 1978) for different Reynolds number at hemisphere tilt angle $\alpha = 0°$	123
71	Comparison between numerical and experimental total average Nusselt number over hemisphere (front and back) for different Reynolds number at hemisphere tilt angle $\alpha = 0°$, $\alpha = 30°$ and $\alpha = 52°$	125
C-1	Free convection flow in the annular space between hemisphere internal surface and filament heater	150

LIST OF APPENDICES

Number	Appendix
(A)	UNCERTAINTY ANALYSIS
(B)	CONVERSION FROM LINEAR LOCATION TO ANGULAR LOCATION FOR STREAM-WISE SURFACE
(C)	HEAT TRANSFER LOSSES CALCULATIONS THROUGH THE HEMISPHERICAL MODEL
(D)	PUBLICATION PAPER IN THE JOURNAL OF INTERNATIONAL SCIENCE AND TECHNOLOGY CONFERENCE (ISTEC)

NOMENCLATURE

A_f	Hemisphere front surface area, m^2
A_b	Hemisphere back surface area, m^2
C_D	Drag Coefficient, $(F_D/0.5\rho V_\infty^2 A)$
$C_{D,f}$	Friction or viscous drag Coefficient, Eq.(1)
$C_{D,p}$	Pressure drag Coefficient, Eq.(1)
C_L	Lift Coefficient, $(F_L/0.5\rho V_\infty^2 A)$
C_P	Pressure Coefficient, $(P - P_\infty/0.5\rho V_\infty^2 A)$
D	Hemisphere diameter, m^2
F_D	Drag force exerted on the hemisphere, N
F_L	Lift force, N
Δh	Differential head, mm
$h_{\theta,\phi}$	Local convection heat transfer coefficient at front surface, $W/m^2.K$
$h_{x,y}$	Local convection heat transfer coefficient at back surface, $W/m^2.K$
$\overline{h_{\theta,\phi}}$	Average convection heat transfer coefficient at front surface, $W/m^2.K$
$\overline{h_{x,y}}$	Average convection heat transfer coefficient at back surface, $W/m^2.K$
k	Thermal conductivity of air, $W/m.K$
$Nu_{\theta,\phi}$	Local Nusselt number at front surface of the hemisphere, $h_{\theta,\phi}D/k$
$Nu_{x,y}$	Local Nusselt number at back surface of the hemisphere, $h_{x,y}D/k$
$\overline{Nu_f}$	Average Nusselt number at front surface of the hemisphere, $\overline{h_{\theta,\phi}}D/k$
$\overline{Nu_b}$	Average Nusselt number at back surface of the hemisphere, $\overline{h_{x,y}}D/k$
P	Pressure, Pa
P_∞	Atmospheric pressure, Pa
P_s	Static pressure (differential pressure), Pa
P_{wake}	Local wake pressure behind hemisphere, Pa
Pr	Prandtl number, ν/α
q_f	Average heat flux at front surface of the hemisphere, W/m^2
q_b	Average heat flux at back surface of the hemisphere, W/m^2
$q_{\theta,\phi}$	Local heat flux at front surface of the hemisphere, W/m^2
$q_{x,y}$	Local heat flux at back surface of the hemisphere, W/m^2

Re	Reynolds number in the tunnel working section, $\rho V_\infty L/\mu$
Re_D	Reynolds number based on hemisphere diameter, $\rho V_\infty D/\mu$
r_b	Radius of the hemisphere base, m
T_∞	Temperature of the fluid at the inlet of wind tunnel, $°C$
T_s	Temperature at the surfaces of the hemisphere, $°C$
t	Time, s
V_∞	Uniform free air stream velocity, m/s
υ_x	Velocity components in the x-direction, m/s
υ_y	Velocity components in the y-direction, m/s
x	Coordinate along x-axis, m
y	Coordinate along y-axis, m
z	Coordinate along z-axis, m
$(\partial u/\partial y)_s$	Velocity gradient on the surface, s^{-1}
$(\partial T/\partial y)_s$	Thermal boundary layer temperature gradient, $°C/m$
Greek Symbols:	
α	Hemisphere inclination to the vertical y-axis
θ	Angular location on the hemisphere stream-wise direction (meridian angle)
ϕ	Angular location on the hemisphere span-wise direction (azimuthal angle)
μ	Dynamic viscosity of air, $kg/m.s$
ν	Kinematic viscosity, m^2/s
ρ	Density of air flow, kg/m^3
ρ_w	Density of water, kg/m^3
α_f	Thermal diffusivity of air, $[k/C_p\rho]$, m^2/s
τ_{wf}	Shear stress along hemisphere front surface, Pa
τ_{wb}	Shear stress along hemisphere back surface, Pa
Abbreviations	
CWT	Constant Wall Temperature
PC	Personal Computer

Chapter 1

Introduction

1.1 Literature Review
1.1.1 Aerodynamic Flow Characteristics
1.1.2 Heat Transfer Characteristics
1.2 Overview of Literature
1.3 Organization of the Thesis
1.4 Aim of Research

CHAPTER 1: INTRODUCTION

The study of aerodynamic flow and heat transfer characteristics over a bluff bodies immersed in a turbulent boundary layer flow have attracted the attention of many investigators in the field of industrial aerodynamics. In particular, the analysis of air flow around three-dimensional bluff body such as hemisphere shapes are valuable for finding pressure distributions over hemisphere surface and determining variation of heat transfer convection coefficient in order to estimate heating and cooling load. However, many engineering applications related to highly curved bodies such as hemispheres occur in the form of domed buildings, aircraft hangers and surface protrusions on air craft, etc. Most of the previous studies have concerned two-dimensional bluff bodies, such as normal plate (Good & Joubert, 1968), (Range Raju et al., 1976), (Castro & Fackrell, 1978) and (Sakamoto et al., 1975), inclined plates (Sakamoto et al., 1977) and semicircular cylinders (Sakamoto et al., 1977). On the other hand, additional complexity arises for curved body such as hemisphere because the location of a separation point cannot be identified purely based on the geometry. This leads to strong dependency of flow field on Reynolds number, boundary layer thickness and the turbulence intensity level of the approaching flow. Several research papers have focused on this subject.

1.1 Literature Review

1.1.1 Aerodynamic Flow Characteristics

For such curved bodies various experimental and numerical studies have been undertaken to determine aerodynamic flow characteristics. The early work of (Maher, 1965) was conducted for a Reynolds number of

about 1.5×10^5 (based on hemisphere diameter) in a thin boundary layer to find the pressure distribution on smooth and rough hemispheres in a wind tunnel. His results show that the minimum mean pressure coefficients for smooth and rough hemispheres are -1.15 and -0.8, respectively. Also reduction in the maximum pressure coefficients occurred because the rough surface promotes turbulent boundary layer over the hemisphere and causes earlier separation over the hemisphere. Consequently, the earlier separation over the hemisphere reduced suction at separation point, but led to more suction overall in the wake and increased drag, also he reported that the drag coefficient becomes invariant when Reynolds number exceeds 1.4×10^6. Other authors extended experiments for different boundary layer and different Reynolds number. (Taylor, 1991), suggests that, when Reynolds exceeds 2.0×10^5 and turbulence intensity exceeds 4 %, the pressure distributions becomes Reynolds number independent. (Ogawa et al., 1991), indicates that for Reynolds numbers ranging from $1.2 \times 10^5 \sim 2.1 \times 10^5$, level of turbulence has little effect upon the mean pressure distribution. (Toy et al., 1983), had experimental investigations about air flow past a hemispherical dome immersed in two kinds of thick turbulent boundary layers of different turbulent intensity and velocity profiles. Their results show that with increase of turbulence intensity in the boundary layer, both separation region and reattachment points moved downstream. (Meroney et al., 2002), conducted numerical simulation, as well as wind tunnel measurements to study flow around single and dual domes in a thick boundary layer. (Manhart, 1998), performed a large eddy simulation to investigate vortex shedding from a hemisphere in a turbulent boundary layer. (Tamura et al., 1990), used numerical simulation to find the unsteady flow filed around a wall mounted hemisphere. (Savory & Toy,

1986), (Savory & Toy, 1986) and (Savory & Toy, 1988), conducted a series of investigations to find the velocity and pressure distribution around the hemisphere and hemisphere cylinders for different incoming velocity and turbulence intensity boundary layer profiles. Recently, (Tavakol et al., 2010), reported a flow regime around a wall mounted hemisphere placed in two different boundary layers (thin and thick) using numerical simulations and hot-film anemometry. They measured velocity distribution at different sections of the flow field; they measured locations of flow separation and reattachment with a hot-film anemometer. And they employed a numerical simulation using RNG $k-\varepsilon$ turbulence model and their results compared with the wind tunnel measurements. They concluded that, the hemisphere located in a thin boundary layer profile has a greater reattachment length downstream of the hemisphere and a closer separation point to the hemisphere apex, (Tavakol & Yaghoubi, 2010) extended their research to study the Reynolds number dependency and the flow structures in the upstream and downstream region of air flow around a surface mounted hemisphere using experimental and numerical themes, they concluded that the flow is highly Reynolds number dependent especially at the reversed flow region formed upstream and downstream of the hemisphere. Their analysis to the flow structure shows that in the span-wise direction the maximum reversed flow occurs at the lower free stream velocity of 5 m/s. They also found that the reattachment length behind the hemisphere is decreases with increasing of incoming free stream velocity. (Cheng & Fu, 2010) carried out wind tunnel tests to investigate the effect of Reynolds number of range ($5.3\times10^4 \leq Re \leq 2.0\times10^6$) on the aerodynamics characteristics of hemispherical dome. They observed that in smooth flow the transition of separation flow occurs in between $Re = 1.8\times10^5$ - 3.0×10^5 and pressure distributions become stable after $Re \geq 3.0\times10^5$, while in turbulent flow the

transition of separation flow occurs at lower $Re < 1.1\times10^5$ and the pressure distributions become Reynolds number independent at $Re = 1.0 - 2.0\times10^5$.

1.1.2 Heat Transfer Characteristics

The bluff bodies are of current interest for use in heat dissipation where heat transfer performance is desired. Furthermore, forced convection heat transfer from isothermal or isoflux external surfaces is an important problem in many engineering applications, such as aeronautic engineer. There are many engineering systems that are modeled using forced convection, such as electronic components on printed circuit boards placed in cabinets, hot-wire anemometers, transformers, heat sinks, thermal spreaders, and heat exchanger design, in addition to many other complex components that need a suitable means of forced convection heat transfer to maintain safe operating temperature. Owing to its many practical engineering applications and scientific interest, the problem of forced convective heat transfer from isothermal and isoflux axi-symmetric curved shapes bluff bodies has been studied extensively, such as spheroids (Beg, 1975), cylinders (Ahmed & Yovanovich, 1970), and discs (Wedkind & Kobus, 1996) using variety of predictive methods as reviewed in (Youvanovich & Vanoverbeke, 1988). The extensive literature for sphere model has been summarized amongst others, by (Ahmed & Yovanovich, 1994), they provided an approximate analytical method based on linearization of the energy equation to develop solution for the forced convection heat transfer from isothermal spheres for all Prandtl numbers and for $Re_D \leq 2 \times 10^5$. (Dhole et al., 2006) used finite volume method to investigate the effects of Reynolds and Prandtl numbers for the range of conditions ($5 \leq Re \leq 200$ and $0.7 \leq \mathrm{Pr} \leq 400$),

respectively, on the heat transfer characteristics of an unconfined sphere for different thermal boundary layer conditions (isothermal and isoflux) on the sphere surface, there results capture well dependence of average Nusselt number on the Reynolds and Prandtl numbers. (Kendoush, 1995) obtained an analytical solution to the forced convection heat and mass transfer across a laminar incompressible boundary layer over the surface of a stationary isothermal sphere, His solution is valid for Pr < 1(for gases) and for laminar flow with $Re > 10^2$. Recently, (Richter & Nikrityuk, 2011), conducted three dimensional calculations of the flow and heat transfer around sphere and non-spherical particles of various shapes in steady state regime. Their work focused on the relation between geometric parameters on the drag and surface averaged Nusselt number, their major finding that the drag coefficient is mainly influenced by the normalized longitudinal length of the geometry and as the geometry shape becomes sphere the higher heat transfer rate is obtained. (Whitaker, 1972) developed a correlation for the average Nusselt number for a sphere in a uniform free-stream for the range of Reynolds numbers as $1 \leq Re \leq 10^5$.

1.2 Overview of Literature

In the aforementioned literature review of the experimental and numerical studies performed for heat transfer and flow characteristic over bluff bodies, it has been observed that most of these researches were dedicated to the flow past a surface mounted hemisphere where its apex pointed to the windward direction (y-axis) due to its extensive applications. However, it can be said that the attempts that have been devoted to analyze the fluid flow over hemispherical body are often not take into account the effect of angle of attacks of the hemisphere submerged freely in the approaching flow. On the other hand, the number

of studies for steady laminar and turbulent forced convection is limited on hemispherical bluff bodies, with most researches restricted to analytical solution carried out by (Lewandowski et al., 1992) and theoretical and experimental study conducted by (Lewandowski et al., 1996), which devoted only for natural convection heat transfer from isothermal hemisphere, while the vast majority of the researches have been dedicated to the spherical geometries in the field of forced convection heat transfer. This encouraged us to examine a different configurations in which the hemisphere apex pointing towards horizontal axis, in addition taking into consideration to vary hemisphere tilt angle to analyze the fluid flow and heat transfer characteristic from the heated surfaces of the hemisphere. Therefore, additional investigation is necessary to distinguish the heat transfer performance over hemisphere surfaces placed in different angle of attacks.

1.3 Organization of the Thesis

The thesis lies in 5 chapters, the chapters are organized as follow:

Chapter 1

This chapter introduces a brief outline of the thesis problems, literature review of the related topics of the problems. In addition, this chapter includes the objective of the thesis and the major contribution in this thesis.

Chapter 2

This chapter highlights the mathematical formulations of drag and lift forces exerted over tilted and un-tilted hemisphere. Also, this chapter describes the theory of heat transfer problem taking into consideration constant heat flux condition over the hemisphere. Moreover, the

numerical scheme chosen in the problem, the problem description and model assumptions are introduced in this chapter.

Chapter 3

This chapter introduces in details the model preparation for the experiments, experimental apparatus and procedures utilized for the experimental investigation, such as, wind tunnel accessories, heating system and data acquisition system. In addition, this chapter describes the flow visualization technique used to capture the flow phenomenon around the obstacle. Also the results of uncertainty analysis for the experimental measurements are explained in this chapter.

Chapter 4

This chapter includes the experimental and numerical results conducted for three different tilt angles of the hemisphere, it also includes a comparison between the results obtained from experiments and numerical, as well as a validation of the numerical results is conducted, wherein the surface average Nusselt number obtained at zero tilt angle in different flow condition are examined against empirical correlations obtained by different researchers.

Chapter 5

This chapter includes the conclusion, recommendations, and suggestion for future work.

1.4 Aim of Research

The aim of this research is to investigate the air flow characteristics around a heated surface of a hemispherical body with constant heat flux and tilted vertically to y-axis at three different angles (0°, 30° and 52° degrees) to the free stream air flow direction inside a sub-sonic wind tunnel. In addition, to study forced convection heat transfer

characteristics in the boundary layer adjacent to the hemisphere surface. Having flow field, drag and lift coefficients, pressure coefficient, heat flux distributions, local Nusselt numbers, recirculation zones, flow separation region, and reattachment locations will be investigated at Reynolds number range $0.5\times10^5 \leq Re \leq 2.5\times10^5$ using experimental measurements and numerical simulations. Based on analyzed results we will be able to distinguish in which configuration and condition could the hemisphere dissipate a comprehensive heat transfer, consequently an optimum condition will be proposed of a suitable fixation tilt angle of the hemisphere in order to enhance heat dissipation from any practical industrial application processes through hemispherical model.

Chapter 2

Theory and Computational Simulation

2.1 Force Analysis on the Hemispherical Model
2.1.1 Analysis of Total Drag & Lift Coefficients on a Hemisphere at $\alpha = 0°$
2.1.2 Analysis of Total Drag & Lift Coefficients on a Hemisphere at $\alpha > 0°$
2.2 Fluid Flow and Heat Transfer Analysis
2.2.1 The Hemispherical Model
2.2.2 Governing Equations in Steady State Heating
2.2.3 Boundary Conditions in Steady State Heating
2.2.4 Evaluation of Heat Transfer
2.2.5 Numerical Computation and Meshing
2.2.6 Basic Overview of the $k - \varepsilon$ Turbulence Model

CHAPTER 2: THEORY AND COMPUTATIONAL SIMULATION

2.1 Force Analysis on the Hemispherical Model

The suspended (3D) three dimensional hemispherical body is immersed in air flow stream of various velocities inside tunnel working section, therefore, the body will experience to forces and to a lesser extent to moments as a result of the flow around its external front and back surfaces. Those forces are generally characterized as a function of body orientation, body geometry and flow conditions. As in this research fluid velocities and hemisphere orientation are variables in order to investigate the changes of forces on the hemisphere body. The common terms used to express those forces are called drag and lift coefficient, C_D and C_L, respectively. However, the development of the common interested term, the drag coefficient, C_D is enhanced by pressure and viscous friction drags over the hemispherical body. The general form of the total drag coefficient of a body is expressed (White, 2003);

$$C_D = C_{D,pressure} + C_{D,skin\ friction} \quad (1)$$

In our research the pressure drag in equation (1) is expected to dominant over the second term the friction drag. Therefore, the pressure drag will be the major contributor that form the total drag, C_D on the hemisphere surface, while, the viscous drag effect is expected to have a minimal contribution since the outer surface of the hemisphere were maintained as smooth surface and of a blunt shape.

The flow around hemisphere as in our model can be considered of less-aerodynamic shape because the boundary layer separation is

expected to occur due to the presence of leading and trailing sharp edges as shown in Figure 1. Moreover for different orientations of the hemisphere to the flow direction, there may also be an enhancement in the pressure difference on the hemisphere surfaces, in other word the difference of the favorable to adverse pressure gradients which could contribute to earlier boundary layer separation which in turn effects on the total drag over the hemispherical body.

2.1.1 Analysis of total Drag & Lift Coefficients on a Hemisphere at ($\alpha = 0^{\circ}$)

Analysis of the pressure and shear wall stress on the front and back surface for hemisphere with zero tilt angle $\alpha = 0°$ to the free stream air velocity V_{∞} is shown in Figure 1, this along with, our experimental and numerical investigations that the hemisphere inclination angle chosen was ($0°, 30°, 52°$), respectively. In the following analysis we will treat three-dimensional hemispherical body to obtain an expression for total drag and lift coefficients.

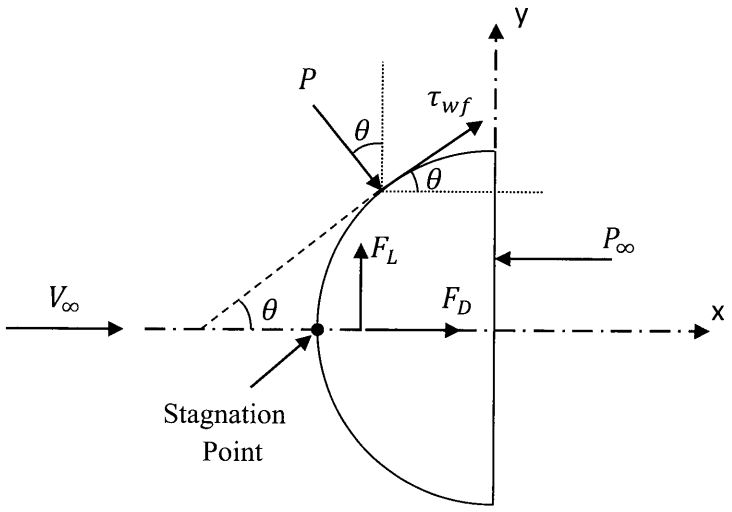


Figure 1: Notation for the integration of pressure and shear stress distributions over a hemispherical body (front and back surfaces) for $\alpha = 0°$

In this case where ($\alpha = 0°$), and along the base of the hemisphere, we assume that the pressure on the surface is atmospheric, $P = P_\infty$, and neglecting the effect of shear stress at the back surface area, A_b of the hemisphere as well. Where it is extremely expected to have a wake region downstream of the hemisphere along back area, so the contribution of the shear stresses due to friction is diminished in this region.

From Figure 2, the drag and lift forces on the shaded strip of surface areas are as follows

$$F_D = P \sin\theta dA_f + \tau_{wf} \cos\theta dA_f - P_\infty . dA_b \tag{2}$$

$$F_L = -P \cos\theta dA_f + \tau_{wf} \sin\theta dA_f \tag{3}$$

The load of the hemisphere is neglected in Eq. (3) as the weight is supported by an extended link in the test section, also at the initial steps of experimental investigation the values of lift and drag forces are set to zeroed which correspond to the weight of the hemisphere on the electronic balance device and with no rearward force on the balance.

The areas utilized in the integration over hemisphere front and back surfaces will be as follows

$$dA_f = 2\pi r_b ds = 2\pi r_b \frac{dr}{\sin\theta} \tag{4}$$

$$dA_b = 2\pi r_b dr \tag{5}$$

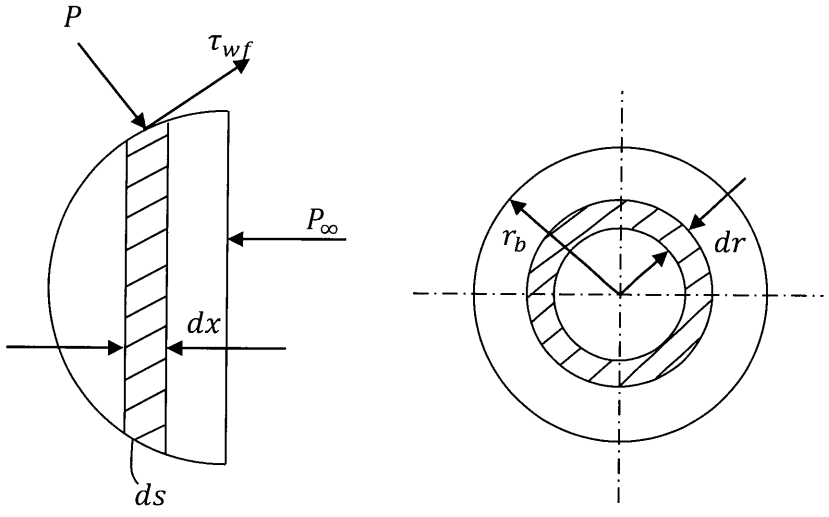
Where, A_b and A_f are the base and front surface areas of the hemisphere, respectively.

The total drag and lift forces due to pressure and shear stress, respectively, acting over the total surface area of the hemisphere are as follow,

$$F_D = \int_0^{r_b} P \sin\theta . dA_f + \int_0^{r_b} \tau_{wf} \cos\theta . dA_f - \int_0^{r_b} P_\infty . dA_b \qquad (6)$$

$$F_L = \int_0^{r_b} -P \cos\theta . dA_f + \int_0^{r_b} \tau_{wf} \sin\theta . dA_f \qquad (7)$$

Where, r_b is the hemisphere base radius. P & P_∞ are the pressure distributions along hemisphere front and back surfaces, respectively. τ_{wf} is the component of shear stress due to viscous flow over the front surface of the body.



(a) (b)

Figure 2: Forces on an element of the hemispherical body front surface, $\alpha = 0°$, (a) side view, and (b) end view

Substituting of surface areas expressions (4 & 5) into Equations (6 & 7), the drag and lift forces will be as follow

$$F_D = \int_0^{r_b} P \sin\theta . 2\pi r_b (dr/\sin\theta) + \int_0^{r_b} \tau_{wf} \cos\theta . 2\pi r_b (dr/\sin\theta) - \int_0^{r_b} P_\infty . 2\pi r_b dr \qquad (8)$$

$$F_L = \int_0^{r_b} -P \cos\theta . 2\pi r_b (dr/\sin\theta) + \int_0^{r_b} \tau_{wf} \sin\theta . 2\pi r_b (dr/\sin\theta) \qquad (9)$$

The Integral of equations (8 & 9) with respect to the base radius r_b, the total drag and lift forces becomes

$$F_D = A_b\left[(P - P_\infty) + \tau_{wf}\cot\theta\right] \tag{10}$$

$$F_L = A_b\left(\tau_{wf} - P\cot\theta\right) \tag{11}$$

Recall from the general form of the drag & lift coefficient of a body (White, 2003)

$$C_D = \frac{F_D}{q_\infty A} \tag{12}$$

$$C_L = \frac{F_L}{q_\infty A} \tag{13}$$

Where q_∞ is the dynamic pressure of the free air stream flow, $q_\infty = \frac{1}{2}\rho V_\infty^2$, and ρ is the air density. A, is the hemisphere projected frontal area used for the measurement of the drag and lift coefficients.

Substituting equations (10 & 11) into equations (12 & 13), therefore the drag and lift coefficients can be written as

$$C_D = \frac{(P - P_\infty) + \tau_{wf}\cot\theta}{q_\infty} \tag{14}$$

$$C_L = \frac{\left(\tau_{wf} - P\cot\theta\right)}{q_\infty} \tag{15}$$

Equations (14 & 15) can be rearranged and, from the definition of a Newtonian fluid where shear stress near a solid wall is defined (White, 2003) as

$$\tau = \mu\left(\frac{\partial u}{\partial y}\right)_s \tag{16}$$

Where, μ is fluid viscosity and the second term is the velocity gradient along y-axis. Wall shear stresses, τ in equation (16) can be analyzed along inclined frontal surface of the hemisphere as shown in Figure 1, and it reduces to

$$\tau_{wf} = \frac{\mu}{\sin\theta} \tag{17}$$

Therefore, substituting equation (17) into equation (14) & (15) gives the final form of total drag and lift coefficients for hemisphere tilted at zero degree to the free stream air flow, C_D and C_L becomes

$$C_D = \frac{(P - P_\infty)(1 - \cos^2\theta) + \mu\cos\theta}{q_\infty(1 - \cos^2\theta)} \tag{18}$$

$$C_L = \frac{\mu - P\cos\theta}{q_\infty \sin\theta} \tag{19}$$

The previous equation (14 and 15) can be rearranged and written in terms of pressure and skin friction coefficients, C_p & C_f, respectively, as follow

$$C_D = C_p + C_f \cot\theta \tag{20}$$

$$C_L = C_f - \frac{P\cot\theta}{q_\infty} \tag{21}$$

2.1.2 Analysis of total Drag & Lift Coefficients on a Hemisphere at ($\alpha > 0^\circ$)

The effect of shear stresses at the back surface area, A_b will be considered for this case, as the hemisphere in this condition is tilted with a certain angle, α to the vertical axis (y) as shown in Figure 3, and as performed in the experimental and numerical investigations for the two cases where α chosen were (30° & 52°). The same analytical procedures used in the previous section are implemented herein in order to obtain an

expression for the total drag and lift coefficients for a tilted hemisphere ($\alpha > 0°$).

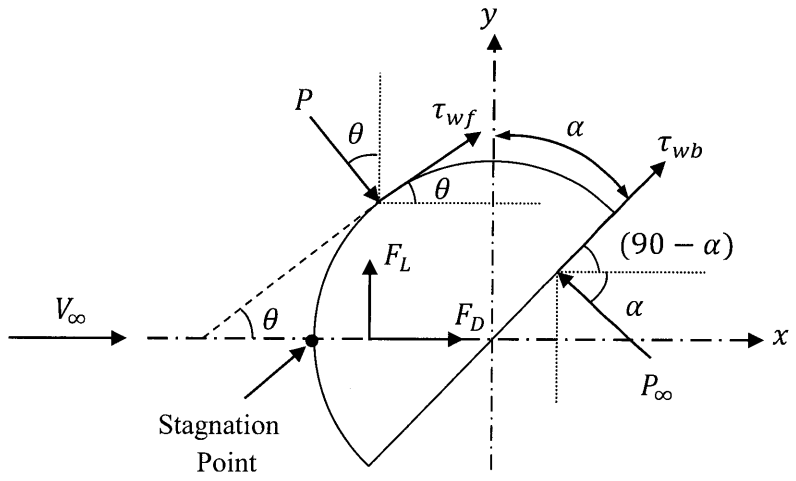


Figure 3: Notation for the integration of pressure and shear stress distributions over a hemispherical body (front and back surfaces) for $\alpha > 0°$

From Figure 4, the drag and lift forces on the shaded strip of surface areas are as follows

$$F_D = \left[P \sin\theta + \tau_{wf} \cos\theta\right] dA_f + \left[-P_\infty \cos\alpha + \tau_{wb} \sin\alpha\right] dA_b \qquad (22)$$

$$F_L = \left[-P \cos\theta + \tau_{wf} \sin\theta\right] dA_f + \left[P_\infty \sin\alpha + \tau_{wb} \cos\alpha\right] dA_b \qquad (23)$$

The areas utilized in the integration over hemisphere front and back surfaces will be as follow

$$dA_f = 2\pi r_b ds \cos\alpha = 2\pi r_b \frac{dr}{\sin\theta} \cos\alpha \qquad (24)$$

$$dA_b = 2\pi r_b dr \cos\alpha \qquad (25)$$

The total drag and lift due to pressure and shear stress acting over the total surface area of the hemisphere, and by substituting the expression of (24 & 25) into equations (22 & 23), the integral of total drag and lift forces will be as follow;

$$F_D = \int_0^{r_b} \left[P \sin\theta + \tau_{wf} \cos\theta\right] 2\pi r_b dr \frac{\cos\alpha}{\sin\theta}$$

$$+ \int_0^{r_b} \left[-P_\infty \cos\alpha + \tau_{wb} \sin\alpha\right] 2\pi r_b dr \cos\alpha \qquad (26)$$

$$F_L = \int_0^{r_b} \left[-P \cos\theta + \tau_{wf} \sin\theta\right] 2\pi r_b dr \frac{\cos\alpha}{\sin\theta}$$

$$+ \int_0^{r_b} \left[P_\infty \sin\alpha + \tau_{wb} \cos\alpha\right] 2\pi r_b dr \cos\alpha \qquad (27)$$

The Integral of equations (26 & 27) with respect to the hemisphere base radius, r_b, the total drag and lift forces become;

$$F_D = A_b \cos\alpha \left(\left[P + \tau_{wf} \cot\theta\right] + \left[-P_\infty \cos\alpha + \tau_{wb} \sin\alpha\right]\right) \qquad (28)$$

$$F_L = A_b \cos\alpha \left(\left[-P \cot\theta + \tau_{wf}\right] + \left[P_\infty \sin\alpha + \tau_{wb} \cos\alpha\right]\right) \qquad (29)$$

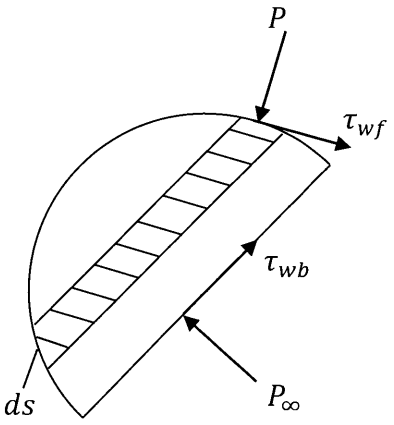


Figure 4: Forces on an element of hemispherical body front surface, $\alpha > 0°$

The wall shear stress, τ in equation (16) is analyzed along back surface area as shown in Figure 3 and it reduces to,

$$\tau_{wb} = \frac{\mu}{\sin(90-\alpha)} \tag{30}$$

Note that the same shear stress τ_{wf} equation (17) for frontal surface is introduced here. Therefore substituting equations (17 and 30) into equation (28 & 29) will have the final form of drag and lift coefficients for tilted hemisphere with an angle, α to the free stream air flow, C_D and C_L becomes

$$C_D = \frac{1}{q_\infty}\left[P - P_\infty \cos\alpha + \mu\left(\frac{\cot\theta}{\sin\theta} + \frac{\sin\alpha}{\sin(90-\alpha)}\right)\right] \tag{31}$$

$$C_L = \frac{1}{q_\infty}\left[P_\infty \sin\alpha - P\cot\theta + \mu\left(\frac{1}{\sin\theta} + \frac{\cos\alpha}{\sin(90-\alpha)}\right)\right] \tag{32}$$

2.2 Fluid Flow and Heat Transfer Analysis

2.2.1 The Hemispherical Model

The hemispherical model studied experimentally in this research is three-dimensional (3D) body subjected to a stream of Newtonian fluid of an incompressible flow in a wind tunnel with uniform air velocities and temperature, V_∞ and T_∞, respectively, as depicted physically by nature in Figure 5. The hemisphere front and back surfaces maintained with uniform constant heat flux, wherein the surfaces temperature, T_s during experimental investigations becomes $(T_s > T_\infty)$. Therefore, the forced bulk flow of air free stream at the inlet boundary of the tunnel past perpendicularly at the top center of the front surface of the hemisphere, and owing to the thermal potential difference, $(T_s - T_\infty)$ the hemisphere dissipate heat from its entire surfaces due to forced convection heat

transfer which satisfying the Newton's law of cooling. Thus, the fluid adjacent to the hot surfaces grows up and formed the thermal boundary layer over hemisphere body. Neglecting the contribution of the heat transfer by radiation from the body, and as the temperatures distributions along the hemisphere surfaces are constant due to constant heat flux, the problem can be reduced and treated to solve only the convection heat transfer around the body, since it is expected that the heat transfer by convection is dominant in this problem. Accordingly, to study heat transfer enhancement from the hemisphere, it is necessary to determine the dissipated energy transferred by convection from the hemisphere surface to the supplied air fluid.

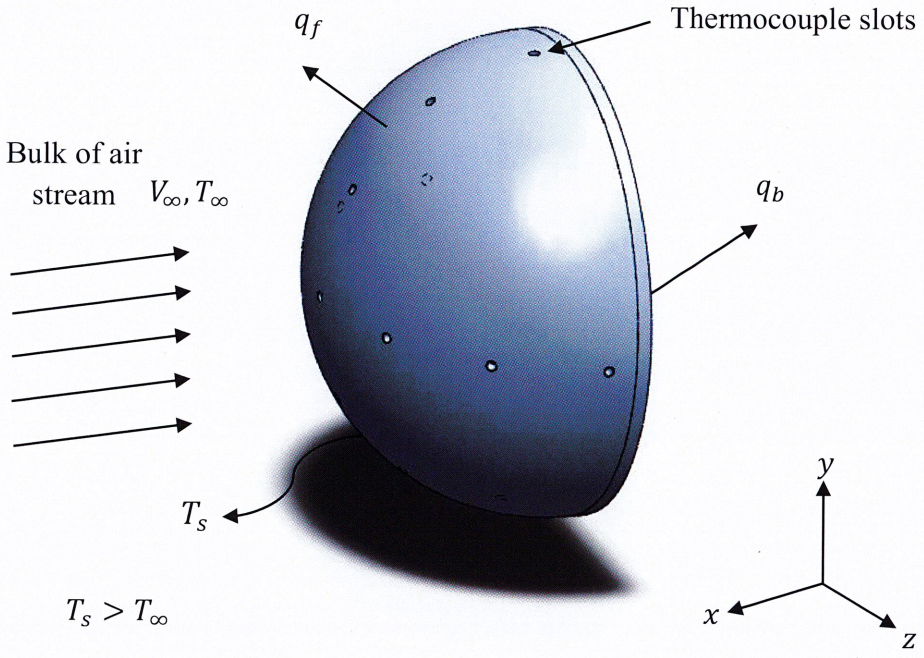


Figure 5: (3-D) three dimensional schematic of a hemispherical model during forced convection

The problem can be simplified by considering the flow around two dimensional (2-D) stream-wise cross sectional view of a hemisphere

subjected to constant heat flux boundary condition at it is surfaces. Figure 6 depicts a (2-D) cross sectional domain of the flow around hemisphere stream-wise direction, which is considered for the numerical calculation and it includes axis used to write the boundary conditions. The revealed orientation is for the hemisphere at zero tilt angle ($\alpha = 0°$) that tilted to the vertical axis, y. The position was changed during numerical and experimental investigations for the other two orientations ($\alpha = 30°, \alpha = 52°$). Therefore, in order to study the heat transfer enhancement among the three conditions.

The following assumptions are used:

1. Incompressible flow, where the density changes are negligible, $\partial\rho/\partial t \approx 0$.
2. Steady, constant fluid properties, $\partial T/\partial t \equiv 0$ (i.e. properties are temperature-independent).
3. Body forces and viscous dissipation energy are ignored in this research.

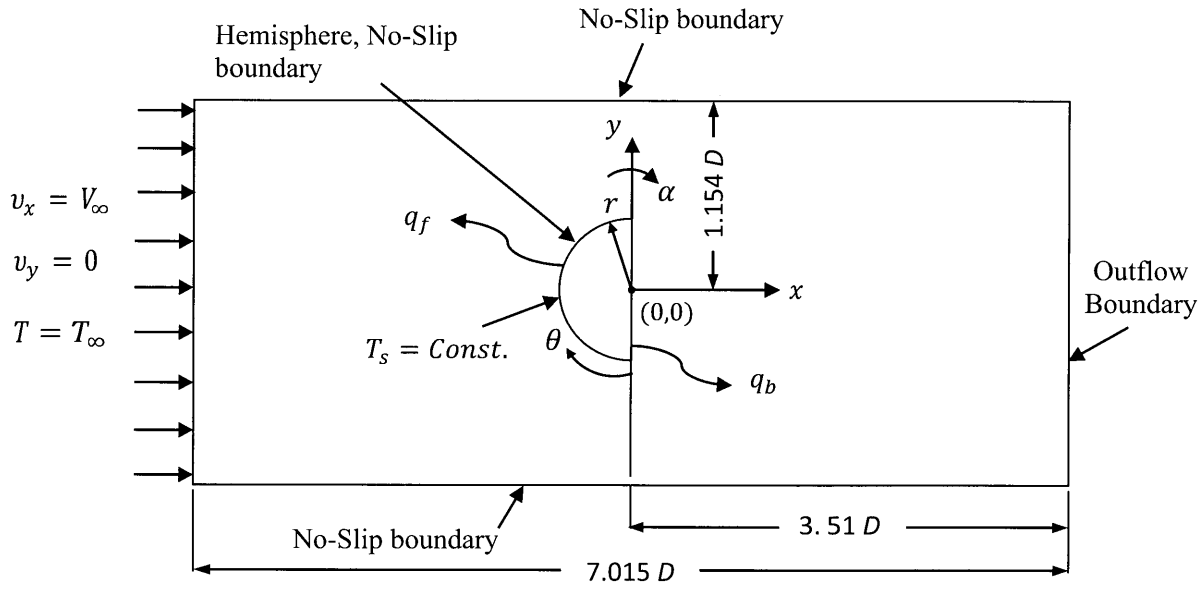


Figure 6: (2-D) Cross sectional schematic of the computational domain for the flow around a hemisphere in stream-wise direction, for hemisphere tilt angle ($\alpha = 0°$)

2.2.2 Governing Equations in Steady State Heating

The flow and heat transfer phenomena in the computational domain described in Figure 6 is governed by the continuity, the Navier-Stokes and the energy equations (White, 2003) which are subjected to the aforementioned assumptions. The (2-D) two dimensional form of the governing equations in the Cartesian coordinate system is considered here to solve the flow past over stream-wise direction of the hemisphere, using Cartesian velocity components in $(x \,\&\, y)$ directions.

Continuity equation:

$$\frac{\partial v_x}{\partial x} + \frac{\partial v_y}{\partial y} = 0 \tag{33}$$

x – Components of momentum equation:

$$v_x \frac{\partial v_x}{\partial x} + v_y \frac{\partial v_x}{\partial y} = -\frac{1}{\rho}\frac{\partial P}{\partial x} + \nu\left(\frac{\partial^2 v_x}{\partial x^2} + \frac{\partial^2 v_x}{\partial y^2}\right) \tag{34}$$

y – Components of momentum equation:

$$v_x \frac{\partial v_y}{\partial x} + v_y \frac{\partial v_y}{\partial y} = -\frac{1}{\rho}\frac{\partial P}{\partial y} + \nu\left(\frac{\partial^2 v_y}{\partial x^2} + \frac{\partial^2 v_y}{\partial y^2}\right) \tag{35}$$

Energy equation:

$$v_x \frac{\partial T}{\partial x} + v_y \frac{\partial T}{\partial y} = \alpha\left(\frac{\partial^2 T}{\partial x^2} + \frac{\partial^2 T}{\partial y^2}\right) \tag{36}$$

In above equations, v_x and v_y are the velocity components in x and y directions, respectively. P is the pressure, and T is the temperature of the fluid. ν and ρ are the kinematic viscosity & the density of air, respectively. Where α is the thermal diffusivity of the fluid.

2.2.3 Boundary Conditions in Steady State Heating

The boundary conditions as shown in Figure 6 can be stated as follows:

At the tunnel inlet boundary: Uniform flow

$$\upsilon_x = V_\infty, \upsilon_y = 0, T = T_\infty, \frac{\partial P}{\partial x} = 0 \tag{37}$$

At the tunnel outlet boundary:

$$\frac{\partial \upsilon_x}{\partial x} = 0, \ \frac{\partial \upsilon_y}{\partial x} = 0, \ \frac{\partial T}{\partial x} = 0, \ P = P_\infty = 0 \ , \ T = T_\infty \tag{38}$$

At the hemisphere front surface: No-slip condition

$(0 \leq \theta \leq \pi)$

$$\upsilon_x = \upsilon_y = 0, \ \frac{\partial T}{\partial x} = 0, \ \frac{\partial P}{\partial y} = 0, \ \frac{\partial \upsilon_x}{\partial x} = 0, T = T_s \tag{39}$$

At the hemisphere back surface: No-slip condition

$(-r \leq y \leq r)$

$$\upsilon_x = \upsilon_y = 0, \ \frac{\partial T}{\partial y} = 0, \ \frac{\partial P}{\partial x} = 0, \ \frac{\partial \upsilon_x}{\partial y} = 0, T = T_s \tag{40}$$

At the top and bottom wall of the tunnel: No-slip condition

$$\upsilon_x = \upsilon_y = 0, \ \frac{\partial T}{\partial y} = 0, \ \frac{\partial P}{\partial y} = 0, \ \frac{\partial \upsilon_x}{\partial x} = 0, T = T_\infty \tag{41}$$

The numerical solution of the governing flow and heat equations (33) – (36) subjected to the aforementioned boundary conditions outlined in equations (37) – (41), have been solved numerically using FLUENT, which then yields the velocity, pressure and temperature fields which in turn are used to obtain the surface pressure coefficient, local Nusselt number and local heat flux, etc.

2.2.4 Evaluation of Heat Transfer

The local heat fluxes transfer at the front and back surfaces of the hemisphere stream-wise direction are evaluated by the following expressions (Incropera & DeWitt, 2002)

$$q_\theta = h_\theta(T_s - T_\infty), \quad (0 \leq \theta \leq \pi) \tag{42}$$

$$q_{x,y} = h_{x,y}(T_s - T_\infty), \quad (-r \leq x, y \leq r) \tag{43}$$

Where q_θ and $q_{x,y}$ are the local heat fluxes per unit area in the front and back surface of the hemisphere, respectively. h_θ and $h_{x,y}$, are the local heat transfer convection coefficients in the front and back surface, respectively. T_s and T_∞, are the temperatures at the hemisphere surface and the incoming fluid, respectively. θ is the stream-wise (meridian angle) angular displacement limits from the leading edge to the trailing edge of the front surface as depicted in Figure 6, x *and* y represent linear locations limits at the back surface of the hemisphere, note that y is considered for un-tilted hemisphere, and x for tilted hemisphere and r is the hemisphere radius.

The average heat transfer coefficients at the front and back surfaces of the hemisphere, therefore, can be determined using the following expressions

$$\bar{h}_{\theta,\phi} = \frac{1}{\pi r}\int_0^\pi h_{\theta,\phi} \sin\theta, \phi d\theta, \phi \tag{44}$$

$$\bar{h}_{x,y} = \frac{1}{D}\int_{-r}^{r} h_{x,y} dx, y \tag{45}$$

The total heat flux transferred from the entire surface of the hemisphere stream-wise cross section due to convection must be equal to the

summation of the averaged values of the local heat fluxes at front and back, q_f & q_b, respectively, according to the following equation

$$q_T = q_f + q_b \tag{46}$$

Where q_f and q_b, are the average value of heat flux at the front and back surfaces, respectively.

The local Nusselt number on the front and back surface of the hemisphere is evaluated by the following expressions (Incropera & DeWitt, 2002)

$$Nu_{\theta,\phi} = \frac{h_{\theta,\phi} D}{k} \tag{47}$$

$$Nu_{x,y} = \frac{h_{x,y} D}{k} \tag{48}$$

Where, D is the hemisphere diameter, and k is the thermal conductivity of air.

The average Nusselt number that characterizes the heat transfer from the hemisphere stream-wise, θ, span-wise, ϕ and back surface to the moving fluid due to forced convection can be calculated by the following expressions

$$\overline{Nu_f} = \frac{\overline{h_{\theta,\phi}} D}{k} \tag{49}$$

$$\overline{Nu_b} = \frac{\overline{h_{x,y}} D}{k} \tag{50}$$

2.2.5 Numerical Computation and Meshing

The governing equations of an incompressible turbulent 2-D flow along with the boundary conditions described above were solved using the finite volume discretization method employed by commercial

FLUENT code version 6.3.26. The numerical simulation is performed to study in more details the flow field, pressure distribution, and heat transfer around an immersed mounted hemisphere. Hereby, the finite volume discretized method involves applying the integral form of the governing equations over a discrete control volume of each cell, thereafter the divergence theorem applied to convert it into a control surface integral around the perimeter of each cell, wherein the discrete values of the variables are evaluated at the center of each cell. The computational domain is divided into small elements of quadrilateral cells and at each element the velocity, pressure, and temperature fields was approximated until convergence accomplished. Numerically, SIMPLE algorithm is used to solve the conservation equations, which uses a relationship between velocity and pressure corrections to impose conservation of mass and to obtain the pressure field, which achieve more efficient single phase implementation for the steady state flow. The method to solve obtained non-linear equations in the Fluent segregated solver was the Guess-Seidel iterative technique as it to allow efficient matrix inversion and its ability to solve non-linear equations with considerably reduced memory requirements.

The mesh generation of the computational domain was performed in GAMBIT program as follows, a scaled dense grids of 300 divisions are employed on both front surface of stream-wise direction and back wall of the hemisphere, so as to adequately capture the variations of the velocity and temperature gradients in the boundary layer developed adjacent to the hemisphere surfaces, moreover separation and recirculation's are also expected to develop in these regions. While the grids away from the hemisphere walls are larger, where the flow is without any considerable variation, therefore at the inlet and outlet boundaries of the computational

domain each was maintained with 100 divisions, while the top and bottom walls each maintained with 200 divisions. Figure 7 shows the grid generated of the computational domain for the numerical simulation of the three configurations of the hemisphere stream-wise direction. The computational domain obtained contained different number of cells at each tilt angle as shown in Table 1. The variations found in these values because we employed an adaption method to refine the grid adjacent to the hemisphere walls in order to accurately resolve the boundary layer which is considered very thin specifically near the front surface of the hemisphere. The process of Adapt-Gradient applied after 1000 of iteration of each test, once adaption completed by which zero number of cells for refinement is achieved, then the iteration proceed for all tests up to 10000 iterations. The solution was converged where the values of the residuals obtained were less than 10^{-6}. A total of fifteen tests were performed numerically through the FLUENT.

Table 1: Computational domain information

Re	0 degree			30 degree			52 degree		
	Cells	Faces	Nodes	Cells	Faces	Nodes	Cells	Faces	Nodes
5.0E04	95864	195338	99474	99386	202622	103236	99554	201570	102016
1.0E05	95864	195338	99474	99053	201920	102876	103376	210228	106852
1.5E05	99227	202461	103234	98969	201755	102786	103490	210347	106857
2.0E05	99056	202069	103013	98972	201752	102780	105380	214549	109169
2.5E05	95864	195338	99474	99782	203550	103768	103025	209247	106222

The numerical simulation is linked to the experimental investigations performed on the tilted hemisphere in the wind tunnel at the three different angles 0°, 30° and 52°, in order to determine heat transfer and fluid flow over the hemisphere subjected to various air stream velocities. The numerical investigation conducted is 2-D Cartesian coordinate system performed over stream-wise direction of the

hemisphere in the computational domain. The computational domain origin is located in the center of back wall of the hemisphere. The necessary domain dimensions are measured with respect to the hemisphere diameter, D. wherein the actual dimensions of the tunnel test in meter are (x, y, z) = (0.45, 0.15, 0.15). The boundary conditions required for the computational domain are three types used to compute the flow filed. The inflow and outflow boundaries were specified as velocity inlet and pressure outlet, respectively, the top and bottom boundaries of the computational domain and hemisphere front and back surfaces were specified as wall. The inflow boundary conditions were chosen to match the velocity and turbulence profiles measured during the wind tunnel experiments. Outflow boundary conditions were chosen to maintain constant longitudinal rate of change of all dependent variables (constant slope).

The 2-D problem was modeled in the Fluent using two isothermal conditions, no slip planes in contact with the fluid regions for top and bottom walls boundaries of simulated tunnel, while the obstacle thermal boundary condition (front stream-wise and back surfaces) was specified as a constant heat flux in contact with the fluid. A uniform inlet velocity and free stream temperature, V_∞ and T_∞, respectively, were applied at the inlet upstream boundary domain, also an atmospheric zero pressure and ambient air temperature at the outlet downstream boundary were specified, and T_∞ at the top and bottom wall boundaries were applied. The obstacle walls (front and back) and ambient air temperatures were set to $T_S = 70\ °C$ and $T_\infty = 20\ °C$, respectively, while the obstacle constant heat flux was set to 3039.7 W/m^2. The properties of air flow were evaluated at a mean film temperature of $45\ °C$ (318 K). The hemisphere

is mounted on a hanger and its distance from the inlet plane in the computational domain is about 3.5 D.

2.2.6 Basic Overview of the $k-\varepsilon$ Turbulence Model

The $k-\varepsilon$ turbulence model is used to take into consideration the enhanced mixing and diffusion caused by the unsteady turbulent eddies in the flow domain. As many of the flow conditions in the present experiments were involved transitions to turbulent flow specifically over the obstacle near downstream region. So to solve the turbulent flow this model is required. When using $k-\varepsilon$ turbulence model the steady Navier-Stokes equation is replaced by Reynolds-averaged Navier-Stokes (RANS) equation. In which, the $k-\varepsilon$ model uses (RANS) equation for momentum in order to determine the transport of turbulent fluctuations i.e. fluctuations of velocity components. These new unknowns are solved by $k-\varepsilon$ model.

In $k-\varepsilon$ turbulence model, two transport equations are solved simultaneously with the equations of mass, momentum and energy to solve the turbulent fluctuations, which also allows the two equations to account the effects of convection and diffusion of turbulent energy. These two equations solve for the turbulent kinetic energy, k, and the turbulent dissipation rate, ε. These transport equations is given by (Fluent, 2006),

$$\frac{\partial}{\partial t}(\rho k)+\frac{\partial}{\partial x_i}(\rho k u_i)=\frac{\partial}{\partial x_j}\left[\left(\mu+\frac{\mu_t}{\sigma_k}\right)\frac{\partial k}{\partial x_j}\right]+G_k+G_b-\rho\varepsilon-Y_M+S_k \qquad (51)$$

$$\frac{\partial}{\partial t}(\rho\varepsilon)+\frac{\partial}{\partial x_i}(\rho\varepsilon u_i)$$

$$=\frac{\partial}{\partial x_j}\left[\left(\mu+\frac{\mu_t}{\sigma_\varepsilon}\right)\frac{\partial \varepsilon}{\partial x_j}\right]+C_{1\varepsilon}\frac{\varepsilon}{k}(G_k+C_{3\varepsilon}G_b)-C_{2\varepsilon}\rho\frac{\varepsilon^2}{k}+S_\varepsilon \qquad (52)$$

The turbulent viscosity, μ_t, is computed by combining k and ε as

$$\mu_t = \rho C_\mu \frac{k^2}{\varepsilon} \tag{53}$$

However, the standard $k-\varepsilon$ model doesn't perform well in cases of large adverse pressure gradients, therefore, the Realizable $\kappa-\varepsilon$ Turbulence model, which provides superior performance for flows involving boundary layers under strong adverse pressure gradients, separation, and recirculation, is used to study the numerical computation of the turbulent flow field around the hemisphere. The developed realizable $\kappa-\varepsilon$ model differs from the standard $\kappa-\varepsilon$ model, as the realizable contains a new formulation for the turbulent viscosity, and a new derived transport equation for the dissipation rate, ε. In the realizable $\kappa-\varepsilon$ model, the model satisfies certain mathematical constraints on the Reynolds stresses, consistent with the physics of turbulent flows.

The new derived model for the dissipation rate, ε in the realizable $\kappa-\varepsilon$ model is as follow, (Fluent, 2006),

$$\frac{\partial}{\partial t}(\rho\varepsilon) + \frac{\partial}{\partial x_j}(\rho\varepsilon u_j) =$$

$$\frac{\partial}{\partial x_j}\left[\left(\mu + \frac{\mu_t}{\sigma_\varepsilon}\right)\frac{\partial \varepsilon}{\partial x_j}\right] + \rho C_1 S_\varepsilon - \rho C_2 \frac{\varepsilon^2}{k+\sqrt{\nu\varepsilon}} + C_{1\varepsilon}\frac{\varepsilon}{k} C_{3\varepsilon} G_b + S_\varepsilon \tag{54}$$

Where,

G_k: Generation of turbulence kinetic energy due to the mean velocity gradients.

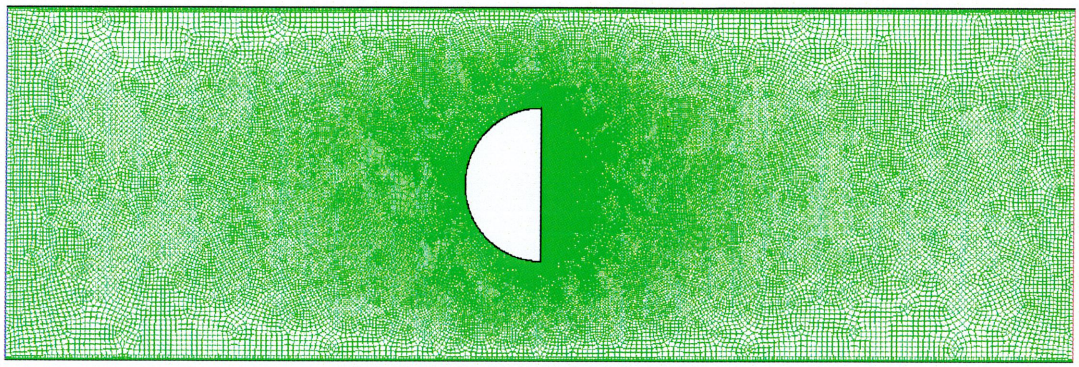
G_b: Generation of turbulence kinetic energy due to buoyancy.

Y_M: Represents the contribution of the fluctuating dilatation in compressible turbulence to the overall dissipation rate.

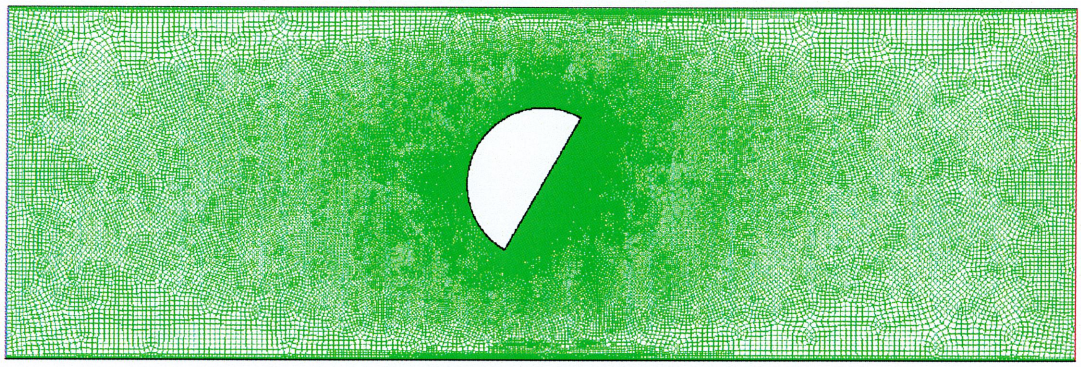
$C_{1\varepsilon}$, $C_{2\varepsilon}$ and $C_{3\varepsilon}$: are constants.

σ_k and σ_ε: are the turbulent Prandtl numbers for κ and ε, respectively.

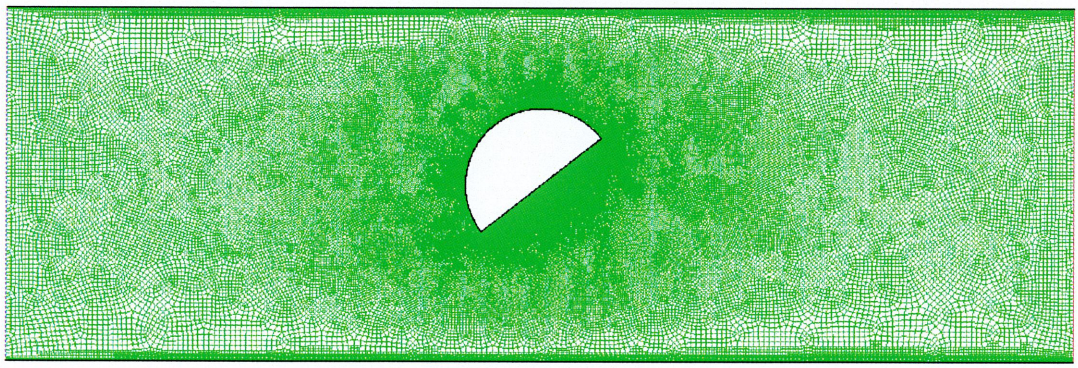
S_k and S_ε: are user-defined source terms.



(a) Tilt angle $\alpha = 0°$



(b) Tilt angle $\alpha = 30°$



(c) Tilt angle $\alpha = 52°$

Figure 7: Computational domain of unstructured quadrilateral grid arrangements for the hemisphere at three orientations (a) 0°, (b) 30°, (c) 52°

Chapter 3

Experimental Apparatus and Procedures

3.1 Introduction
3.2 Experimental Apparatus
3.2.1 The Preparation of Model
3.2.2 Wind Tunnel Setup
3.2.2.1 Electrical Interface Console
3.2.2.2 Electronic Manometer Bank
3.2.2.3 Lift and Drag Electronic Balance Device
3.2.2.4 Wake Survey Rake
3.2.3 Control System and Data Acquisition Software
3.2.3.1 Hardware and Software Control System
3.2.3.2 Power Supply System
3.3 Experimental Procedure and Uncertainty
3.4 Flow Visualization System

CHAPTER 3: EXPERIMENTAL APPARATUS AND PROCEDURES

3.1 Introduction

Experimental investigations conducted on an aluminum hemispherical model to obtain clear representation of the nature of the airflow characteristic, as well as the effectiveness of heat transfer dissipation over the smooth wall surface of heated hemisphere tilted at various angles of attack to the air stream flow and immersed in a fully developed flow in a test wind tunnel. Two conditions were performed on the wall surface of the hemisphere, constant heat flux (hot surface) condition and cold surface condition.

The experiments were performed in a sub-sonic wind tunnel test (ARMFIELD C15-10) located in the Mechanical Engineering Department at the University of Bahrain Fluids Laboratory. The tunnel cross section is a transparent 150 mm square working section with an overall length of 455 mm. Basically, the experiments on the hemispherical model conducted for two different conditions; the initial investigation was carried out for the hemisphere surface maintained at room temperature 20°C "cold condition" i.e. there was no heat input to the hemisphere surface, accordingly no heating element or thermocouples attached to the hemisphere interior portion, the objective of this test is to investigate the airflow characteristic over wall surface of the hemisphere, such as drag & lift forces behavior at different air flow stream velocities and for three different angle of attacks, α. On the same model, the second experimental work carried out on the heated hemisphere with constant heat flux wherein a hot condition maintained over the entire surfaces of

the hemisphere with an average surface temperature of 70 °C, in which an investigation carried to study airflow and heat transfer characteristics for the same inlet air velocities and hemisphere positions performed in cold condition experiments. An intended comparison study conducted between two conditions in terms of the effect of heating surfaces to the lift & drag forces exerted on the hemispherical model.

The experiments were carried out in air, $Pr = 0.707$. Air is drawn in through a variable speed fan located at the discharge end of the tunnel to minimize turbulence inside the working section. A honeycomb type flow straightener and 9.4:1 contraction ratio ensure well developed air flow through working section. The operating range of the fan is nominally 0-32 m/s with no model installed in the working section. The maximum velocity achievable in the test section varies with the model type and the blockage created by the model, 30 m/s was the maximum air inlet velocity with the installation of the hemispherical model in cold condition tests, the blockage developed in this condition created by the hemispherical body and the velocity has been reported to decrease by 6.25 %, where Mach number is (Ma = 0.08). The blockage increases in the hot condition tests as a result of thermocouples and filament heater wires connections to the hemisphere internal hollow cavity, wherein the maximum velocity achieved was 25 m/s, and reduced by around 21.8 % from the design value with no model installed, where Mach number is (Ma = 0.07). The air free stream velocities upstream and downstream of the model were measured with no significant changes, namely 30 m/s and 29.6 m/s (0.6%) for cold condition, and 25 m/s and 24.2 m/s (3.2%) for hot condition. The upstream and downstream velocities were taken at around 200 mm and 150 mm away from the model, respectively, through tapping's hole on the working section roof and using hot-wire

anemometer. And as shown in Figure 8 that elucidates flow uniformity in the working section, and hence the wall interference has no effect. The inlet turbulent intensities were measured and found it lies between 0.032% ~ 1.63%, which corresponds to the inlet velocities range from 5 to 25 m/s, thus as the turbulence intensities are low we assure that the flow at the inlet boundary is uniform and free stream flow is exist.

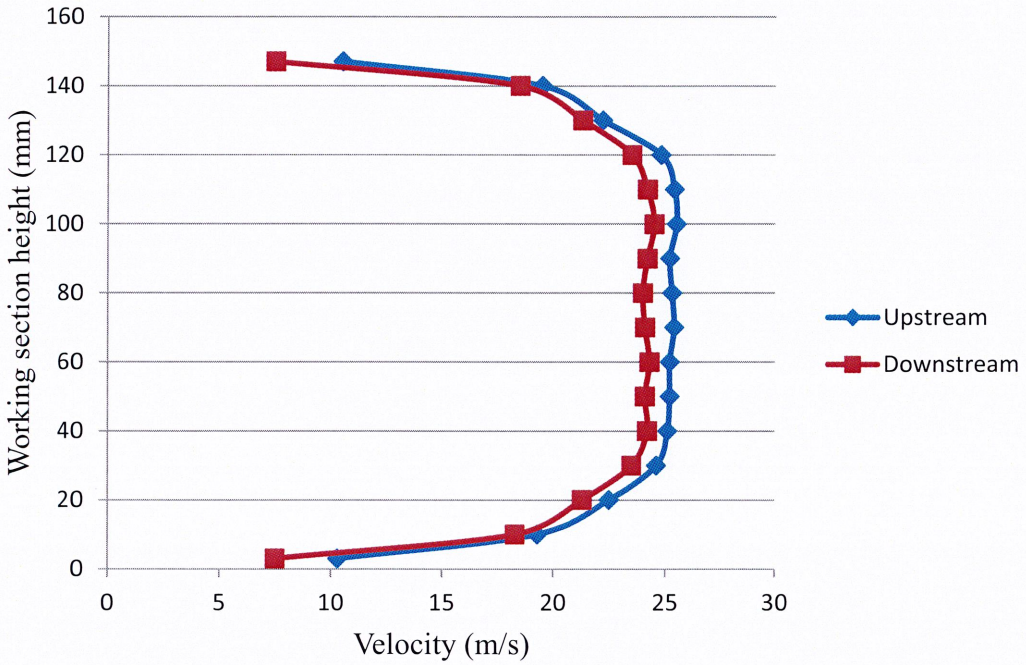


Figure 8: Working section velocity profile upstream and downstream from the hemispherical model installed at $\alpha = 0°$ (hot condition)

Air velocity is adjusted from the software by altering fan speed. Fan speed is set as a percentage of maximum speed, between 0% and 100%. An Electronic Balance and software, allows full electronic monitoring and recording of the measured drag and lift forces on the software mimic diagram on the PC. The corresponding static head in the tunnel given as the differential head between the static pressure at the tunnel wall and the ambient atmospheric pressure, expressed as an

equivalent height of water (mmH_2O). The free stream air velocity is displayed in (m/s) on the software mimic diagram.

The experimental setup consists of a smooth suspended hemisphere in the test section tilted for three different angles α (0°, 30° and 52°) to the vertical y-axis during experimental investigation as shown in Figure 9 in order to investigate the effect of the hemisphere angle of attacks to the different parameters of airflow and heat transfer characteristic. The location of the model in the test tunnel and the reference coordinate system are shown in Figure 10. The experimental setup consists an immersed hemisphere of diameter, D = 65 mm in the test section of the wind tunnel. To avoid wall interference, the model is supported from the rear with steel rod of $0.05D$, where D is the diameter of the hemisphere. In addition, the tunnel blockage was overcome by reducing the Mach number value to below 0.1 as stipulated by (Achenbach, 1972). At, for instance, the maximum Reynolds number, which was obtained in the tunnel test section, the Ma number was even lower than 0.08.

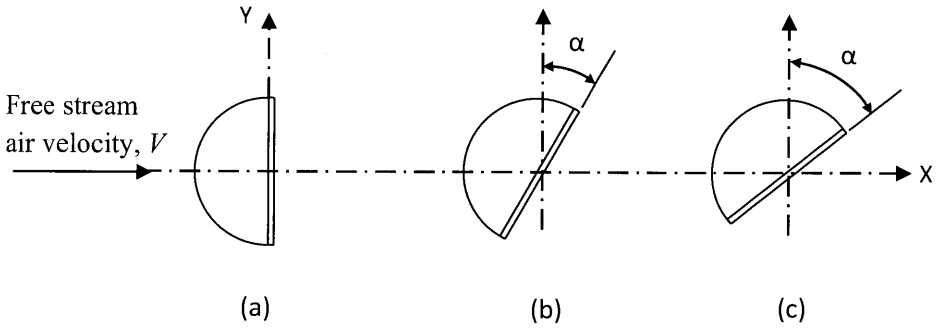


Figure 9: Hemisphere examined at three different tilt angles (α) in the tunnel working section (a) α = 0°, (b) α = 30°and (c) α = 52°

The hemisphere surface was heated by means of one filament heater bonded in the hollow cavity of the hemisphere with high temperature resistant epoxy. The filament heater was placed at the top center of the hemisphere internal surface to ensure symmetry of heat distribution all over hemisphere surfaces. The average temperatures all over hemisphere surfaces maintained at ≈70°C. The electrical input to the filament heater controlled by DC power supply via voltage, current and resistance to maintain the desired constant heat input to the hemisphere surfaces. The local temperature distributions over the hemisphere in the front and back surfaces measured by means of a total twenty one (21) K-type thermocouples embedded in the front and back surfaces of the hemisphere into small slots by heat resistant epoxy resin, and attached to a digital temperature recorder to detect the temperature readings of the hemisphere surfaces at various tests air flow velocities and angle of attacks to the hemisphere. The thermocouples junctions passed into the hemisphere back surface wall through small hole drilled for this purpose. The temperatures readings are taken at thirteen 13 points spread on the hemisphere front surface and were symmetrically arranged in stream-wise and span-wise directions as shown in Figure 12 (a). While the remaining eight 8 points are arranged at the back surface of the hemisphere, as shown in Figure 12 (b). A uniform temperature on the hemisphere surfaces were achieved by adjusting power input to the filament heater, the average temperatures maintained to be close to ≈ 70°C, a deviation of ± 2°C have been observed at certain points away from the heating element and specifically were located at the back surface of the hemisphere. Accordingly we were able to examine the heat transfer behavior over the hemispherical body at various flow speeds and at three different tilt angels. Figure 11 elucidate and summarize the entire control system utilized in the experimental investigations.

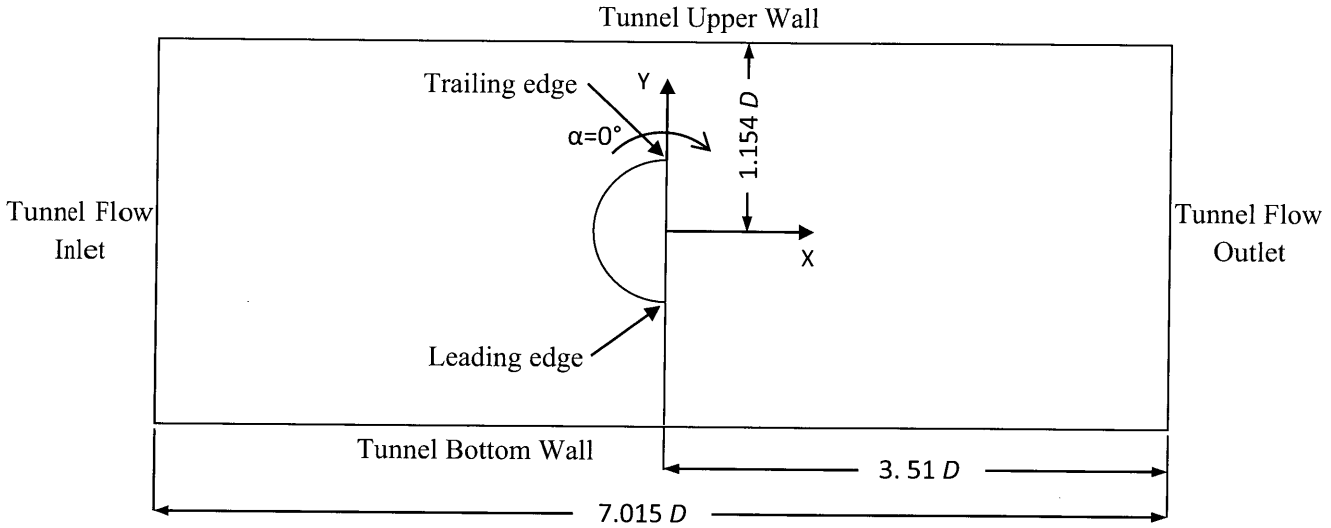


Figure 10: Schematic of the hemispherical model positioned at (α = 0°) tilt angle in the test tunnel working section with reference coordinates system

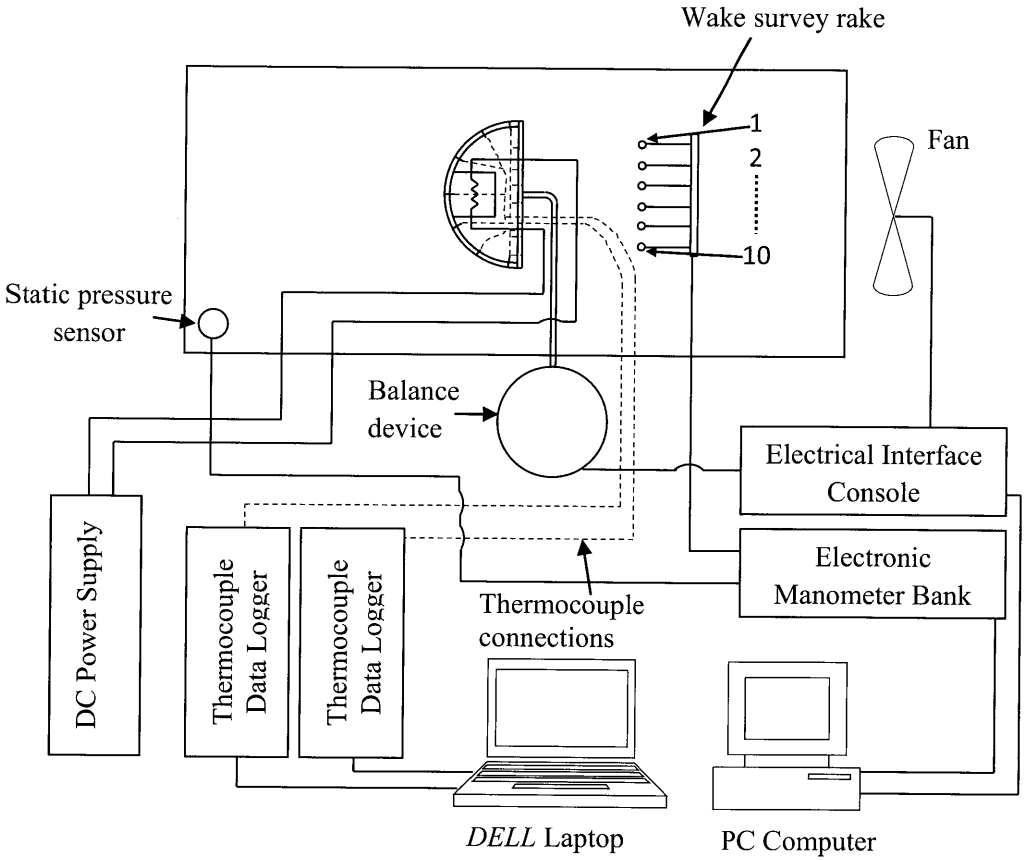
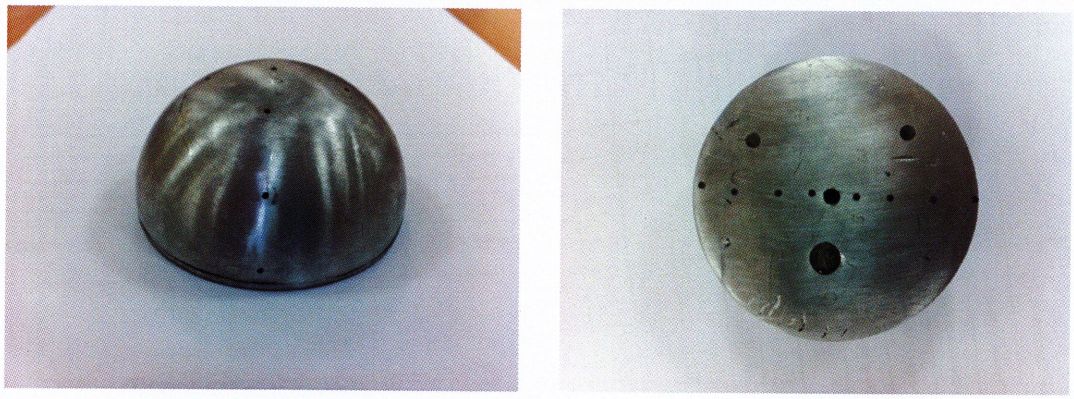


Figure 11: Experimental control system utilized for the heating of the hemisphere surfaces, the measurements of local temperatures over the hemisphere front & back surfaces, drag & lift forces and pressures in the wake region.

3.2 Experimental Apparatus

3.2.1 The Preparation of Model

An aluminum hemisphere with 65 mm diameter D, and wall thickness of approximately 2 mm was used as a testing model in this research. The hemisphere consist of two pieces, a hollow cavity curved body in which it is identified as a front surface of the hemisphere as shown in Figure 12 (a). Additionally, a removable aluminum circular disc having diameter same as hemisphere with a thickness of 2 mm was used to seal hemisphere base body, which also known as back surface of the hemisphere as shown in Figure 12 (b). It is kept removable to allow setting up of the heating element and bonding of the thermocouples to the internal hollow portion of the hemisphere. Fine surfaces maintained for the entire surfaces of the hemisphere. The hemisphere was polished to maintain fine surfaces using 1500 sand papers at the end of all preparations and before commencement of the experimental works.



(a) (b)

Figure 12: (a) Front surface of an aluminum hemispherical model and (b) back surface (disc).

Hemisphere front & back surfaces drilled with a total of twenty one 21 tiny slots with 1.5 mm diameters. Thirteen 13 slots were arranged and spread in the front surface while the remaining eight 8 spread at the back surface of the hemisphere. The slots in the front surface were set to be in two directions, stream-wise and span-wise, respectively, each direction consist of six 6 slots arranged at constant intervals of (25°~ 30°) for meridian angle, θ and azimuthal angle, ϕ, and were numbered from (1 to 7) and (8 to 13) respectively, as shown in Figure 13 (a & b) and their angles values are listed in table 2, both directions intersect at one point wherein a slot number 4 is located (at the apex of the hemisphere front surface). The arrangements of these two directions in the tunnel working section are clearly revealed in Figure 14. On the other hand, the slots at the back surface were arranged to be in straight line numbered from (14 to 21) with certain gaps as shown in Figures 12 (b) & 13 (c), the direction of those slots adjusted to be in the direction identical to the stream-wise direction, this made in the stage when the back disc bonded with the hemisphere body. Those twenty one 21 slots represent the thermocouples locations, wherein the thermocouples conductor's tips placed inside them in which the local surface temperatures at specific locations around hemisphere surfaces were examined at various flow configurations and at different hemisphere tilt angles as revealed in Figure 9. Two small holes located at the top of the circular disc were drilled to allow the filament heater coils pass through them, in order to connect with the power supply, another small hole (8 mm) has been drilled at the bottom side of circular disc as shown in Figure 13 (c), to bring all thermocouples wire bundle through it, so as tidy all wires leaving the hemisphere.

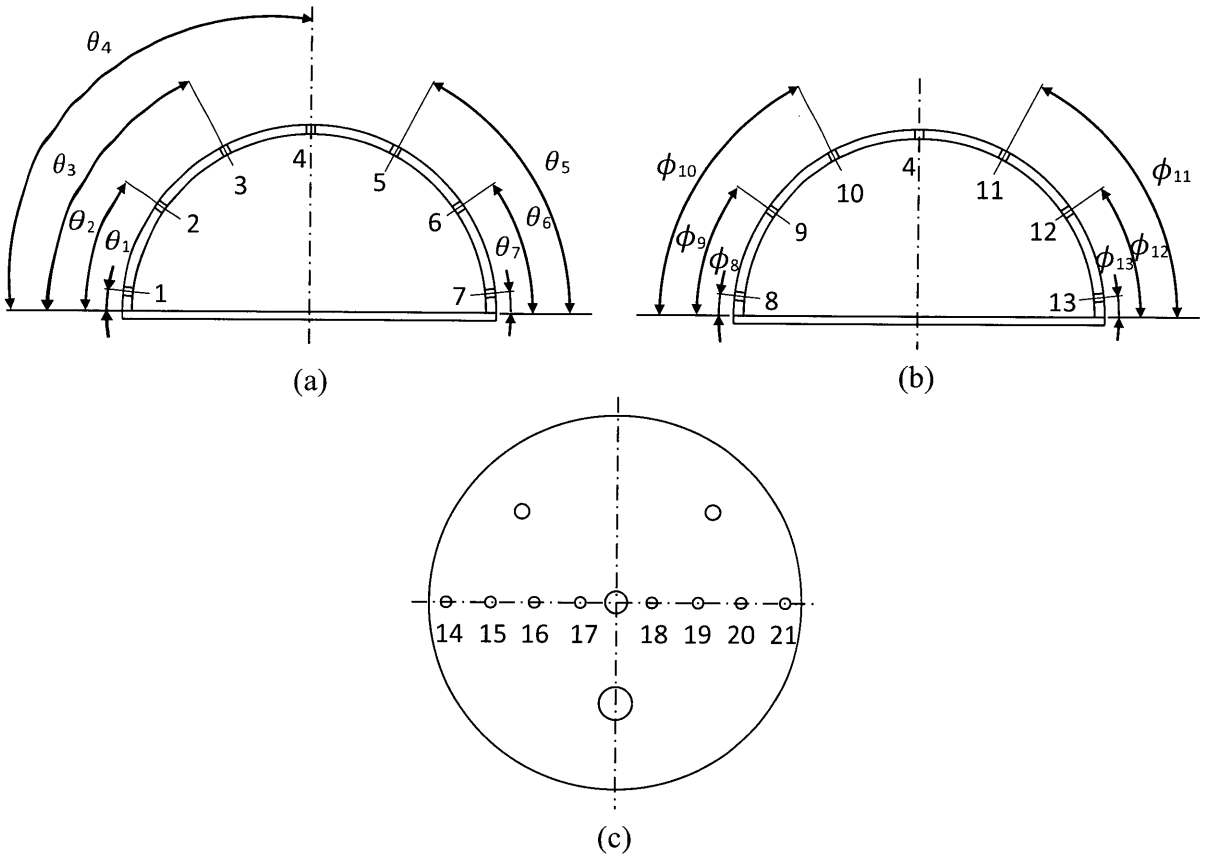


Figure 13: Arrangement of thermocouples slots locations (a) front surface stream-wise direction (b) front surface span-wise direction and (c) back surface

Table 2: Front surface thermocouples tip location angles.

Stream-wise direction (meridian angle, θ)						
θ_1	θ_2	θ_3	θ_4	θ_5	θ_6	θ_7
6°	35°	62°	90°	64°	35°	7°
Span-wise direction (azimuthal angle, ϕ)						
ϕ_8	ϕ_9	ϕ_{10}	ϕ_4	ϕ_{11}	ϕ_{12}	ϕ_{13}
6°	34°	62°	90°	62°	35°	6°

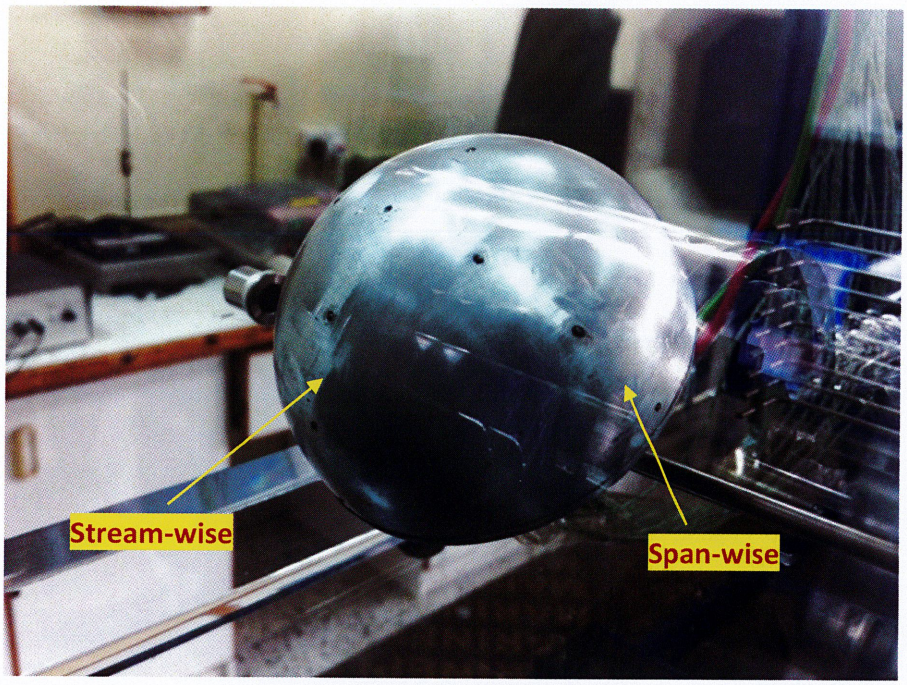


Figure 14: Hemisphere front surface stream-wise & span-wise arrangements in the tunnel working section

The heating element as shown in Figure 15 (a) consisting of a filament heater which is operated by a thin coil to provide required heat input by means of DC power supply. All thermocouples were numbered on their miniature connector by marker in order to place each at the desired slot on the hemisphere surfaces so as to identify the output measurements of each during experiments. At first, the thermocouples from their probe side passed through the bottom 8 mm hole of the circular aluminum disc as shown in Figure 15 (b), to ensure that nothing missed and to make bonding process to the thermocouples easier, thus avoiding unnecessary movement of the whole assembly. The thermocouple probe placed at slot number 4 that located at top surface of the hemisphere passed into heater center body via a tiny slot and is bonded by heat resistant epoxy till it get dried, then the filament heater was bonded in the hollow cavity of the hemisphere, it kept around fifteen minutes to ensure

the epoxy dried enough and the heating element stick with the internal surface. Subsequently we proceed separately with each thermocouple, until completed from hemisphere internal surface with a total of 13 bonded thermocouples, afterward bonding process continued for the thermocouples at circular disc internal surface slots, at that time the arrangement was as illustrate in Figure 15 (b). Finally the filament heater coils passed through two holes as shown in Figure 15 (c) and consequently the disc bonded with the hemisphere by the epoxy and the assembly held together for around 24 hours by means of a small G-clamp tool to ensure the surfaces stick together; the final assembly is shown in Figure 15 (d).

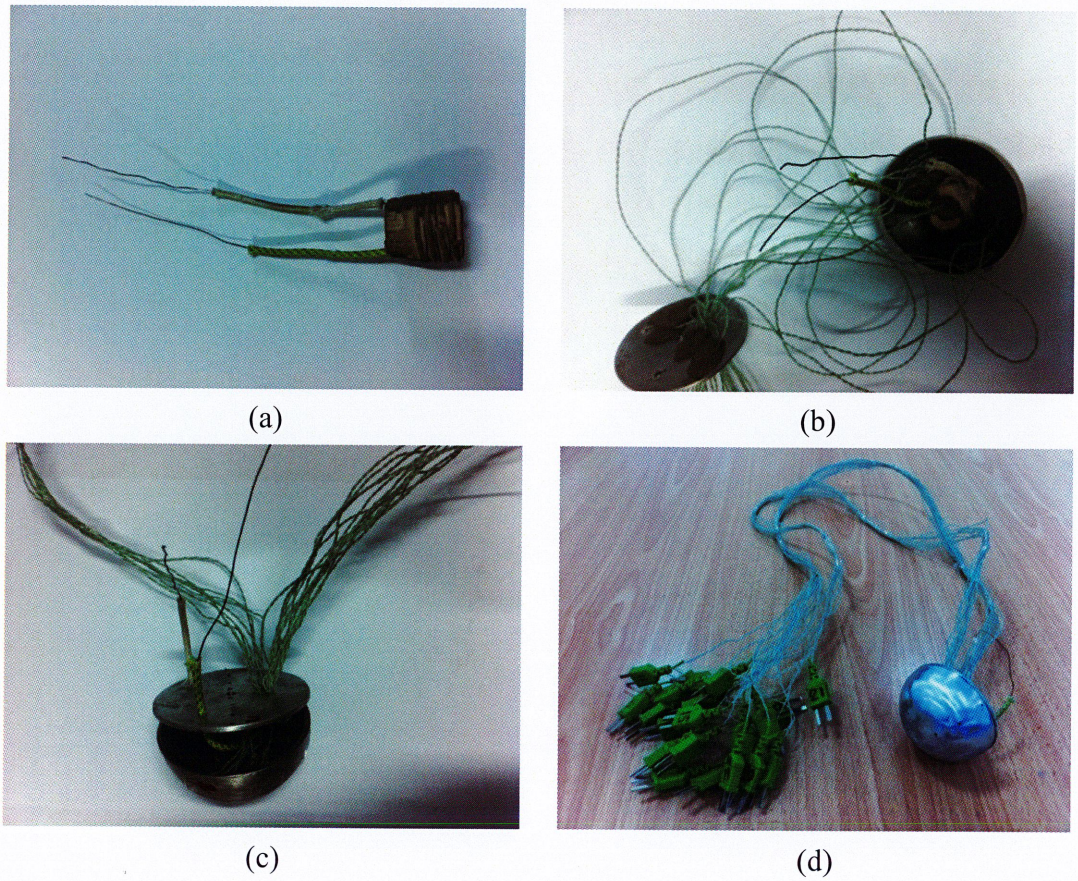


Figure 15: Preparation steps of hemisphere for hot condition experiments, (a) filament heater, (b) bonding of the heating element & thermocouples into internal surfaces of hemisphere & disc, (c) bonding of back disc to the hemisphere body, (d) final assembly arrangement

3.2.2 Wind Tunnel Setup

Basically, the wind tunnel consists of three main parts; The entry section, transparent working section with uniform cross section and outlet diffuser as shown in Figure 16. The main accessories associated with the wind tunnel is the Balance device, Electronic Manometer bank, which connect with Electrical Console (IFD7) and software model (C15-304), allows full electronic monitoring and recording of the measured fluid flow characteristics on the PC.

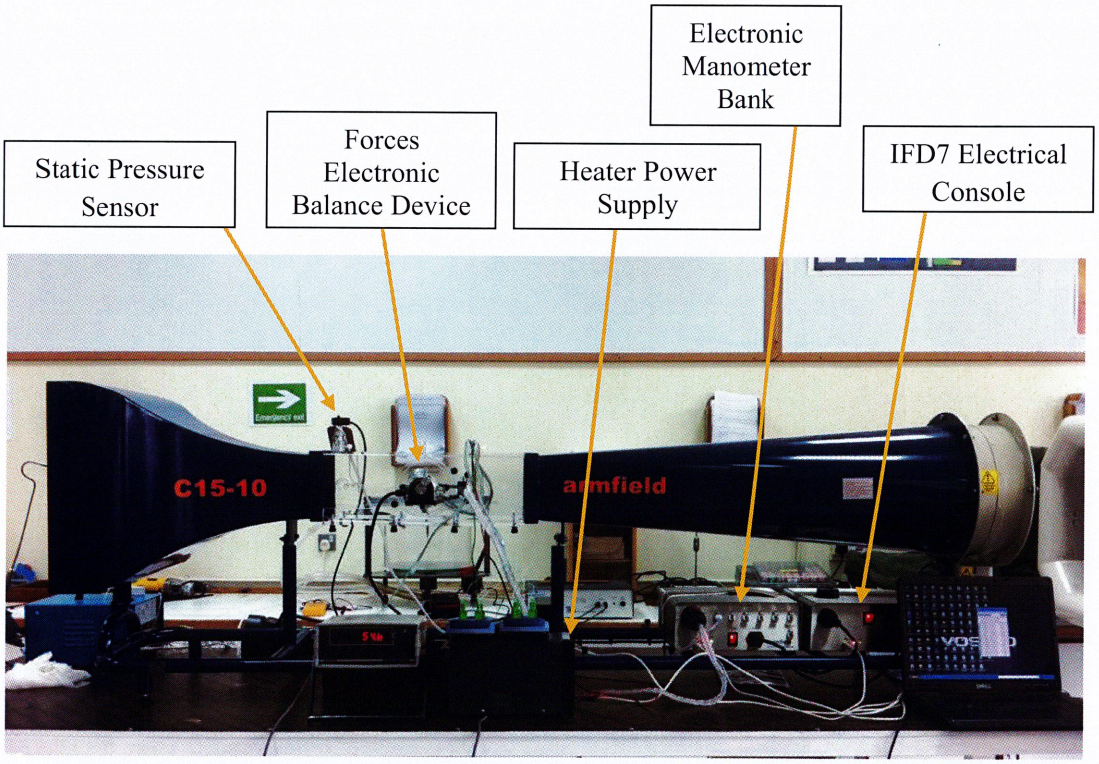


Figure 16: Wind tunnel experimental setup assembly

3.2.2.1 Electrical Interface Console

Electrical Interface Console (IFD7) transfers data from the drag, lift & rotation sensors in the Balance device to a PC computer via the computer's USB port. It also provides necessary power to the Electronic

Manometer Bank and for the wind tunnel motor fan. Additionally the Electrical Interface Console provides a connection to the computer which allows the fan to be controlled from the PC via USB ports. Figure 17 illustrates the IFD7 Electrical Interface console and the necessary connection from the device.

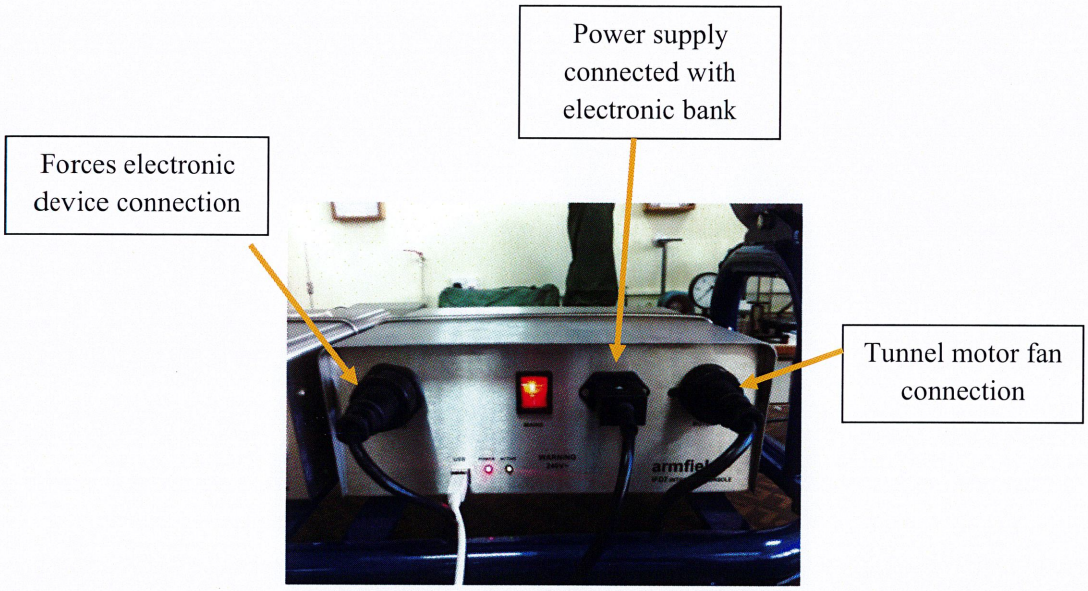


Figure 17: IFD7 Electrical Interface console

3.2.2.2 Electronic Manometer Bank

Through this device the differential pressures head in the tunnel working section are measured electronically and recorded through the software in the computer PC. The software displays each sensor reading on the mimic diagram in boxes labeled marked around the socket in the manometer bank. The electrical supply to the manometer is obtained from IFD7 Electrical Interface Figure 17. Data transferred from the Electronic Manometer Bank to the control PC using a second USB port on the PC. This console incorporates a total of sixteen 16 differential pressure

sensors, each with a range of 0-178 mm H_2O. A ten (10) way connector which contains of 10 tubes numbered (1 to 10) utilized for the measurement of the pressures head in the wake downstream of the hemispherical model which is connected with steel tubes in the Wake Survey Rake device Figure 22. A single way connector number eleven (11) in the manometer bank utilized for the measurement of tunnel working section static pressure, wherein an electronic pressure sensor mounted in a tapping through the side wall at the rear of the working section measures the static pressure near the entry of the working section as shown in Figure 18, allowing the instantaneous air velocity in working section to be calculated and displayed on the software mimic diagram Figure 19. All head differential readings are displayed on the mimic diagram screen in millimeter scale unit (mm H_2O). Also, all the readings from the manometer are relative to atmosphere i.e. they are differential pressures. Figure 20 illustrates Electronic Manometer Bank and the necessary connection from the device.

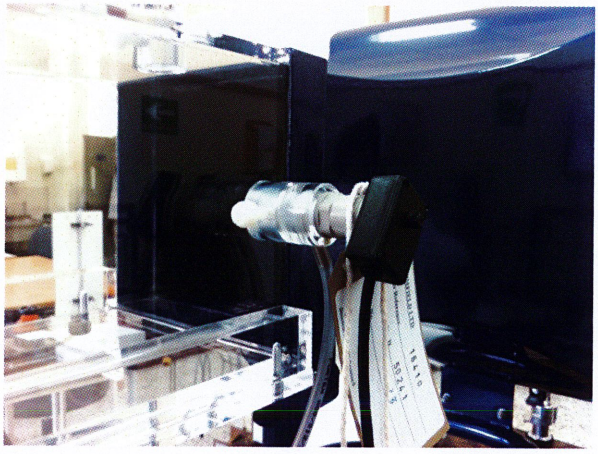


Figure 18: Static pressure sensor

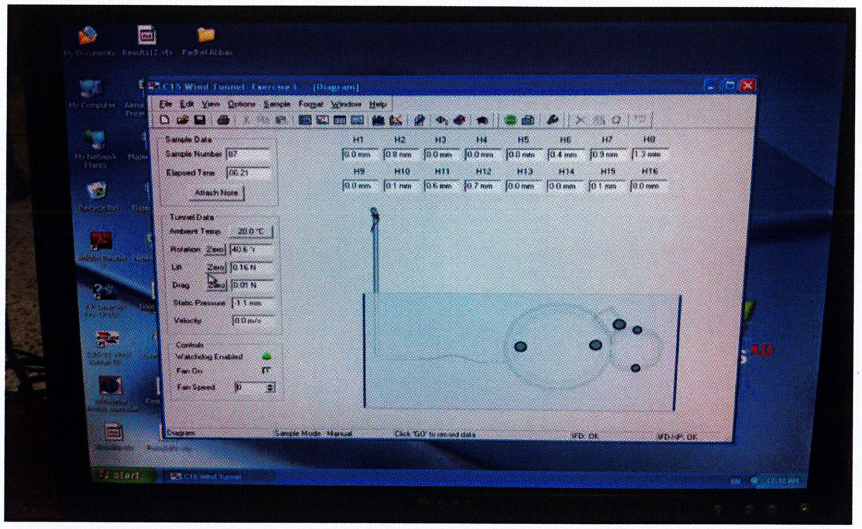


Figure 19: Wind tunnel software mimic diagram screen



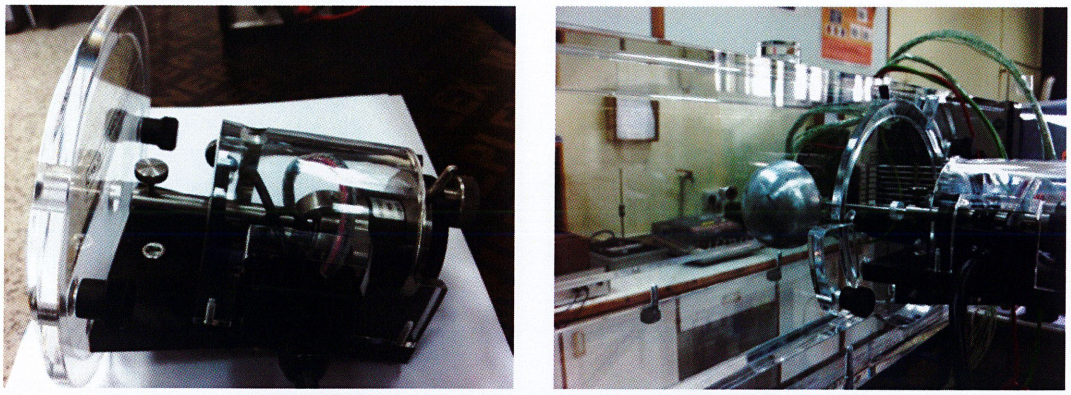
Figure 20: Electronic manometer bank

3.2.2.3 Lift and Drag Electronic Balance Device

The Electronic Balance Device Figure 21 (a) utilized for the measurements of the lift and drag forces of the hemispherical model. The hemisphere assembled to the electronic balance via steel rod tightened in the middle of the hemisphere base disc through small tapping thread Figure 21 (c), the rod end consists of a locating pin which fits into a slot

in the metal collar on the end of the lever arm within the balance device. The rod is secured into the collar by tightening the screw to ensure positioning the model on the centerline of the tunnel working section. The Device consists of sensors responsible for the measurement of the lift and drag forces, the drag force being measured directly and lift by a reduction in the model weight, the ranges of lift and drag measurements are between (0-5.4 N). The Electronic Balance device allow hemispherical model to be rotated ± 52°, the angle of rotation measured electronically by a rotation sensor integrated with this device. The signals from sensors are transmitted through cable from the balance device which is connected to the socket on the interface box, and afterwards the signals from the device are passed via the IFD7 Electrical Interface console Figure 17 to the PC wherein the sensors outputs are displayed on the software mimic diagram.

The hemispherical model assembled with the electronic balance and mounted to the tunnel front wall of the working section through a large circular hatch located in the middle wall of the working section as illustrate in Figure 21 (b). The lift and drag forces readings will be zeroed in the initial stage and before commencement of each experiment, which correspond to the weight of the hemisphere on the balance and with no rearward force on the balance, although the rotation reading adjusted to zero value which corresponds to the hemisphere at zero angle of attack, this done before commencement of the hemisphere rotation for any further testing position where ($\alpha > 0°$).



(a) (b)



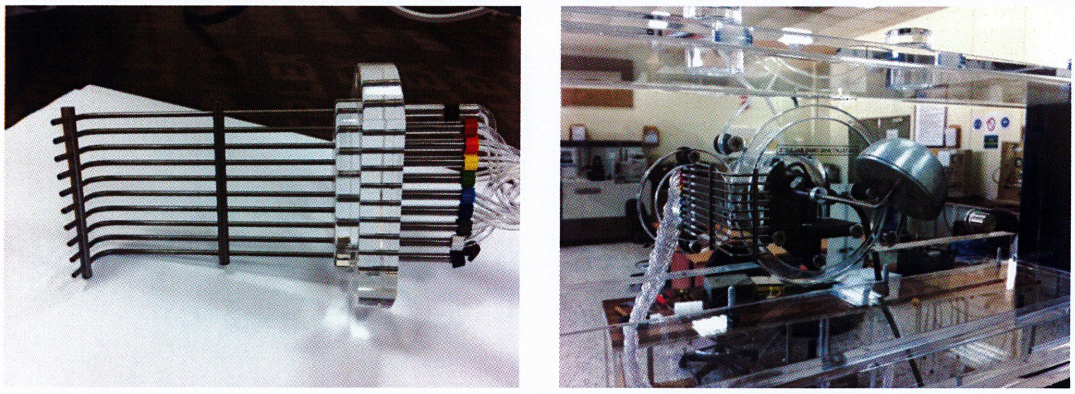
(c)

Figure 21: Measurements of rotation, lift and drag forces by (a) Electronic balance device, (b) device and hemisphere assembly mounted in the working section, (c) stainless steel rod tightened through hemisphere base.

3.2.2.4 Wake Survey Rake

Pressures changes in the wake downstream of the hemisphere were measured using Wake Survey Rake device as revealed in Figure 22 (a). The rake consists of ten 10 stainless steel tubes positioned vertically in a row and pointing towards the airflow direction in the wake region as revealed in Figure 22 (b). The tubes have a fixed pitch of 5 mm and are linked via flexible tubing to multi-way connector sensors in the Electronic Manometer Bank Figure 20.The rake is mounted in the front wall of the working section into small access hatch located downstream

of larger hatch of balance device, Figure 22 (b). The sensors transmit differential head readings in the wake region from the Electronic Manometer Bank to the PC computer in real time in millimeter (mm-H_2O) in which it is displayed in the software mimic diagram in the PC, Figure 19.



(a) (b)

Figure 22: Wake survey rake, (a) stainless steel tubes arrangement (b) survey rake mounting position in the tunnel section

3.2.3 Control System and Data Acquisition Software

3.2.3.1 Hardware and Software Control System

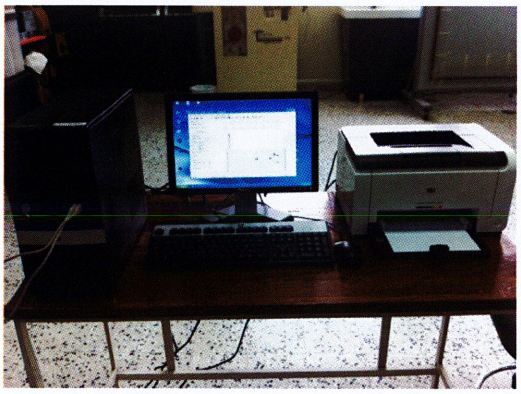
The data acquisition hardware consists of two computers for different purposes. The first system brand is (HEWLETT PACKARD, hp) PC Figure 23 (a), used to run the software package integrated with the wind tunnel in order to control, monitor and record various parameters in the tunnel during the commencement of the experiments on the hemisphere. The software provides sensor output logging and fan control as well as performing all required calculations for the displayed parameters. The data acquisition software also consist of a mimic diagram screen wherein the processing of results and data are presented

in a table format as revealed in Figure 19, the sensors transmit the readings to the computer in real time such as static pressure head at the tunnel wall of the working section, the differential heads arranged tapping points behind the hemisphere indicated as readings in millimeter (mm) of water, also the rotation, lift and drag on the hemispherical model using lift and drag balance were indicated in degree and Newton (N) units respectively. The velocity of air is variably adjusted through the software by altering the tunnel fan speed. Fan speed set as a percentage between 0% and 100%. Air velocity in the wind tunnel is displayed in meter per second (m/s) in the mimic diagram and is calculated from the static pressure measured at the tunnel working section wall, the software has a built-in equation to measure air velocity wherein, $V_{\infty} = (2\rho_{water}\, g\Delta h/\rho_{air})^{0.5}$, which is required before running the tunnel fan to input the ambient temperature reading. The ambient temperature in the laboratory is entered to the software manually, and the reading was taken from a thermometer scale fixed in the lab, which subsequently is used to calculate, air density through software and hence air velocity will be calculated.

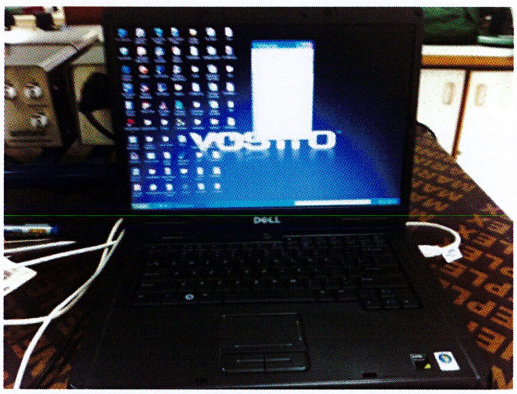
The second system brand is (DELL) Laptop Figure 23 (b), used to monitor and record local temperature readings along hemisphere stream-wise, span-wise directions and at the back surface through PicoLog data acquisition software (PicoLog for Windows) that is installed in the Laptop as shown in Figure 24. The software is integrated with the Thermocouple Data Logger (TC-08) Figure 23 (c), which is powered from USB port through the laptop. Basically, the function of Thermocouple Data Logger (TC-08) is to measure the temperatures readings from the K-type thermocouples (NiCr / NiAl) alloy connected to the device (TC-08) channels. The thermocouples have an effective

temperature range of -270 to +1820°C, and it measures voltages in the range of ±60 mV and the temperature measurement accuracy is (± 1.5°C, ± 0.25%). The thermocouple circuit will actually generate a measurable low-voltage output that is almost directly proportional to the temperature difference produces some net change in the voltage. Therefore the thermocouples readings in micro-volts are converted into temperature readings.

A two Thermocouple Data Logger each consists of eight 8 channels are used to measure temperature readings during the experiments as shown in Figure 23 (c). The software records temperature readings at each second that enable accurate estimation of the temperature changes over a period of time due to force cooling. The time spent to record the drops in the local temperatures over the hemisphere is set to three minutes, which is equivalent to 180 samples of recorded data of temperature readings, the same time maintained for all experimental conditions in which the hemisphere will be tilted at three various angles α and at variable inlet air stream velocities V. The selected time is quite enough to observe the drop occurred to the hemisphere surface local temperatures due to force convection heat transfer from hot surface.



(a)



(b)



(c)

Figure 23: (a) PC to control wind tunnel fan speed, measure lift and drag forces, rotation of hemisphere, tunnel working section static head pressure, hemisphere downstream head pressures, (b) Laptop to monitor and record temperature distributions on the hemisphere surfaces. (c) Thermocouple Data Logger (TC-08) to measure the temperatures readings from the K-type Thermocouples.

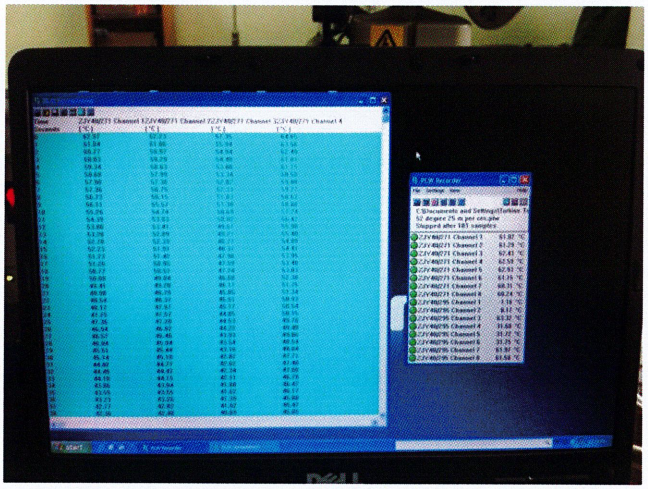


Figure 24: Temperature measurements data acquisition software screen

3.2.3.2 Power Supply System

Regulated direct current DC FARNELL POWER SUPPLY (D30-2) Figure 25 is used to supply necessary power to the filament heater embedded inside hollow cavity of the hemisphere in order to achieve

constant surface heat flux along with the increasing of hemisphere surface temperature from ambient temperature ≈ 20 °C to a hot surface condition at around ≈ 70 °C. The maximum output voltage and current that the Power supply provides are 30 V and 2 Amps, respectively. During all test conditions voltage were maintained at a maximum value of 30 V while the current was manually regulated through changing in resistant value in order to achieve the desired heat input. The current, I value at the hot condition observed approximately ≈1.187 Amps, therefore the estimated power input to the filament heater can be calculated as $P = V \times I \approx 35.61 watt$. The actual power output perhaps lower than the input calculated value of $P \approx 35.61 watt$, hence an expectation that there will be power dissipation lost through the cumulative effect of convection from heated filament, the surface radiation and conduction through hemisphere surfaces. (Refer to Appendix C, for heat transfer losses calculation).



Figure 25: Power supply FARNELL DC utilized for the heat input to the hemisphere surfaces through filament heater

3.3 Experimental Procedure and Uncertainty

In the experimental investigation the collected readings are analyzed and simulated later through (FLUENT) package program. Some of those results are local temperatures distribution over front surface (stream-wise and span-wise) and on the back surface of the hemisphere, drag and lift forces, Reynolds number, tunnel static pressure head inside working section, and differential head in the wake downstream of the hemisphere. In addition flow visualization study was carried to have appropriate picture of the developed boundary layer profile adjacent to the hemisphere surface as well as the nature of flow around hemisphere surface in different flow conditions, and this is explained in next section (3.5).

The maximum air velocity that was achieved depends on the model size, shape and the model orientations to different angle of attack, because of the blockage changes in the working section. However in our experiments the factor of model rotation angle doesn't play a role in increasing the blockage inside tunnel working section and hence the same maximum air velocity achieved in (hot condition) was 25 m/s all over the three tilt angles. The blockage initiated in the tunnel working section in hot condition is due to hemisphere body plus the connections of the thermocouples and filament heater to the hemisphere as shown in Figure 26.

1. Initially, all necessary connections and assemblies shall be prepared ready such as:
    a) Both Electronic Manometer Bank Figure 20 and IFD7 Electrical Interface Console Figure 17, and USB cables are connected to the PC Figure 23 (a).

b) The wake survey rake Figure 22 is mounted downstream of the model via small access hatch in the side wall of the tunnel working section and the stainless steel tubes are connected via flexible tubes to a multi-way quick release connector sensors in the Electronic Manometer Bank Figure 20.

c) The tunnel static pressure sensor Figure 18 tube is mounted in a tapping through the side wall at the rear of tunnel working section and connected via flexible tube to the single way connector socket number 11 in the Electronic Manometer Bank Figure 20.

d) The thermocouples and filament heater connections are passed from working section roof rear tapping located downstream of the hemisphere model position as shown in Figure 26.

e) The steel rod tightened at the middle of back surface (disc) of the hemisphere, while its end connected with the lift & drag balance device as shown in Figure 21 (c). Then the balance device mounted to the front wall of the tunnel working section onto a large circular hatch. The cable from the balance device is connected to the socket on the front of the interface box. After that the tilt angle, α of the hemisphere is manually adjusted to zero degree position by rotating the hemispherical model assembly from the balance device via a lever arm until the two marker aligned together to ensure zero position has been achieved. Finally the rotation value of the model displayed in the mimic diagram is reset to zero as the model at zero degree position in the working section Figure 27 (a), so that for any further rotation

to the hemisphere the rotation degree (α) will be electronically measured and can be obtained directly as displayed in the software mimic diagram screen Figure 19.

f) All parameters displayed in the mimic diagram are reset to zero before starting up tunnel motor fan, such as air velocity, drag & lift forces values.

g) Afterwards the thermocouples are connected to two set of Thermocouple Data Logger (TC-08) that linked to the DELL laptop via USB cables, Figure 23 (b & c), and the filament heater coil is joined to the power supply Figure 25 by means of alligator clip and wires connector.

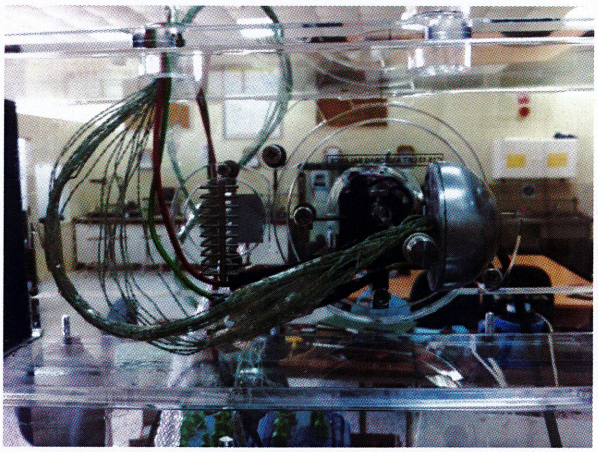


Figure 26: Thermocouples & filament heater coils connections pass through rear roof tapping.

2. Both, the wind tunnel software mimic diagram Figure 19 and PicoLog data acquisition software Figure 24 that installed in the PC & Laptop, respectively are opened in running mode.
3. The IFD7 Electrical Console and the Electronic Manometer Bank are switched ON.
4. Through wind tunnel software mimic diagram we have to make sure the values of drag forces are set to zero before commencement

of the experiment for the desired condition, then the power to the fan is switched ON from the software to make it in standby mode, the fan speed percentage in mimic diagram is reset to zero value. Also the lab ambient temperature reading is set manually in the software mimic diagram.

5. The K-type thermocouples readings displayed in the data acquisition software are calibrated against the thermometer scale reading ($\approx$ 20 °C) that fixed in the laboratory, an average temperature been observed between 20.7 °C ~ 21.4 °C from the software readings. Therefore the accuracy of the thermocouples readings are estimated to be within (95.6 % - 99 %). This procedure was done before the commencement of heating process to the hemisphere in order to estimate errors associated with the used K-type thermocouples.
6. The power supply connected to the filament heater is switched on, the voltage reading set as a constant parameter into a maximum value of 30 V, the resistant is gradually adjusted through power supply with an increment of 0.1055 per 1 °C up to an approximate resistant value of $\approx$ 5.17 wherein a hot condition is achieved for an average value of the hemisphere surface temperatures $\approx$ 70°C. Estimated time spent to obtain hot condition lies between 8 to 10 minutes. An approximate current value, I was $\approx$ 1.187 Amps displayed in power supply, which is proportional to the input resistant value of $\approx$ 5.17.
7. Once hot condition achieved at target temperature immediately we start both the recording process to the temperature readings from the PicoLog data acquisition software, along with the wind tunnel

fan speed which is gradually increased to the desired value, as explained in the next point.

8. Fan speed gradually increases from the software control box until the required air velocity V_∞ inlet is achieved. The air velocity indicated on the PC mimic diagram is an instantaneous average velocity in the test section and it's calculated from the static pressure sensor measured at the tunnel working section wall. The readings of lift/drag forces, differential heads at downstream of the hemisphere are checked to ensure everything are connected correctly, and then three of data samples are taken at variable interval during each test condition to check readings uniformity and to ensure that the system is stabilized. Then the results are saved in separate file.
9. Simultaneously, hemisphere surface temperatures are monitored from the PicoLog data acquisition software. The software automatically record temperature readings at each second. The recording process stopped manually from the software once a steady state surface temperature condition is achieved. The time spent to obtain steady state condition was approximately equal to 3 minutes, which is equivalent to 180 samples of recorded data. Once this achieved the fan is brought to zero speed.
10. Power supply input, P to the filament heater is turned to zero by reducing both voltage and the resistance to zero value from the power supply, making hemisphere surface temperature readings back to room temperature 20 °C.
11. The same procedures from points (4 to 10) were repeated for different tilt angles, α and incoming air velocities, V_∞. At the end of experimental tests condition to the hemisphere under certain (α), then the hemisphere tilt angle, α increased manually to the desired

value before the commencement of the abovementioned procedures. A total of three configurations were performed for the hemisphere in the tunnel as shown in Figure 27. Under each position, five experiments have been performed in which air velocity changed with an increment of 5 m/s until achieving maximum velocity. An overall of fifteen experiments were conducted during experimental investigation as shown in Table 3.

Table 3: Experimental tests and parameters performed for the hemisphere at a constant heat flux.

Hemisphere tilt angle, α positioned in the tunnel working section (1) $\alpha = 0°$, (2) $\alpha = 30°$, (3) $\alpha = 52°$	
Inlet Velocity, (m/s)	Fan Speed Percentage (%)
5	24
10	41
15	61
20	79
25	97

In order to check the accuracy and repeatability of our measurements. The same experiments were repeated for each condition. In general our data showed reproducibility to the most temperatures readings in the repeated experiments, however, maximum difference in the temperature readings was 5 %. The differential heads results in the wake region found close to the values in the initial experiments, a deviation between 2.4 to 4.5 % have been reported. Drag and lift forces deviate by a maximum of 3 % from initial experiments. Moreover, a standard uncertainty analysis was performed for each measurement, and analyzed in details as shown in Appendix A. The uncertainty of temperature measurements was found to be approximately ± 1.5 °C, the uncertainties of static and wake pressure measurements were found to be

approximately ± 0.981 Pa. The uncertainty of air density was found to be approximately ± 4.2×10^{-4} Kg/m^3, and the uncertainty of the measurement of hemisphere area was found to be approximately ± 5.1×10^{-5} m^2.

The calculated results of the total drag and lift coefficients, Reynolds number, Re_D (based on hemisphere diameter), the dimensionless temperature and pressure measurements will involve uncertainties due to propagation of errors. These uncertainties were calculated through the following expression (Beckwith et al., 2007).

$$U_R = \pm\left[\sum_{i=1}^{n}\left(\frac{\partial R}{\partial x_i}U_{x_i}\right)\right]^{1/2} \tag{55}$$

Where U_R is the uncertainty of the measured value R and U_{x_i} is the uncertainty of a given variables x_i upon which R is based (Beckwith et al., 2007). For Drag and Lift coefficients, the x_i is included F_D, F_L, ρ, V_∞ and A. For Reynolds number, Re_D the x_i is included ρ, V_∞, D and μ.

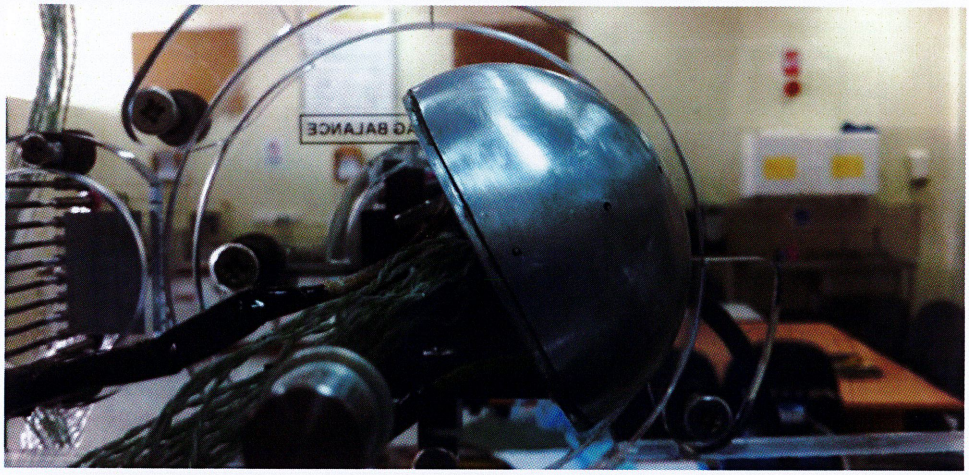
At high Reynolds numbers $Re_D = 107321$ ($V_\infty = 25$ m/s), and hemisphere tilt angle $\alpha = 0°$, the uncertainties of static and wake pressure measurements were found to be small ± 0.261 % and ± 0.289 %, respectively, which revealed high accuracy measurements by the electronic manometer bank. For the drag and lift coefficients, the uncertainties were found to have 1.68 % and 16.7 %, respectively, the uncertainty of the drag is more acceptable than the uncertainty of lift coefficient. However, the larger uncertainty in lift coefficient was 54.1% found at the high tilt angle $\alpha = 52°$ and at $Re_D = 42928.57$ ($V_\infty = 10$ m/s), this could be perhaps due to the presence of an early boundary layer separation in the front surface of the hemisphere and the commencement of flow recirculation that affects pressure distribution over the upper and

lower half of the front surface and therefore the value of lift forces fluctuates within the time, moreover the blockage in the working section could be another reason that affected lift forces of the hemisphere. The uncertainty of Lift coefficient could be reduced in the future experiments by lowering the blockage ratio in the tunnel working section i.e. by reducing the hemisphere size. The present hemisphere to tunnel working section ratio is 0.147 at hemisphere inclination $\alpha = 0°$, and reduces as the tilt angle increases.

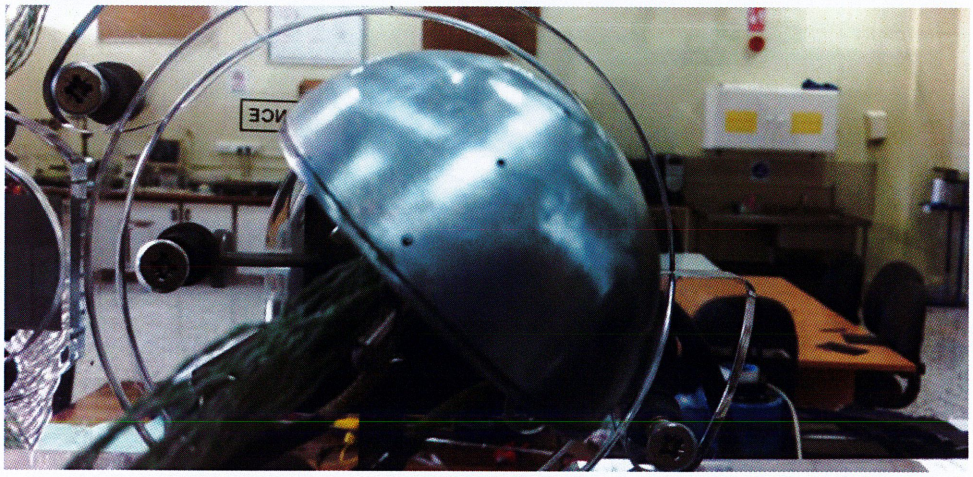
For Nusselt number, the uncertainty of total average Nusselt numbers over the hemisphere surfaces (front and back) was found to have a maximum of 21.3 % at high Reynolds numbers and tilt angle, $Re_D = 107321$ and $\alpha = 52°$, respectively. The uncertainty of total average Nusselt numbers observed to becomes low simultaneously as Reynolds number and tilt angle decreases, and was found to have a minimum of 8.06 % at $\alpha = 0°$. The uncertainty of average Nusselt numbers could be reduced in the future experiments by reducing the heating rate input from the power supply to the hemisphere surfaces along with increasing hemisphere steady state temperature in order to have a sufficient time for observing the cooling process.



(a)



(b)



(c)

Figure 27: Hemisphere positioned at three tilt angles (a) $\alpha = 0°$, (b) $\alpha = 30°$, (c) $\alpha = 52°$.

3.4 Flow Visualization System

The flow visualization study was conducted in order to obtain qualitative information concerning the flow field structure adjacent to the model surfaces, which in turn, assist us to identify for example the developed boundary layer profile over the hemisphere as well as the location of boundary layer separation in different flow conditions. Therefore, a smoke flow visualization experiments were performed to visualize the flow field around the hemisphere positioned in the three different orientations. For this purpose, the smoke generator system (AEROTECH) was used as shown in Figure 28 (a) to produce the necessary smoke for visualization study. In order, to capture clear photos, the working section was covered with black sheets paper from all directions as shown in Figure 29 (a) and (b), and a small square access was maintained at the back wall sheet opposite to the model position to enable monitoring of the smoke flow over the obstacle surface. A suitable adjustment maintained to the oil flow rate along with heater control voltage to suit prevailing optimum condition of smoke, in which under specified condition the oil becomes less viscous and it begins to vaporize and a fairly dense plume of smoke was obtained. Afterward, the smoke probe tip was introduced at the inlet of the wind tunnel parallel to the air stream flow as depicted in Figure 28 (b). In addition, a hand light of high beam was applied to illuminate the smoked flow pattern image over hemisphere surface boundary in the test section, as shown in Figure 28 (c). Also, a camera of iphone 4 was used for photo snapshots. The experimental results of smoke flow visualization are explained in details in the next chapter 4.

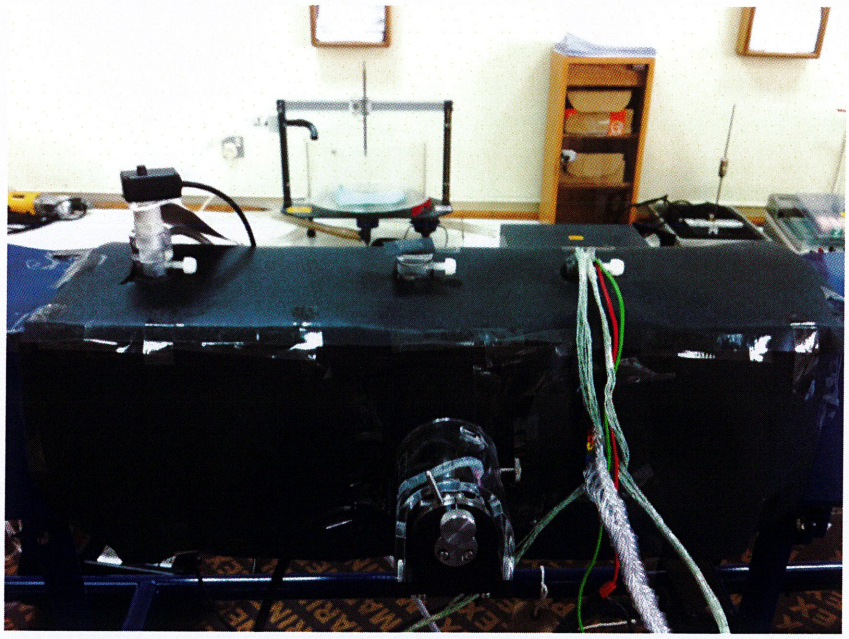


(a)

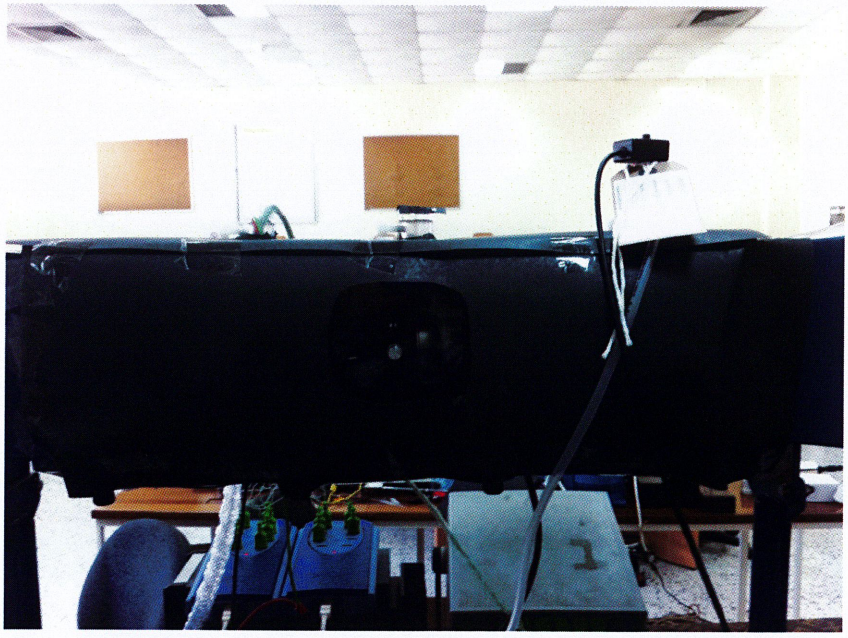


(b) (c)

Figure 28: Flow visualization apparatus (a) smoke generator (b) smoke probe, and (c) hand light



(a)



(b)

Figure 29: Wind tunnel working section covered with black sheets paper (a) front and top walls, (b) back wall with small access for fluid flow monitoring

Chapter 4

Results and Discussions

4.1 Experimental Results
- 4.1.1 Drag and Lift Coefficient
- 4.1.2 Temperature Distribution Over Hemisphere Surface
  - 4.1.2.1 Stream-wise Direction
  - 4.1.2.2 Span-wise Direction
  - 4.1.2.3 Back Surface of the Hemisphere
- 4.1.3 Wake Pressure Measurements
- 4.1.4 Experimental Average Nusselt Number

4.2 Numerical Results
- 4.2.1 Mean Surface Pressure Coefficient
- 4.2.2 Shear Stress
- 4.2.3 Local Nusselt Number
  - 4.2.3.1 Stream-wise Direction
  - 4.2.3.2 Back Surface of the Hemisphere
- 4.2.4 Average Nusselt Number
- 4.2.5 Velocity Contour
- 4.2.6 Validation of Numerical Results
- 4.2.7 Comparison of Numerical and Experimental Average Nusselt Number

CHAPTER 4: RESULTS AND DISCUSSIONS

4.1 Experimental Results

4.1.1 Drag and Lift Coefficient

The total drag coefficient, C_D in cold and hot conditions for the three different hemisphere tilt angles (α) are revealed in Figure 30. The results of total drag coefficient are plotted against Reynolds numbers, *Re*. As can be seen that in cold condition the drag coefficient, C_D increases with Reynolds number up to Re $=1.5 \times 10^5$ and stay almost invariant for high Reynolds numbers between ($1.5 \times 10^5 \leq$ Re $\leq 3.0 \times 10^5$), accordingly C_D becomes Reynolds number independent in this range of *Re*. Perhaps, this is a result of turbulent flow, boundary layer separation and reverse flow due to adverse pressure gradient and large pressure drag taking place at the same point on the upper surface of the hemisphere. Also the values of C_D at cold condition for the three orientations capture similar trends. Moreover, It is observed that the drag coefficient in cold condition increases as the tilt angle, α increase wherein the maximum drag coefficient trend is revealed at higher hemisphere tilt angle $\alpha = 52°$. This can be explained to an early boundary layer separation that takes place at large tilt angle, α at upwind side near the trailing edge and hence the higher pressure drag. Consequently, the lower tilt angle $\alpha = 30°$ the lower C_D values as a result of delayed of boundary layer separation. While at $\alpha = 0°$ the trends of C_D is the lowest since the boundary layer separation is moved further downstream from the leading and trailing edges of the hemisphere (Refer to Ch.3, Figure 10, for geometry details).

The results in hot condition shows similar trends, however with larger values of drag coefficient are observed, and with invariant C_D

values at $Re = 2.0\times10^5$ and above. This perhaps is attributed to larger boundary layer thickness for the heated hemisphere surface and hence a large viscous region. Thus, the drag coefficient is affected by many factors specifically, the fluid viscosity, μ, the flow velocity gradient $(\partial u/\partial y)_s$, and the thermal boundary layer temperature gradient $(\partial T/\partial y)_s$. An increase on the surface temperature will give rise to larger values of viscosity μ and a decrease in $(\partial u/\partial y)_s$ due to buoyancy effect for a mixed convection mode. Perhaps the increase in the viscosity is predominant factor in the drag equation. And therefore the skin friction drag $(\tau = \mu(\partial u/\partial y)_s)$ increases on the surface leading to larger total drag in comparison to the hemisphere surface cold condition.

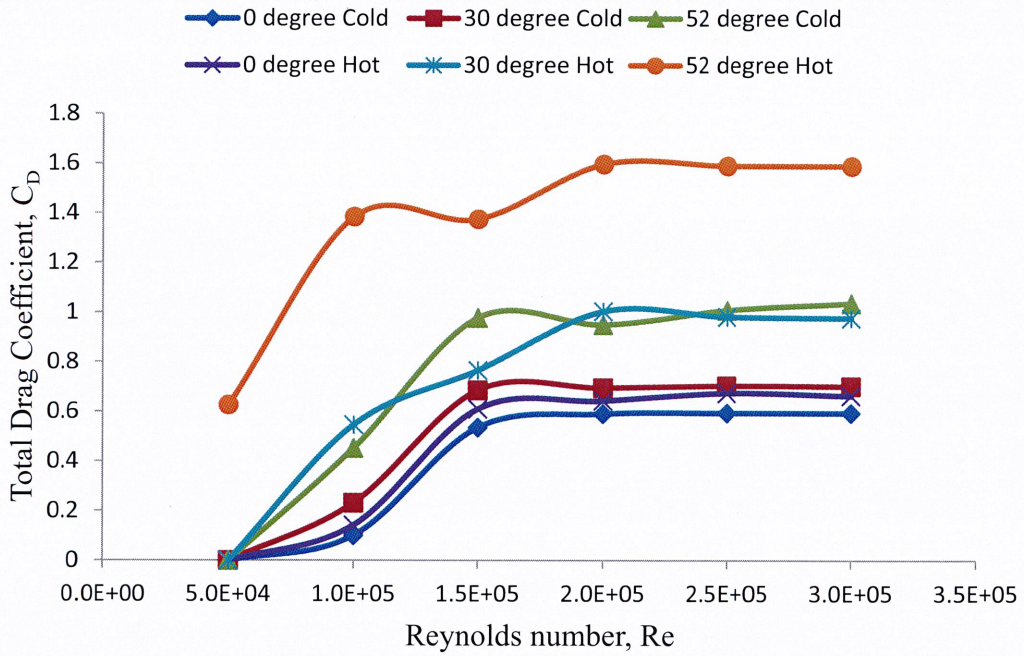


Figure 30: Comparison of total drag coefficient for hemisphere in cold and hot conditions at different Reynolds numbers with hemisphere tilt angles, (α = 0°, α = 30°, α = 52°)

Figure 31 demonstrates the lift coefficient, C_L variations as a function of Reynolds number in cold condition. The lift coefficient, C_L

values at $\alpha = 0°$ in cold condition stays almost invariant for $0.5\times10^5 \leq Re \leq 3.0\times10^5$ and this is due to the flow symmetry where the pressure distribution in upwind and downwind sides of the hemisphere surface terminate each other. However as the tilt angle increases to $\alpha = 30°$ the lift coefficient stays invariant between $0.5\times10^5 \leq Re \leq 1.5\times10^5$ and increases afterwards, this shows that the effect of boundary layer separation becomes significant at high incoming velocity. It is noted that, at higher tilt angle $\alpha = 52°$ the lift coefficient, C_L is erratic between $0.5\times10^5 \leq Re \leq 1.5\times10^5$ and increases thereafter. In general the lift coefficients increases with an increase in (α) between $0.5\times10^5 \leq Re \leq 3.0\times10^5$. This attributed to the increase in the pressure distribution on the lower part (downwind) of the hemisphere compared to the upper part (upwind) where the separation takes place.

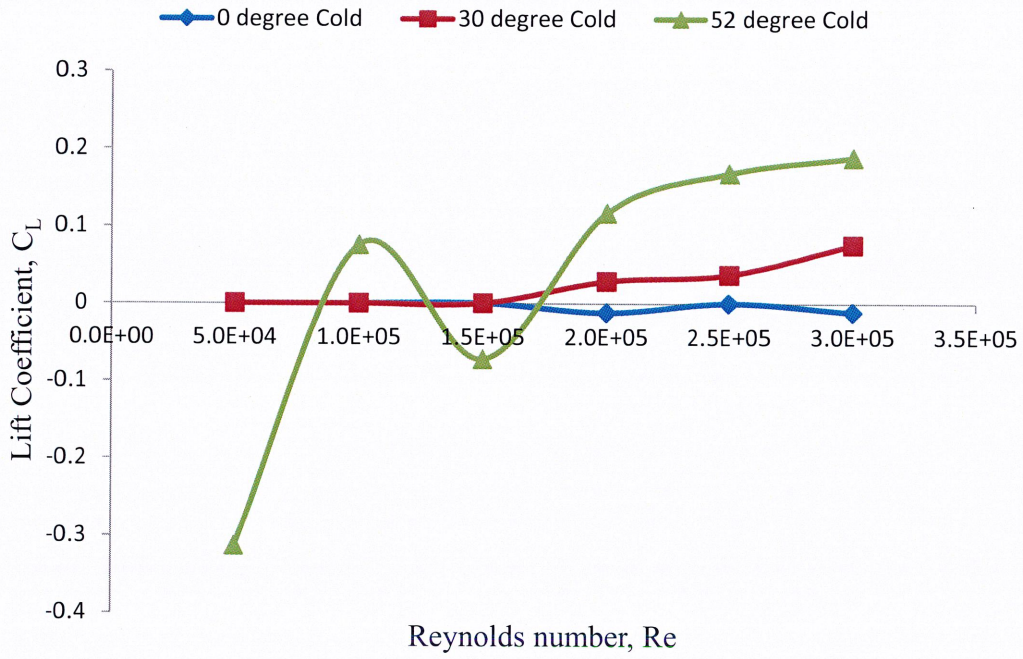


Figure 31: Comparison of lift coefficient for hemisphere in cold condition at different Reynolds numbers with tilt angles, ($\alpha = 0°$, $\alpha = 30°$, $\alpha = 52°$)

4.1.2 Temperature Distribution Over Hemisphere Surface

4.1.2.1 Stream-wise Direction

Figure 32 illustrates the stream-wise dimensionless temperature variations over front surface of the hemisphere with no tilt angle $\alpha = 0°$. The thermocouples location numbered from 1 to 7 taken at specific meridian angle, θ. It is noticed that the dimensionless temperature variations ($\Delta T/T_{atm}$) increases at larger Reynolds number values, where ($\Delta T = T_s - T_s(t + \Delta t)$). This can be explained as Re increases the dissipation of kinetic energy on the surface increases. At each Re value the temperature variation on the surface boundary of the hemisphere also changes, and it shows similar trends on the surface due to symmetry. As can be observed, the higher variation in $\Delta T/T_{atm}$ occurred at points 1 and 7 near the leading and trailing edge, respectively, this is primarily attributed to the variety of the local velocity magnitude over the curvature of the front surface, wherein the velocity gradient $(\partial u/\partial y)_s$ increases as the fluid moves downstream from stagnation point 4 towards leading and trailing edge of the hemisphere, thus the strong flow momentum and larger heat transfer enhancement due to forced convection at those points. On the other hand, this shows that the flow separation didn't occur at locally examined points of 1 and 7 that are located at $\theta = 6°$ (leading edge) and $\theta = 173°$ (trailing edge), respectively. Perhaps, the flow separations in this condition occur only at exact leading and trailing points i.e. at $\theta = 0°$ and $\theta = 180°$, respectively. Moreover, minimal value of $\Delta T/T_{atm}$ is observed at stagnation point 4 ($\theta = 90°$) for all Re, due to low velocity magnitude in this vicinity, accordingly minimal cooling effect occurs.

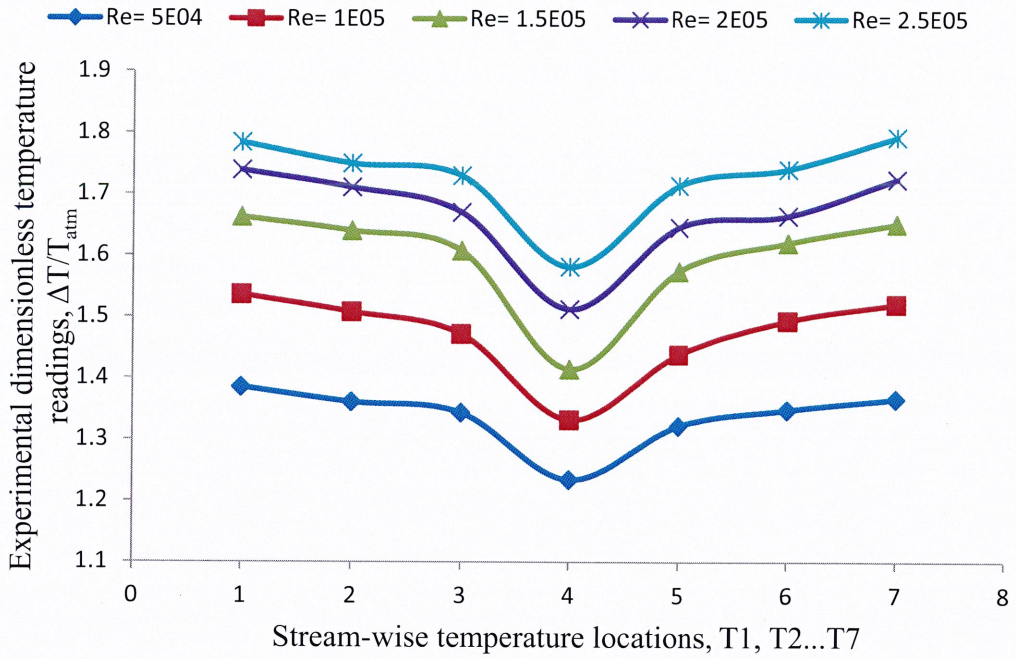


Figure 32: Frontal hemisphere stream-wise dimensionless temperature variations at α = 0° hemisphere tilt angle

Figure 33 shows the stream-wise dimensionless temperature variations for hemisphere tilted at α = 30°. The boundary layer separation and reverse flow takes place due to a strong adverse pressure gradient in the vicinity of the trailing edge front surface of the hemisphere which occurred in the vicinity of points 5 – 7, where the velocity gradient $(\partial u/\partial y)_s \approx 0$ and $\Delta T/T_{atm}$ decrease due to low velocity magnitude, large boundary layer thickness, unsteady transition and turbulence flow, thus lower cooling effect on the surface. However on the leading edge of the front surface of the hemisphere, at point 1, the flow doesn't separate giving higher variations in $\Delta T/T_{atm}$ due to effective cooling at this point as a result of thin boundary layer and strong flow momentum. It is clearly shown that the stagnation point takes place earlier at $\theta \approx 62°$ located approximately at point 3, where a minimum temperature variations are noticed at all Reynolds numbers.

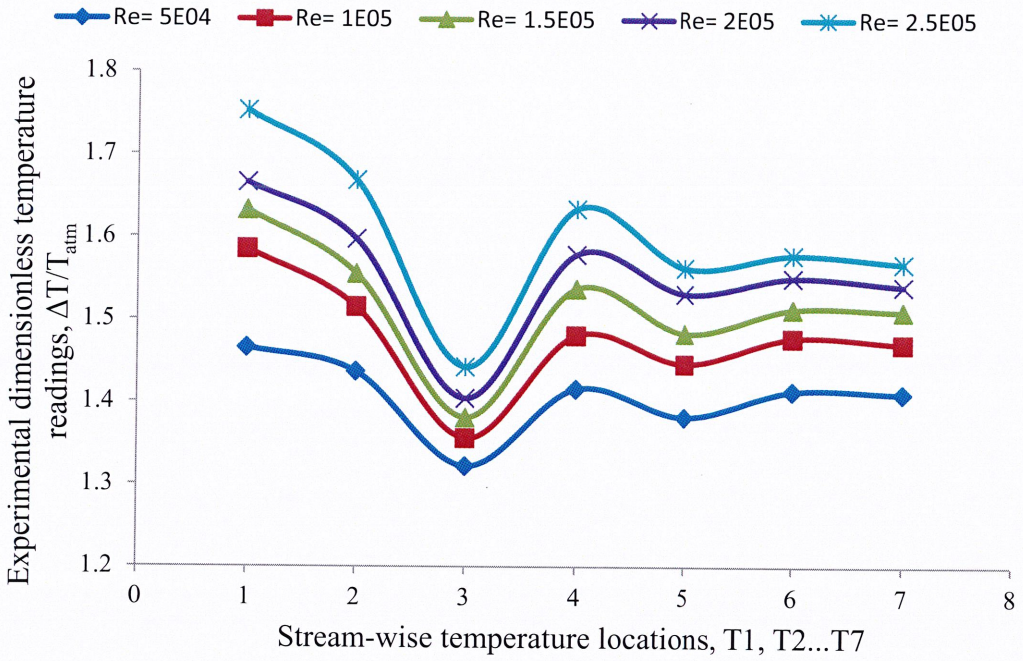


Figure 33: Frontal hemisphere stream-wise dimensionless temperature variations at α = 30° hemisphere tilt angle

Figure 34 demonstrate the stream-wise dimensionless temperature variations for hemisphere tilted at α = 52°. The boundary layer separation and reverse flow in the vicinity of the trailing edge occurred between local points 5 - 7, in which the variations of $\Delta T/T_{atm}$ become unsteady due to low velocity magnitude, transition and turbulence large boundary layer thickness and thus lower cooling effect on the surface, where the velocity gradient $(\partial u/\partial y)_s \approx 0$. On the other hand, at the leading edge at point 1, it revealed higher variations in $\Delta T/T_{atm}$ compared to the trailing edge due to strong flow momentum, thin boundary layer and no boundary layer separation. Thus, heat transfer enhancement in this zone is larger. The stagnation point for this configuration moves further to the downwind side of the hemisphere to $\theta \approx 35°$ which is located approximately at point 2, where a minimum temperature variations are noticed at all Reynolds numbers. It is observed that, among the previous lower tilt

angles an enhancement achieved in heat dissipation specifically at the leading edge by about 6.8 % and 8.7 % compared to the hemisphere tilt angles $\alpha = 0°$ and $\alpha = 30°$, respectively.

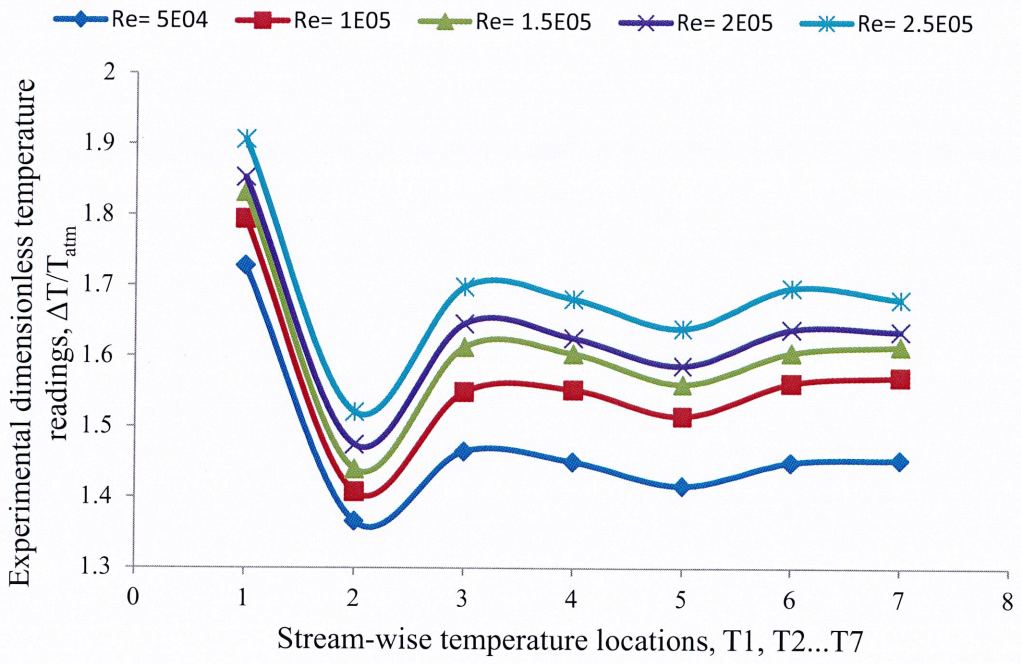


Figure 34: Frontal hemisphere stream-wise dimensionless temperature variations at $\alpha = 52°$ hemisphere tilt angle

4.1.2.2 Span-wise Direction

The local temperature readings were also investigated in the span-wise (azimuthal) direction at six points numbered from 8 to 13, plus the common middle point thermocouple number 4, and each having specific azimuthal angle, ϕ. Figure 35 shows a symmetric trends of dimensionless temperature variations around local point 4 where the stagnation point occurred at $\phi = 90°$ when the hemisphere positioned at $\alpha = 0°$. It is obvious that the temperature variations $\Delta T/T_{atm}$ is Reynolds number dependent. Similarly as in stream-wise, the amount of $\Delta T/T_{atm}$ is changing at each *Re* value; due to the gradual increase of the velocity

gradient $(\partial u/\partial y)_s$ as the flow move azimuthally around the hemisphere curvature. Accordingly, the variations in $\Delta T/T_{atm}$ near the leading and trailing edge are at its maximum values namely at point 8 and 13 that locates at $\phi = 6°$ and $\phi = 174°$, respectively, wherein a maximum cooling is achieved. It is also noticed that the readings obtained in this figure (span-wise) are insignificantly lower than those in the same configuration for the stream-wise section in Figure 32 by around 0.25 % to 6.0 %, this perhaps associated to an experimental errors, consequently, this verify the uniformity of the amount of heat dissipation from the front surface of the hemisphere at α = 0° in both stream and span wise direction.

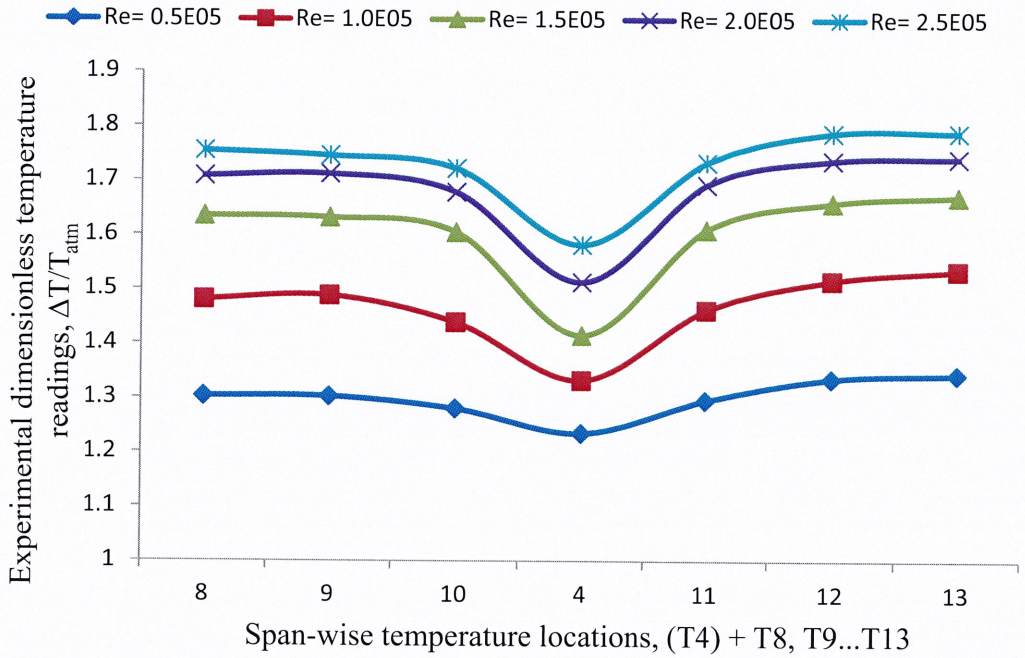


Figure 35: Frontal hemisphere span-wise dimensionless temperature variations at α = 0° hemisphere tilt angle

Figure 36 also shows symmetric trends of temperature variations in span-wise direction around point 4 when the hemisphere tilted at α = 30°. In addition, the dimensionless temperature trends remain Reynolds

number dependent. It's more pronounced that there is no boundary layer separation in the span-wise direction near point 8 and 13 in all Reynolds number, this can be explained as the temperature variation increases gradually in a symmetrical manner from point 4 towards the hemisphere edges, as a maximum effective cooling is shown at these vicinities due to thin boundary layer and strong flow momentum. The minimum values of $\Delta T/T_{atm}$ obtained at point 4 can be perhaps, related to the low flow momentum in this region. It is observed that, an enhancement achieved in heat dissipation by about 0.94% to 7.79% compared to the hemisphere with no tilt angle $\alpha = 0°$.

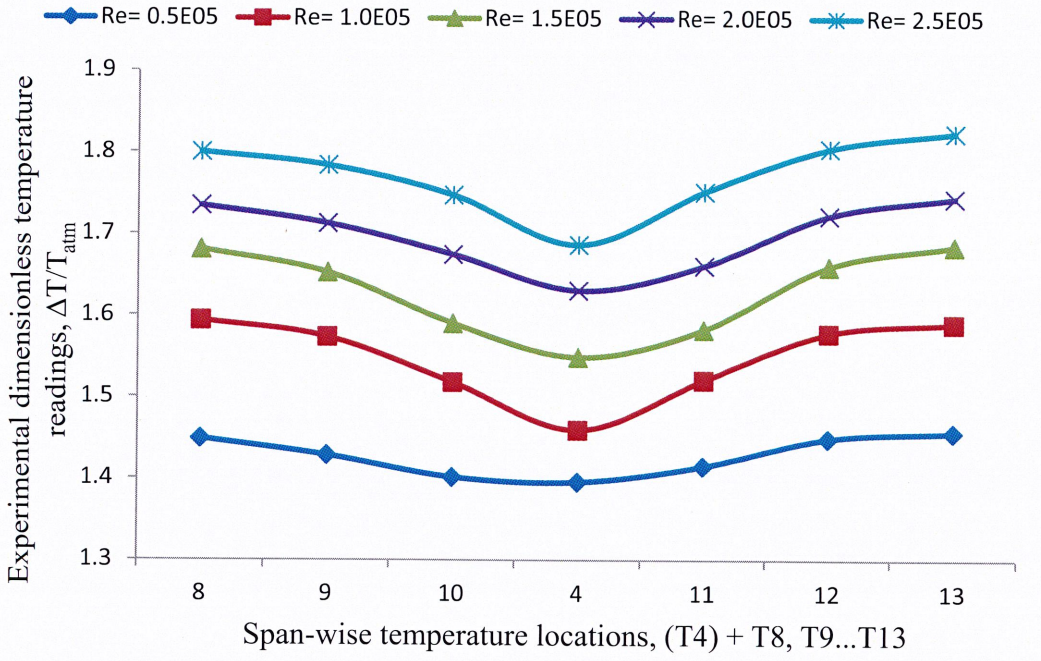


Figure 36: Frontal hemisphere span-wise dimensionless temperature variations at $\alpha = 30°$ hemisphere tilt angle

The trends of $\Delta T/T_{atm}$ in the span-wise direction when the hemisphere is tilted at $\alpha = 52°$ is shown in Figure 37. It can be noticed that, a rapid increase in dimensionless temperature beyond local thermocouple point 4 towards point 8 and 13 located near the hemisphere

edges, namely at Reynolds number between $1.0\times10^5 \leq Re \leq 2.5\times10^5$. In contrast, at low $Re = 0.5\times10^5$ the variation of $\Delta T/T_{atm}$ is insignificant compared to the middle point number 4. However, it is obvious that the variation of $\Delta T/T_{atm}$ remain Reynolds number dependent. An enhancement in heat transfer is revealed to increase by around 0.3 % to 9.77 %, in comparison to the hemisphere positioned at $\alpha = 30°$. This could be perhaps attributed to that, as the azimuthal section that contains the seven thermocouples is shifted more away from the stagnation point by an angle equal to the hemisphere tilt angle (α), therefore at large tilt angle the fluid accelerates symmetrically creating a region of minimum boundary layer thickness at the azimthal section in which an effective cooling takes place due to high flow momentum.

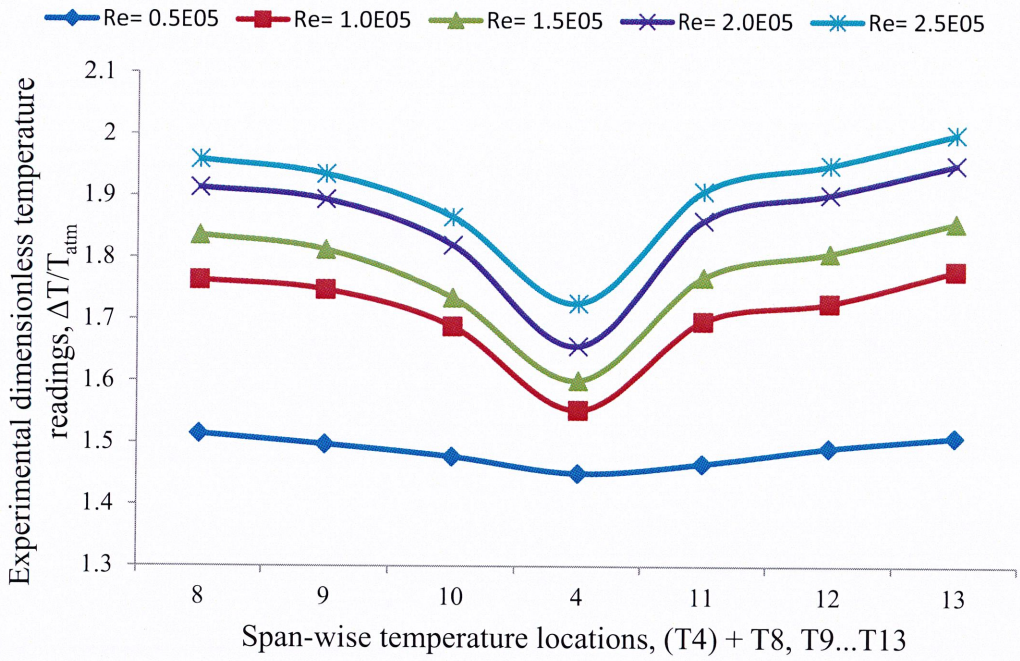


Figure 37: Frontal hemisphere span-wise dimensionless temperature variations at $\alpha = 52°$ hemisphere tilt angle

4.1.2.3 Back Surface of the Hemisphere

Similar temperature variations trend is shown in Figure 38 along back surface of the hemisphere with no tilt $\alpha = 0°$, for different *Re* values. The lowest variations in dimensionless temperature take place at lower Reynolds number $Re = 0.5\times10^5$ and increases at larger *Re* values. It is noticed that at point 17, near the center of the hemisphere back surface, $\Delta T/T_{atm}$ is at its lowest values for all Reynolds number, this can be explained due to minimal air flow velocity in this vicinity of downstream domain of the hemisphere. On the other hand, the temperature variation is at its larger values at point 14 and 21 due to high flow recirculation near leading and trailing edge generated by flow separation at these edges. The variation decreases beyond those points, as the momentum of flow recirculation decreases. It is also noted that at $Re = 0.5\times10^5$ the trend of $\Delta T/T_{atm}$ remains almost invariant along back surface from point 14 to 21 and exhibit low cooling enhancement. In this configuration, the symmetry is revealed in the temperature variations from point 17 towards the leading and trailing edges.

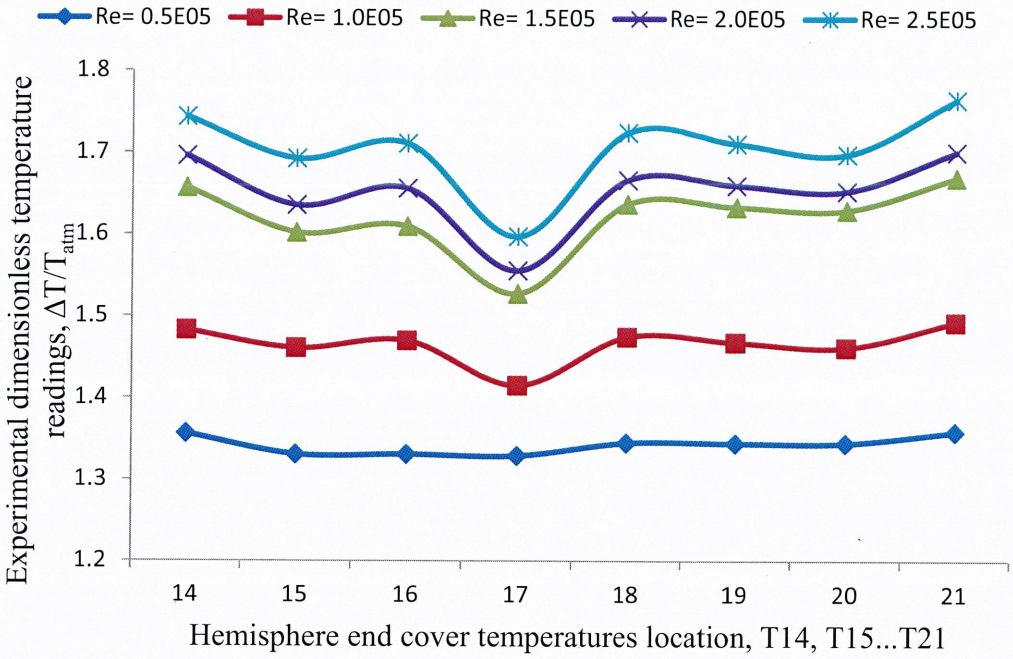


Figure 38: Hemisphere back end dimensionless temperature variations for hemisphere tilt angle $\alpha = 0°$

Figure 39 shows the temperature variations along back surface for the hemisphere tilted at $\alpha = 30°$, It can be noticed that high variation in dimensionless temperature from point 14 to 16 near the leading edge (downwind side), this is attributed to the presence of high flow recirculation in this region enhanced by the maximum flow momentum at the leading edge of front surface in which the flow separation occurs at the edge providing strong recirculation in this vicinity behind hemisphere. In contrast, the trend of $\Delta T/T_{atm}$ decreases and remains almost invariable towards the trailing edge from point 18 to 21; this is because of an earlier boundary layer flow separation that occurred on the front surface near the trailing edge and eventually the boundary layer becomes thicker and the momentum decreases contributing in decreasing flow recirculation behind hemisphere near this region. It is also noted in this graph that the

heat dissipation has increased by a maximum of 3.91 % near the leading edge at points 14 to 16 in comparison to tilt angle $\alpha = 0°$.

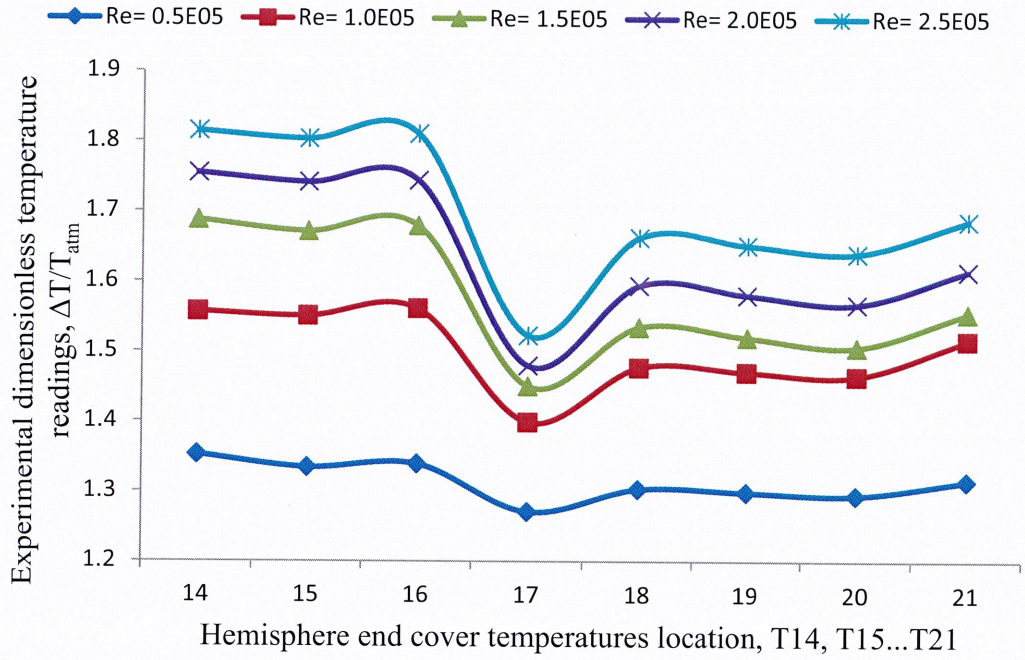


Figure 39: Hemisphere back end dimensionless temperature variations for hemisphere tilt angle $\alpha = 30°$

Figure 40 elucidates the temperature variations along back surface for the hemisphere tilted at $\alpha = 52°$. It can be observed that the dimensionless temperature continue to increase near the leading edge from point 14 to 16 over the region near the trailing edge from point 18 to 21, this is perhaps attributed to a further increase of the flow momentum over front surface towards the leading edge which subsequently created an area of strong eddies as the flow separates exactly at the leading edge. Accordingly, the region of effective cooling for this configuration has increased by around 7.6 % and 3.33% at the downwind side of the hemisphere back surface in comparison to that at $\alpha = 0°$ and $\alpha = 30°$, respectively. On the other hand, the region towards the trailing edge from point 18 to 21 shows inconsiderable improvements in heat dissipation.

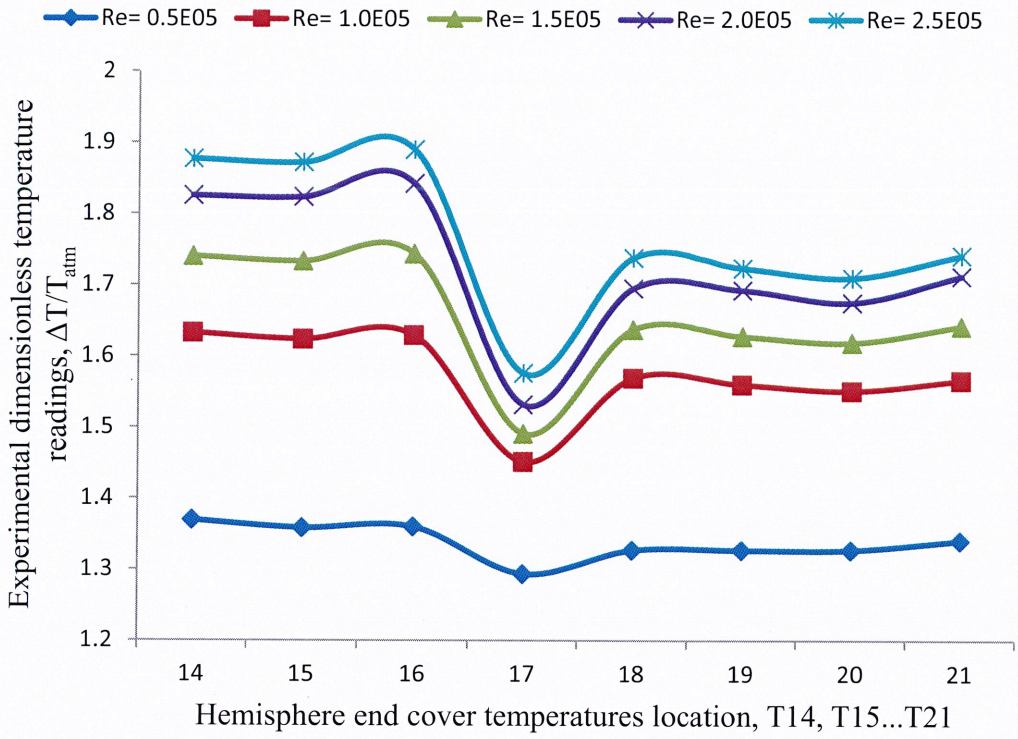


Figure 40: Hemisphere back end dimensionless temperature variations for hemisphere tilt angle α = 52°

4.1.3 Wake Pressure Measurements

Figure 41 depicts the dimensionless pressure variations (P_{abs}/P_{atm}) in the wake region of the hemisphere at zero tilt angle (α = 0°), where, $P_{abs} = (P_{atm} - P_{wake})$, is the absolute pressure from tapping point 1 to 10 taken at a distance of 98 mm from the hemisphere back surface (refer to Ch.3, section: 3.2.2.4, for more details), whilst, P_{wake} in the above equation is the local static wake pressure measured from the obtained differential head, Δh. It is observed that the variations of dimensionless wake pressure is Reynolds number dependent, thus the variation of wake pressure decreases as Re increases. This can be attributed, as increasing in the incoming flow velocity, thus increasing in the flow momentum as well as recirculation downstream of the hemisphere providing strong wake region and hence low pressure. It is

also noted that the trends of P_{abs}/P_{atm} stay almost constant from tapping point 1 to 10 at Reynolds number range between $0.5\times10^5 \leq Re \leq 1.5\times10^5$, while at higher range of Re values, $2.0\times10^5 \leq Re \leq 2.5\times10^5$ the variation in wake pressure is more pronounced, wherein the lowest value of P_{abs}/P_{atm} occurred at the middle region downstream of the hemisphere, namely between local tapping points 4 and 6, this can be explained to the low velocity magnitude in this region i.e. strong wake. Furthermore, it is clear that the trends of dimensionless wake pressure increases away from the middle region towards point 1 and 10 so as the velocity magnitude increases. Moreover, the wake pressure at point 1 and 10 are almost identical at higher Re values, due to flow symmetry at $\alpha = 0°$. The variations of pressure measurements in the wake region are observed to be below atmospheric pressure for all Reynolds number values at a distance of 98 mm away from hemisphere back surface.

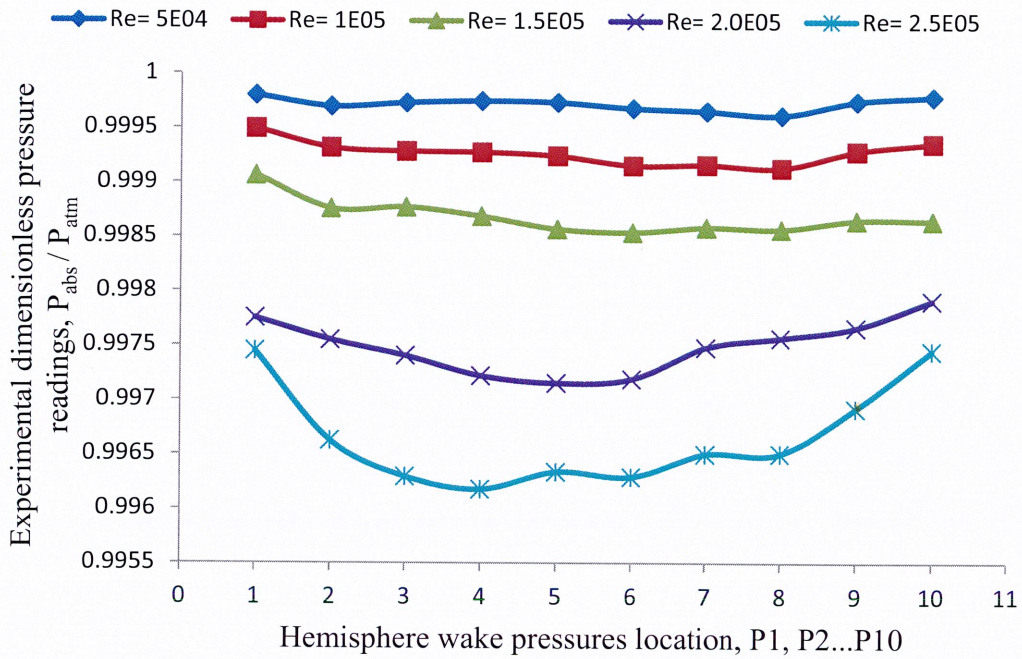


Figure 41: Dimensionless wake pressure variations with hemisphere tilt angle ($\alpha = 0°$)

The wake dimensionless pressure variations for hemisphere tilted at 30° is shown in Figure 42. In this configuration the linear distance from hemisphere back wall to pressure tapping points is increased linearly as a result of hemisphere rotation, in which the shortest distance will be at tapping point 1 (81.75 mm) and the largest at tapping point 10 (114.25 mm). It is noted that the effect of tilt on wake pressure is insignificant at lower range of Reynolds number $0.5\times10^5 \leq Re \leq 1.0\times10^5$, due to narrow wake region and an early reattachment of the flow. In contrast, the changes in the wake pressure is obvious at higher Reynolds number between $1.5\times10^5 \leq Re \leq 2.5\times10^5$. Moreover, the wake pressure measurements have shown low values at point 1 (trailing edge) and continued to decrease up to the middle region near points 4 - 5 as a result of high flow momentum enhanced by flow reattachments, that is caused by an early flow separation near the trailing edge of front surface. The gradual increase in pressure towards the leading edge at point 10 is possibly attributed to the loss in the flow momentum caused by high flow recirculation at lower half portion of the hemisphere back surface, owing to flow separation at the leading edge of the front surface.

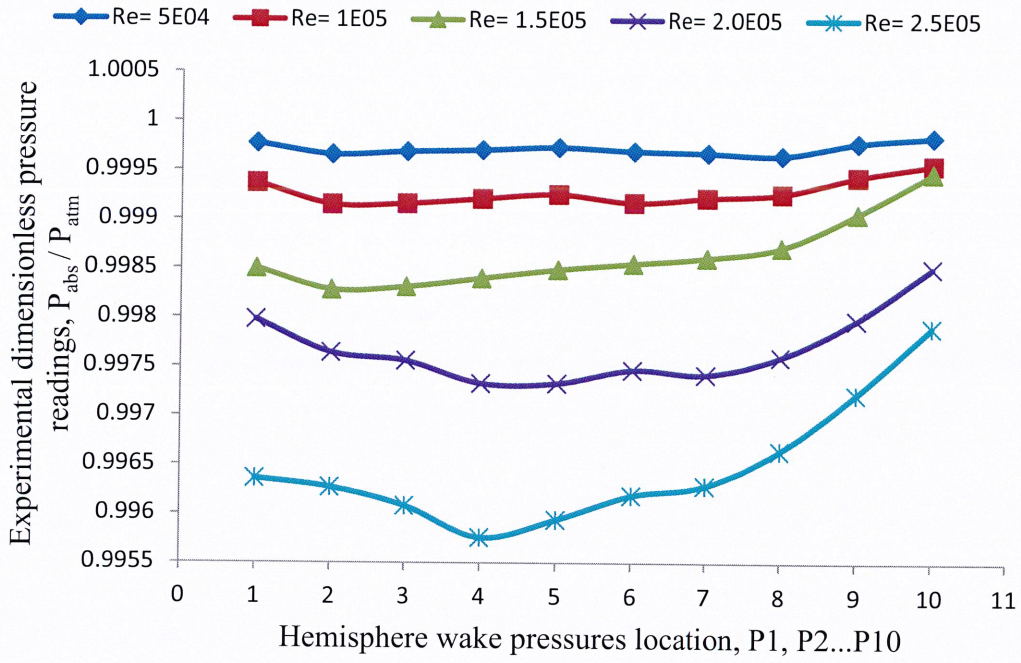


Figure 42: Dimensionless wake pressure variations with hemisphere tilt angle (α = 30°)

Figure 43 demonstrates the dimensionless pressure variations in the wake region of the hemisphere tilted at α = 52°. The further increase in hemisphere rotation leads to changes in the linear distance from hemisphere back wall to the pressure tapping points, wherein the shortest distance is (72.38 mm) at tapping point 1 and the largest at tapping point 10 (123.61 mm). It is evident that the variation of dimensionless pressure is Reynolds number dependent. At low range of Reynolds number between $0.5\times10^5 \leq Re \leq 1.0\times10^5$ the trends remain almost invariant, so the effect of tilting at this range is without any significant effect. The variation is more explicit at higher range of Reynolds number between $1.5\times10^5 \leq Re \leq 2.5\times10^5$, the pressure trend is exponential from tapping points 2 to 10, owing to the increase in the velocity magnitude towards point 10. It is observed that the dimensionless wake pressure at point 10

reaches almost to one. Thus we can infer that beyond 123.61 mm, the wake region has diminished and free stream conditions exist.

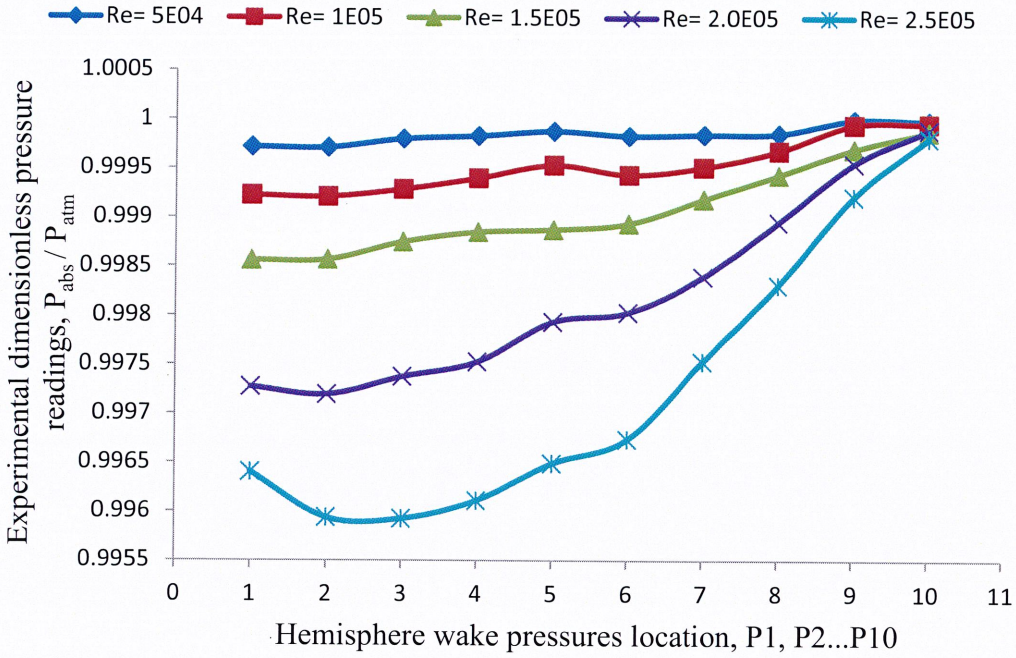


Figure 43: Dimensionless wake pressure variations with hemisphere tilt angle (α = 52°)

4.1.4 Experimental Average Nusselt Number

The experimental estimation of average Nusselt number is primarily depends on the amount of heat transfer input over the hemisphere surface areas. Therefore, the total hemisphere surface area will be the addition of the front curved surface area and base circular area as follow;

$$A_T = A_f + A_b = 3\pi r^2 \tag{56}$$

The total heat input to the hemisphere surfaces is maintained by DC power supply. Thus, the heat transfer rate output from the hemisphere front and back surfaces, q_T is equal to the heater power dissipation.

However, considering the losses in the heat input through the cumulative effect of surface radiation and conduction over the surfaces, thus it is estimated that the losses is around 15 % from the total heat input, P, (refer to Appendix C, for heat transfer losses calculation). As a result the total heat output, q_T from the hemisphere front and back surfaces can be calculated as follow;

$$q_{in} = q_{out}$$

$$losses \times P = q_T$$

$$losses \times V \times I = A_T \overline{h_T}(T_s - T_\infty) \tag{57}$$

Recall Equations 49 & 50 (chapter 2), the value of total average Nusselt number from the hemisphere surfaces can be written as follows

$$\overline{Nu}_{Total} = \frac{D}{kA_T}\left(\frac{q_T}{T_s - T_\infty}\right) \tag{58}$$

Figure 44 demonstrates the total values of experimental average Nusselt number, $\overline{Nu}_{Total}$ over the entire surfaces of the hemisphere (front and back) wherein ($\overline{Nu}_{Total} = \overline{Nu}_f + \overline{Nu}_b$). It is observed that the values of $\overline{Nu}_{Total}$ are Reynolds number dependent. In addition, the overall heat transfer rate yields a larger value at hemisphere tilt angle α = 52° at all Reynolds number, also the amount of total heat transfer from hemisphere surfaces decreases as the tilt angle, α decrease. The highest value of $\overline{Nu}_{Total}$ at α = 52° was ($\overline{Nu}_{Total}$ = 886.1) found at high Reynolds number, Re = 2.5×10^5. The overall heat transfer enhancement from the hemisphere at α = 52° is increased by an average of ≈ 5% in comparison to that at α = 30° and increased by around ≈ 8.3 % in comparison to that at α = 0°.

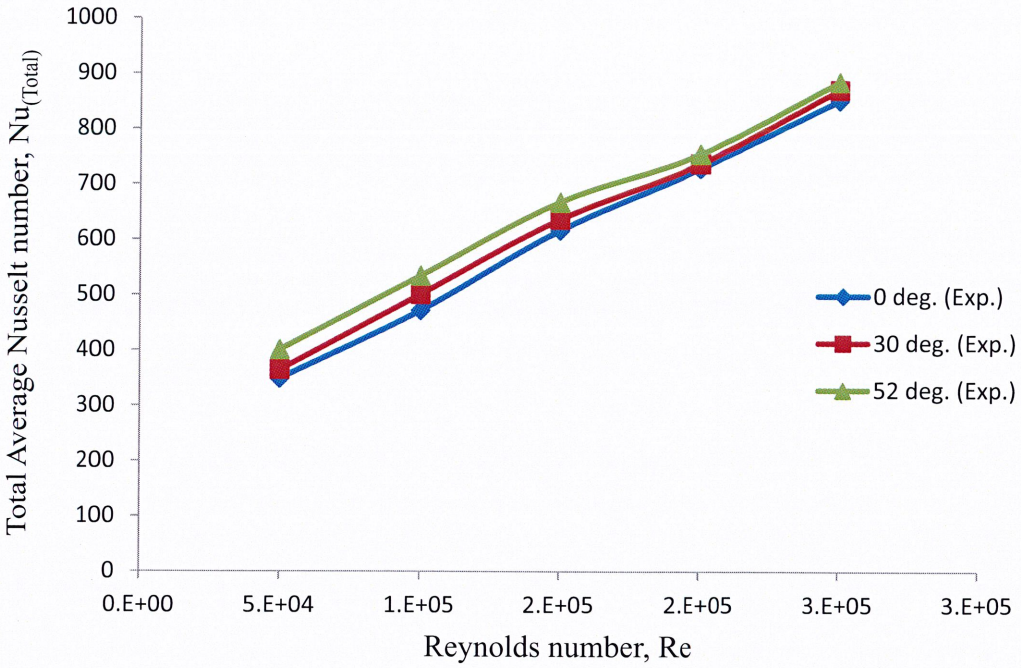


Figure 44: Experimental variations of total average Nusselt number, $\overline{Nu}_{(Total)}$ with Reynolds number of the hemisphere surfaces (front and back) for three different tilt angle ($\alpha = 0°$, $\alpha = 30°$ and $\alpha = 52°$)

4.2 Numerical Results

4.2.1 Mean Surface Pressure Coefficient

Figure 45 demonstrates the mean centerline pressure coefficient, Cp distribution plotted versus the stream-wise meridian angle, θ, on tilted hemisphere at $\alpha = 0°$. As noticed the negative coefficient of pressure values downwind and upwind of the hemisphere are symmetrical extending from $\theta = 0°$ to $\theta = 56°$ and from $\theta = 124°$ to $\theta = 180°$, respectively. Furthermore, the positive pressure coefficient values extend on the front surface between $\theta = 56°$ and $124°$ with the maximum Cp is observed to occur at $\theta = 90°$, which indicates the location of the stagnation point, and from this point the values of Cp decrease symmetrically towards the leading and trailing edge as a result of increasing of the flow acceleration over hemisphere stream-wise curvature due to the existence of a favorable pressure gradient. The negative maximum value of pressure coefficients are noticed to take place at $\theta \approx 12.6°$ and $\theta \approx 167.4°$ from the leading and trailing points, respectively, which indicates that high values of flow momentum occurs on these vicinities. It is also observed that the pressure coefficient variations is invariant to changes in Reynolds number at this orientation where $\alpha = 0°$. The separation point can be observed in the magnified velocity vectors plot on the trailing edge at $\theta = 180°$, in Figure 46. In addition, the snap shot of flow visualization photos taken from two different views as revealed in Figure 47, clearly capture the location of boundary layer separations at the leading and trailing edges of the hemisphere, at $\theta \approx 0°$ and $\theta \approx 180°$.

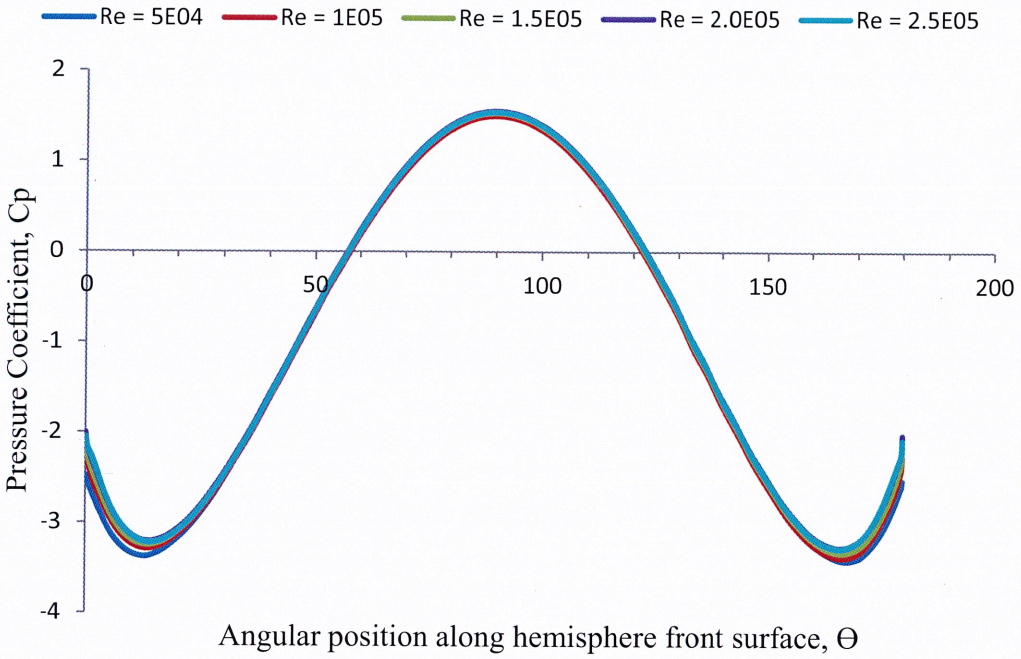


Figure 45: Pressure coefficient variations, Cp along hemisphere stream-wise front surface at $\alpha = 0°$

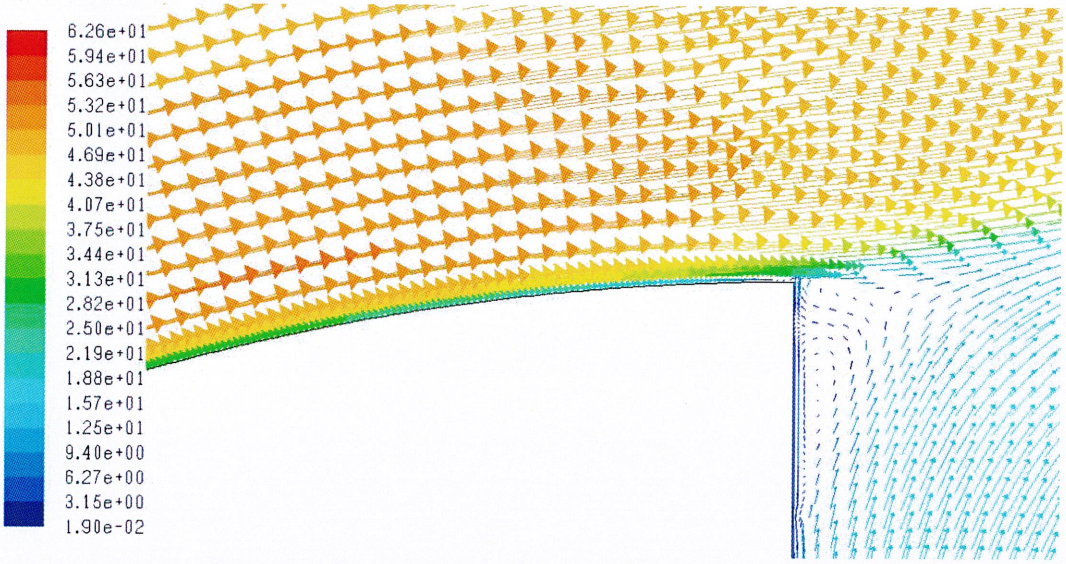
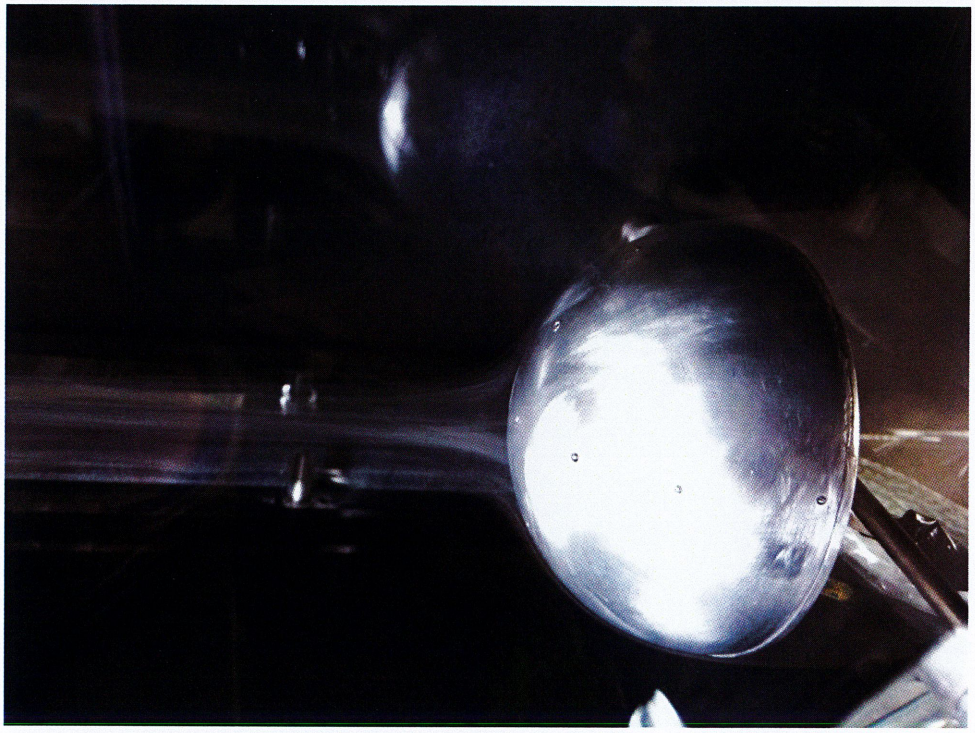


Figure 46: Velocity vectors on the trailing edge at Re = 2.5×10^5 for $\alpha = 0°$



(a)



(b)

Figure 47: Smoke generated flow visualization around hemisphere at $\alpha = 0°$ taken from two views (a) side, (b) front

At a tilt angle of $\alpha = 30°$, the negative maximum pressure coefficient is shifted at the leading edge point, $\theta = 0°$, as shown in Figure 48, which revealed the existence of high flow momentum. In addition, the negative pressure values span over the front surface from $\theta = 0°$ to $\theta \approx 32°$ at the downwind face of the hemisphere, and from $\theta \approx 95.7°$, 96.8°, 98°, 99° and 100° to $\theta = 180°$, at the upwind face corresponding to Reynolds numbers 0.5×10^5, 1.0×10^5, 1.5×10^5, 2.0×10^5 and 2.5×10^5, respectively. The negative pressures gradually recover reaching approximately a stable value at $\theta \approx 167.3°$ which can be clearly noticed at the highest Reynolds number, $Re = 2.5\times10^5$, which indicates the point of separation near the trailing edge and the beginning of the wake region. It is also observed that as Reynolds number increases the negative pressure values recover earlier and reach a stable value indicating an early point of separation, which occurs at $\theta \approx 171.5°$, 171°, 170.54°, 169.79° and 167.3°, respectively. The positive pressure at this tilt angle, $\alpha = 30°$ extend from $\theta \approx 32°$ to $\theta \approx 95.7°$, 96.8°, 98°, 99° and 100° corresponding to Reynolds number 0.5×10^5, 1.0×10^5, 1.5×10^5, 2.0×10^5 and 2.5×10^5, respectively, with a maximum positive pressure coefficient occurring at $\theta \approx 63.8°$ that indicates the stagnation point vicinity. The effect of Reynolds number on the upwind surface of the negative pressure variations is more pronounced, than that at the downwind face. The highest negative pressure values are observed at $Re = 0.5\times10^5$ and these values decrease as Re values increases. The separation point can be also noticed in Figure 49 (a), the magnified velocity vector plot near the trailing point at $\theta \approx 167.3°$, at $Re = 2.5\times10^5$ while at the leading point the flow separation only occurs at $\theta = 0°$, as shown in Figure 49 (b). Moreover, the snap shot of experimental flow visualization photo shown in Figure 50 (b) clearly capture the location of

flow separation near the trailing edge which is estimated to occur at $\theta \approx 165°$, while the flow separation on the leading edge found to be at $\theta = 0°$. In addition, the stagnation point estimated to occur at $\theta \approx 61°$ as shown in Figure 50 (a) & (b).

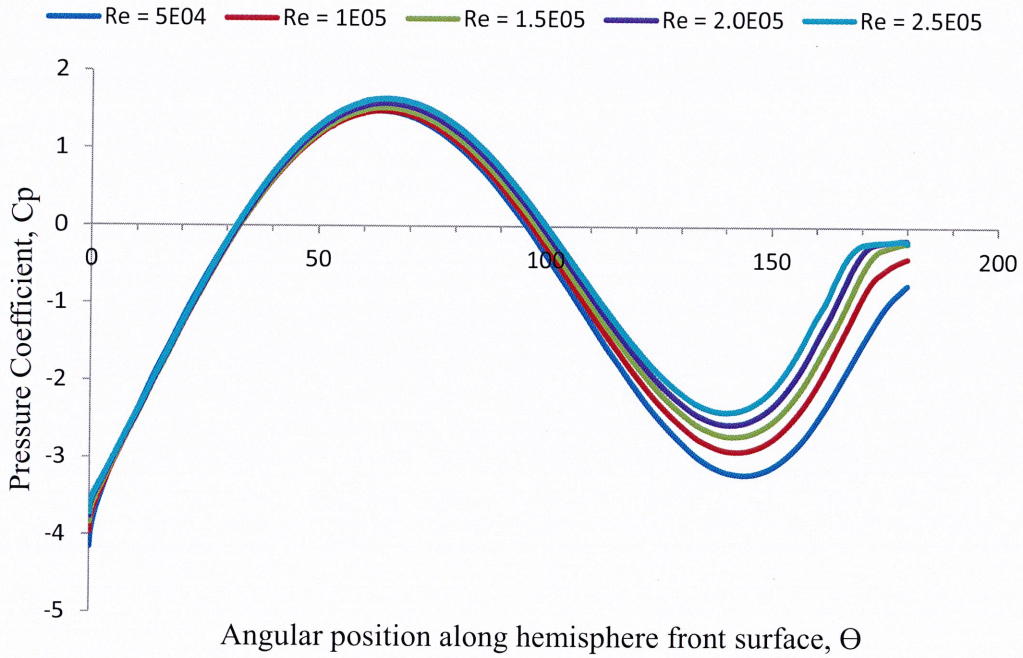
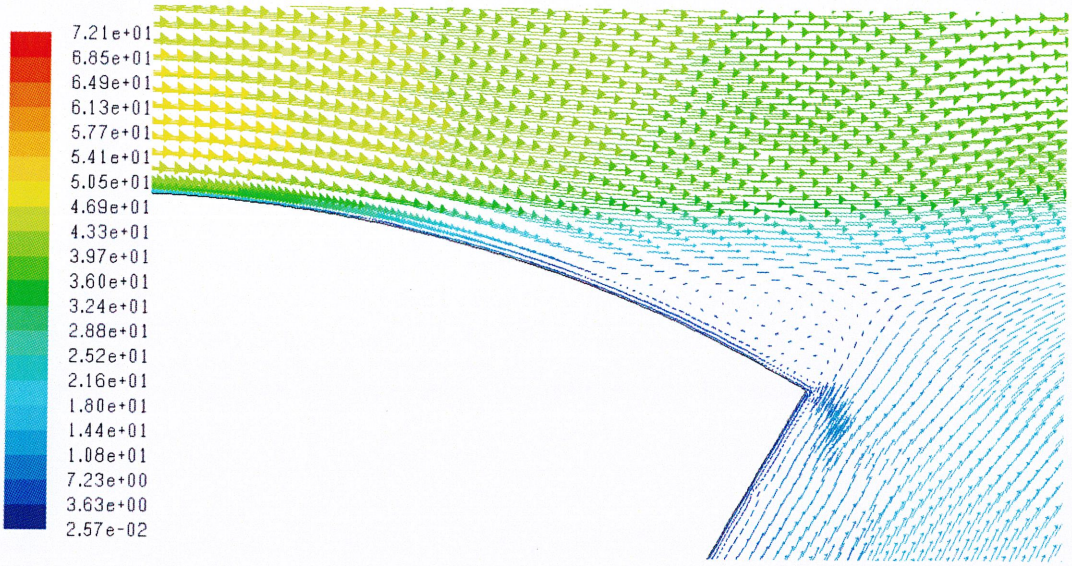
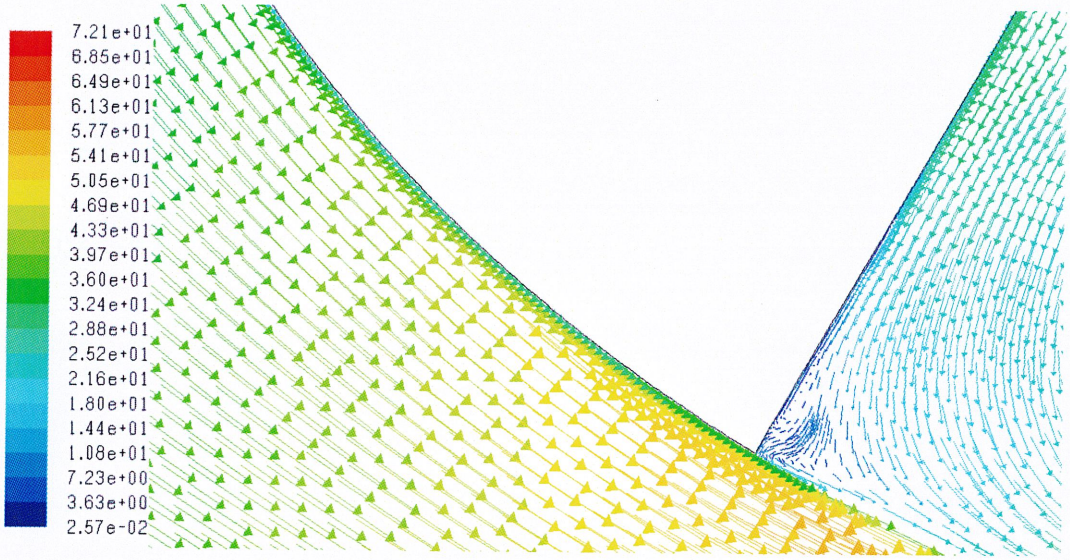


Figure 48: Pressure coefficient variations, *Cp* along hemisphere stream-wise front surface at $\alpha = 30°$

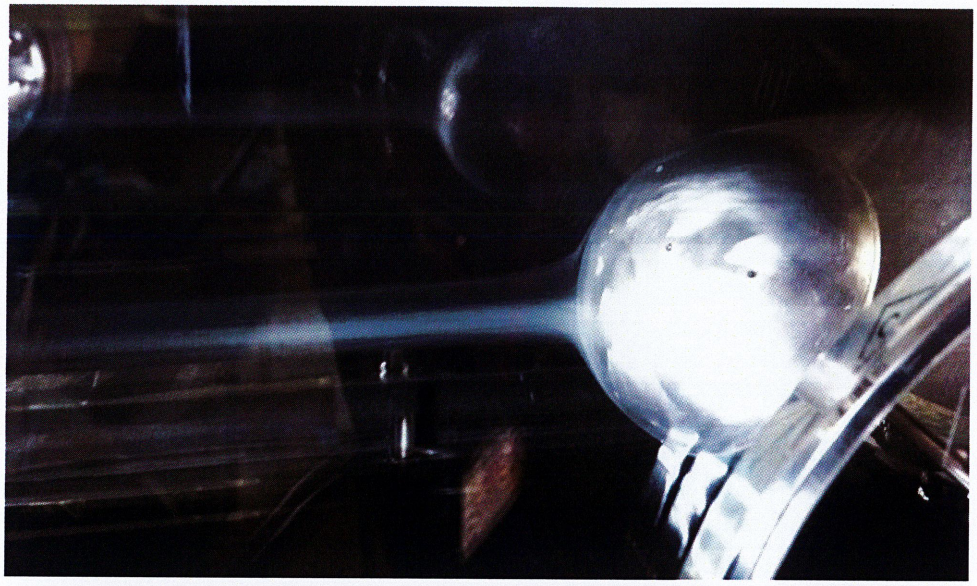


(a)



(b)

Figure 49: Velocity vectors over hemisphere (a) trailing edge, and (b) leading edge at $Re = 2.5\times10^5$ for tilt angle $\alpha = 30°$



(a)



(b)

Figure 50: Smoke generated flow visualization around hemisphere showing separation flow on the trailing surface, taken from two views for tilt angle $\alpha = 30°$

Figure 51 depicts pressure coefficient distribution, Cp as a function of stream-wise meridian angle, θ, of front surface of hemisphere tilted at $\alpha = 52°$. The negative pressures advance further toward the leading point on the downwind face from $\theta = 0°$ to $18°$ for all Reynolds number. Similarly on the upwind face these pressures span from $\theta = 78.9° - 157.5°$ for $Re = 0.5\times10^5$, $\theta = 84.5° - 159.8°$ for $Re = 1.0\times10^5$, $\theta = 81.8° - 154.9°$ for $Re = 1.5\times10^5$, $\theta = 83° - 150.5°$ for $Re = 2.0\times10^5$ and $\theta = 81.5° - 146.8°$ for $Re = 2.5\times10^5$ indicating recovery and stability and the beginning of boundary layer separation which occurs at $\theta \approx 157.5°$, $159.8°$, $154.9°$, $150.5°$ and $146.8°$ for the corresponding Reynolds number 0.5×10^5, 1.0×10^5, 1.5×10^5, 2.0×10^5 and 2.5×10^5, respectively. The maximum positive pressure occurs at the stagnation point where $\theta \approx 47°$. The separation point can be also noticed in Figure 52 (a), the magnified velocity vector plot near the trailing edge at $\theta \approx 146.8°$, at $Re = 2.5\times10^5$, and at the leading point occurs at $\theta = 0°$, as shown in Figure 52 (b). Furthermore, the snap shot of experimental flow visualization photo shown in Figure 53 clearly captures the location of boundary layer separation near the trailing edge which is estimated to occur at $\theta \approx 148°$, while on the leading edge found to be at $\theta = 0°$. In addition, the stagnation point is estimated to occur at $\theta \approx 45°$ as shown in the photo. It is observed from Figures (45, 48 and 51) that the negative pressure values increase at the leading edge as the tilt angle, α of the hemisphere increases. This increase is estimated at 18% at $\alpha = 30°$ and 56% at $\alpha = 52°$ from that at $\alpha = 0°$. These higher values in Cp indicate an increase in flow momentum in this region and thus larger heat transfer enhancement compared to other parts of the hemisphere surface.

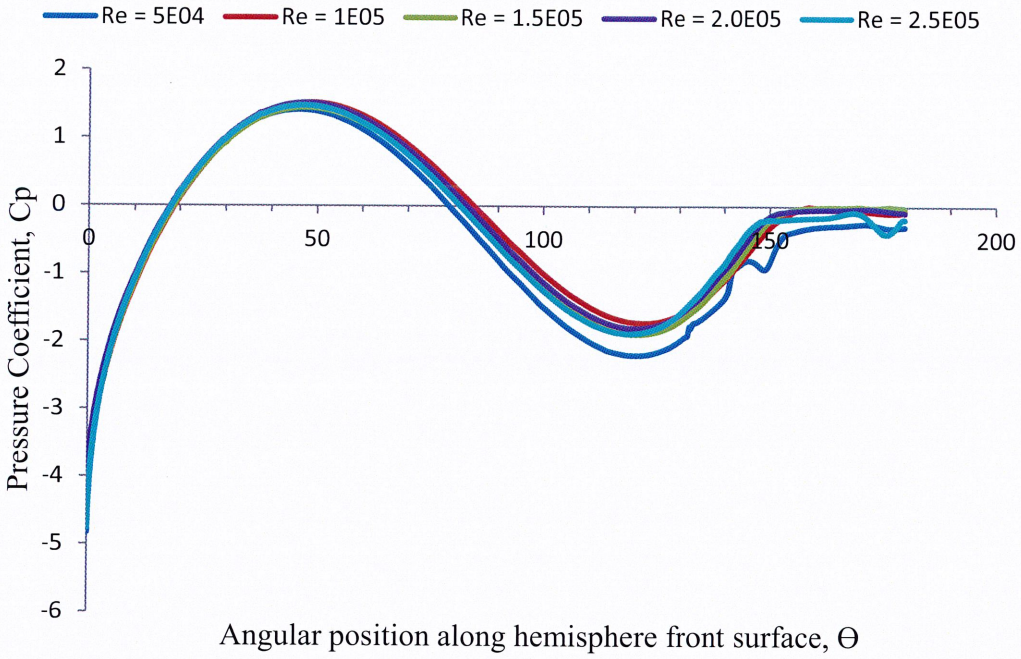
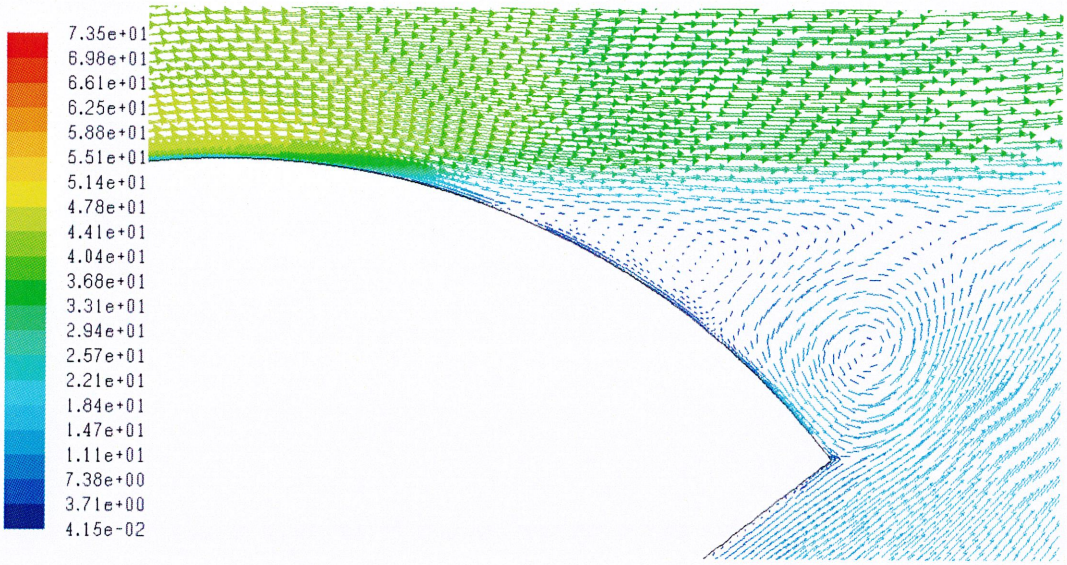
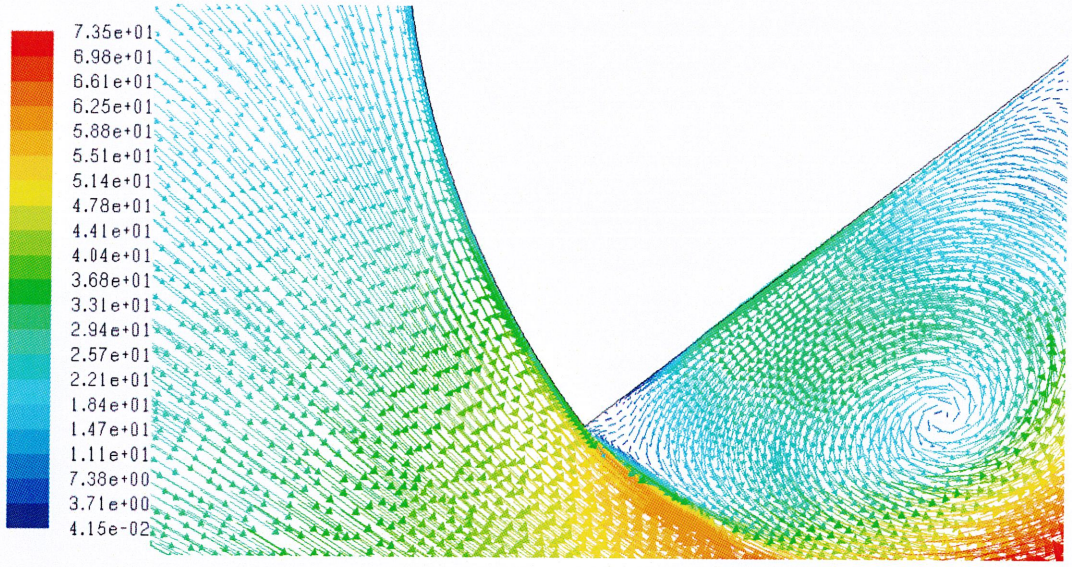


Figure 51: Pressure coefficient variations, *Cp* along hemisphere stream-wise front surface at $\alpha = 52°$



(a)



(b)

Figure 52: Velocity vectors over hemisphere (a) trailing edge, and (b) leading edge at $Re = 2.5\times10^5$ for tilt angle $\alpha = 52°$

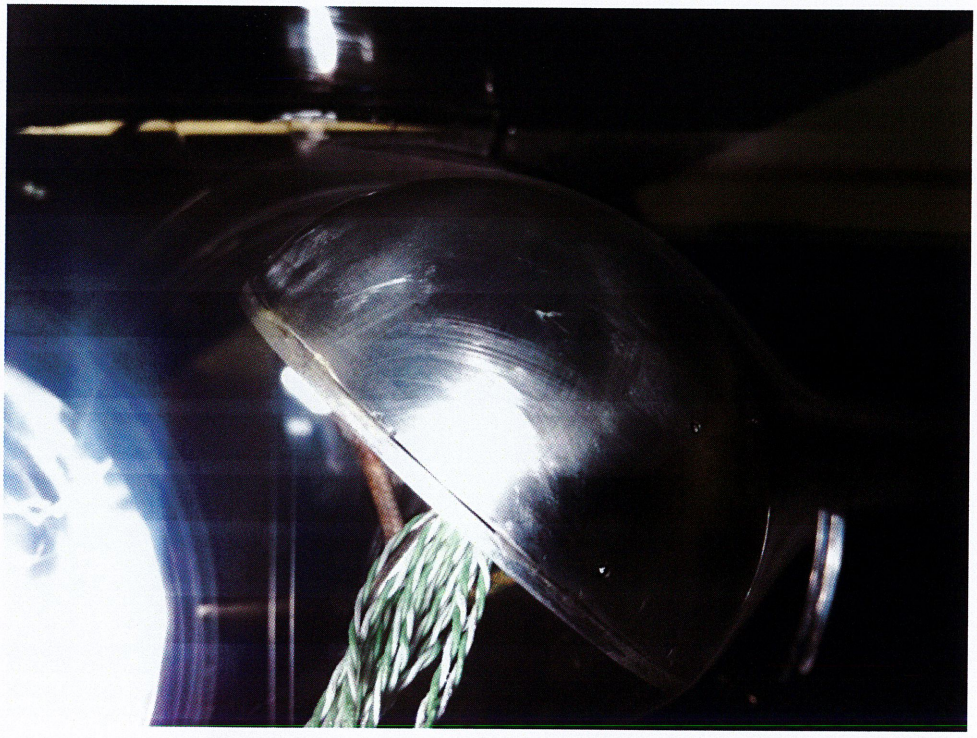


Figure 53: Smoke generated flow visualization around hemisphere showing separation flow on the trailing surface, for tilt angle $\alpha = 52°$

4.2.2 Shear Stress

Figure 54 illustrates shear stress variations, τ_{wf} along stream-wise angular direction, θ for the hemisphere tilted at $\alpha = 0°$. As can be seen, a symmetrical shear stress variations are revealed on the front surface of the hemisphere at this configuration, with a minimal shear values noted at the leading and trailing point, $\theta = 0°$ and $\theta \approx 180°$, respectively, where the boundary layer separation takes place. Also, zero shear values is observed at the stagnation point $\theta \approx 90°$, which is attributed to zero velocity magnitude at the hemisphere apex surface. Conversely, maximum shear stress values are observed at $\theta \approx 23°$ at the front surface leading point, and at $\theta \approx 156.6°$ near trailing point, owing to high flow momentum and velocity gradients at these vicinities. It's obvious that as the Reynolds number increases the skin friction increases on the surface.

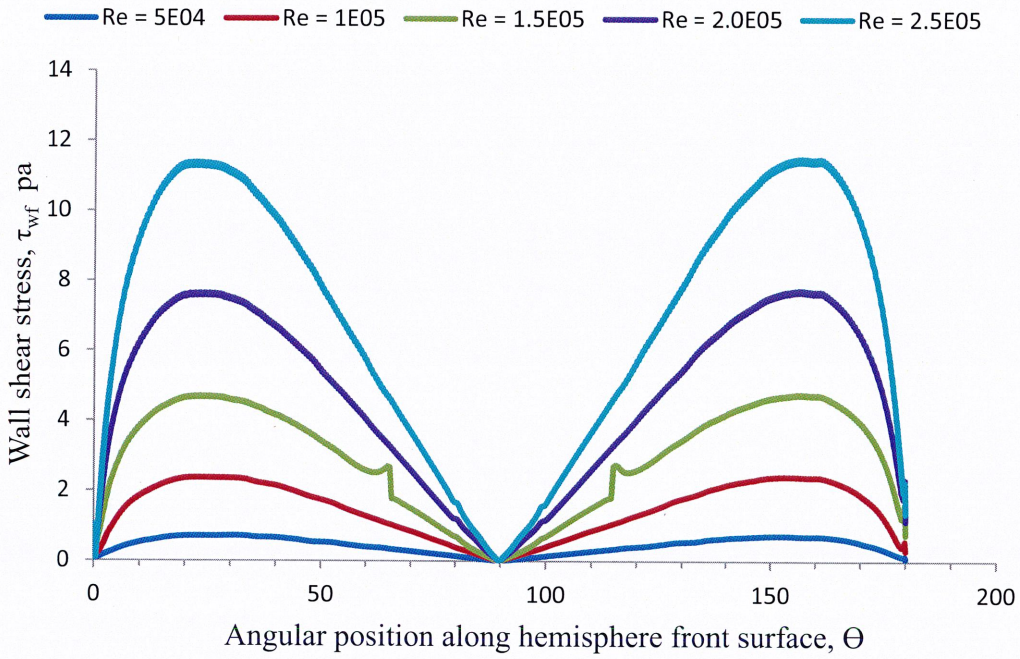


Figure 54: Shear stress variations, τ_{wf} along hemisphere stream-wise front surface at $\alpha = 0°$

Largest values of skin friction are noted near the leading point, namely at $\theta \approx 0.15°$, i.e. just before occurring of boundary layer separation, when the hemisphere is tilted at $\alpha = 30°$ as revealed in Figure 55, therefore the absence of flow separation contribute to the gradual increase in shear stress value as the fluid accelerates over stream-wise direction. The shear stress becomes zero at the stagnation point at $\theta \approx 63.8°$ for all given Reynolds number values, as well as near the trailing edge where an early boundary separation takes place. It is observed that as Reynolds number increases the separation point occurs earlier. In addition, as Reynolds number increases the skin friction increases on the hemisphere surface. It can be also noted that the maximum shear stress values at upwind face near the trailing edge occur at $\theta \approx 130°$ for all Reynolds numbers. Afterward the values of shear stress sharply decrease towards the trailing edge due to loss in flow momentum owing to increase in adverse pressure gradient in this region.

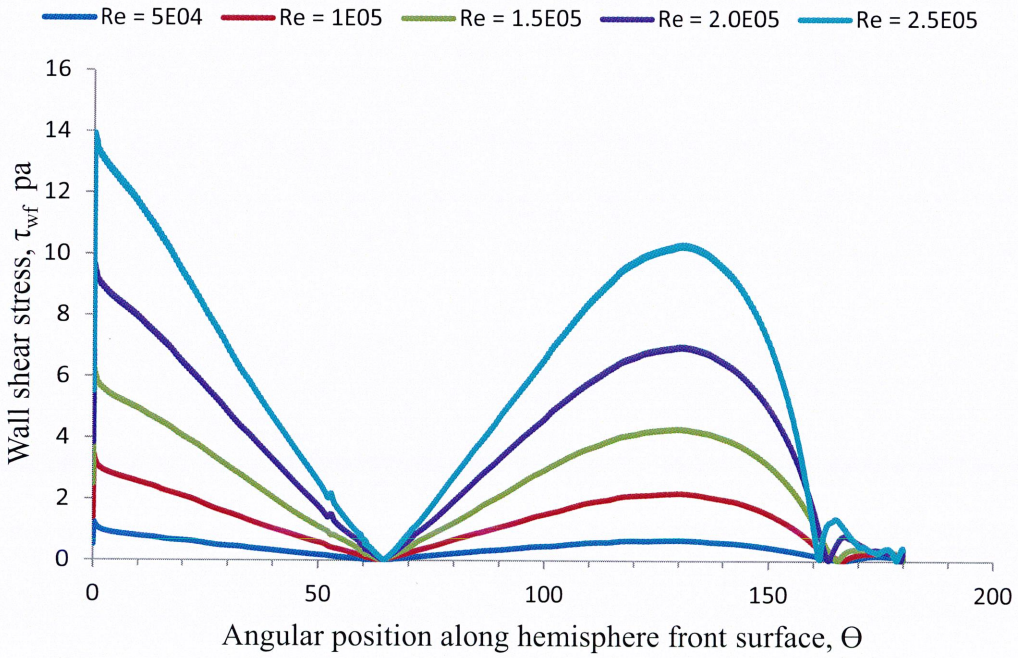


Figure 55: Shear stress variations, τ_{wf} along hemisphere stream-wise front surface at $\alpha = 30°$

The skin friction values increase further near the leading edge in the stream-wise direction when the hemisphere is tilted at $\alpha = 52°$ as shown in Figure 56. Moreover the zero shear stress values move towards the leading edge at stagnation point $\theta \approx 47°$, and at the boundary layer separation point near the trailing edge at $\theta \approx 140°$. Highest values of shear stress τ_{wf} are also noted at upwind face $\theta \approx 108°$ for all Reynolds number. The multi-peaks phenomena depicted at the beginning of the wake region at $\theta \approx 140°$ near the trailing edge suggests transition of separated free shear layer occurred and a separation bubble is formed at this stage. The first and second peaks indicate the locations of separation and reattachment/rear separation, with increasing Reynolds number the magnitude of the peak suction continuously increase whilst, the wake pressure suction decreases. Similarly as Reynolds number increases the skin friction values increase. It is noted that the boundary layer separation takes place earlier in this configuration.

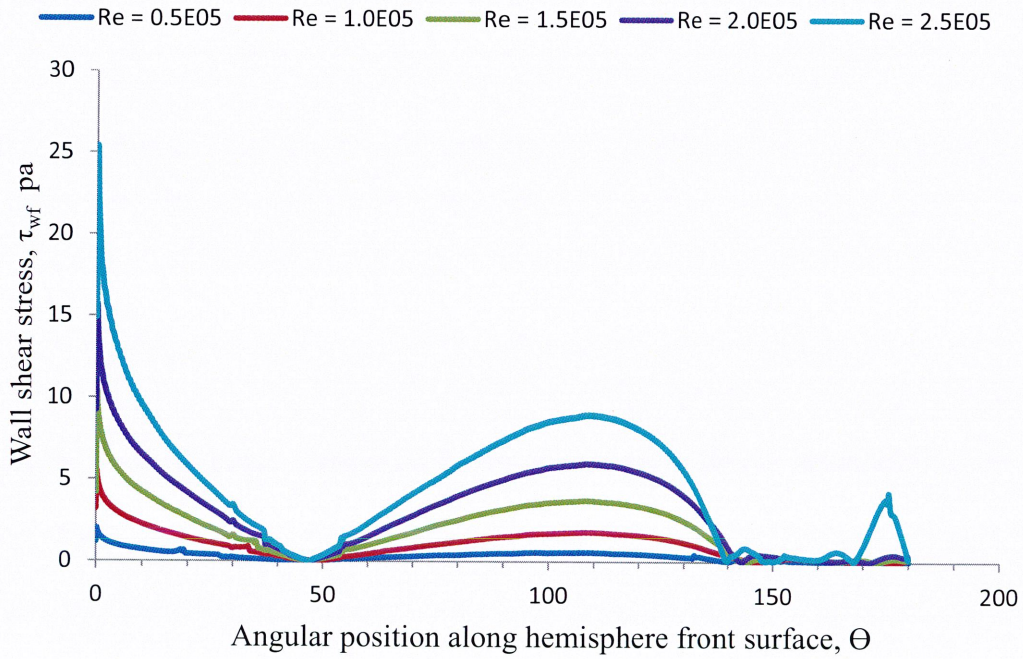


Figure 56: Shear stress variations, τ_{wf} along hemisphere back surface at $\alpha = 52°$

4.2.3 Local Nusselt Number

4.2.3.1 Stream-wise Direction

Numerical results for the variation of local Nusselt number, Nu_θ with meridian angle, θ are shown in Figure 57, for hemisphere stream-wise direction and tilt angle $\alpha = 0°$. As revealed, the results of local Nusselt number, Nu_θ are strongly influenced by Reynolds number, so as Re increases Nu_θ increases. This is attributed to a corresponding reduction in the boundary layer thickness over the surface. The heat transfer enhancement has shown an identical variation on both half of the stream-wise section due to symmetry. The lowest Nu_θ being at the stagnation point at $\theta \approx 90°$ where the flow velocity at it is minimal values, afterward, Nu_θ gradually increases towards the leading and trailing edge of the hemisphere as a result of boundary layer development encountered with the increase of flow momentum, subsequently, the maximum enhancement in heat transfer dissipation over the surface is observed to occur at $\theta \approx 19.2°$ and $\theta \approx 161.4°$ in the downwind and upwind faces, respectively. However, beyond these points, Nu_θ decreases up to minimum values at the leading and trailing points where separation occurs, which indicates the beginning of the wake region.

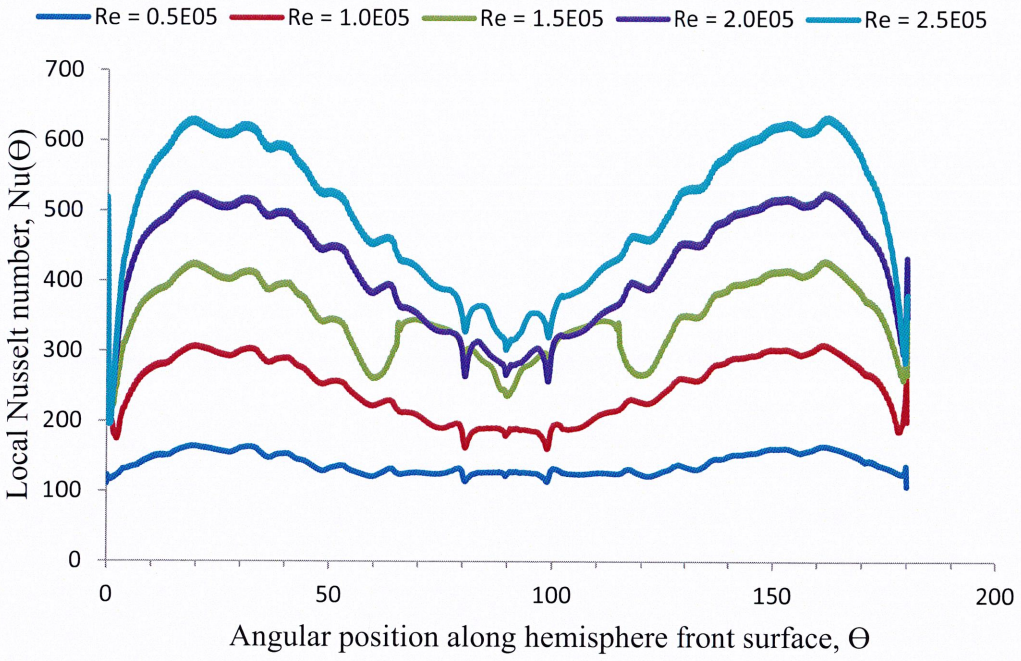


Figure 57: Local Nusselt number variations along hemisphere stream-wise front surface at α = 0°

Figure 58 shows the heat transfer is largest at the leading edge of the hemisphere surface at α = 30° tilt angle. The stagnation point has moved towards the leading edge at $\theta \approx 63°$ where the heat transfer is lowest. The highest value of Nu_θ at the upwind face is observed to occur earlier at $\theta \approx 131°$ for all Reynolds number comparing to that at tilt angle α = 0°. Furthermore, the heat transfer is observed to decrease at the point of boundary layer separation as at $\theta \approx 167.3°$ for ($Re = 2.5\times10^5$) near the end of the trailing edge where a strong adverse pressure gradient and reverse flow takes place leading to thick boundary layer and lower cooling effect on this zone. The multi-peaks phenomenon in Nu_θ depicted beyond separation points owing to the mixing associated with vortex formation in the wake region. It is noted that, as Reynolds number increases, the boundary layer separation takes place earlier on the trailing

edge. It is also noted that heat transfer enhancement increases at larger Re values.

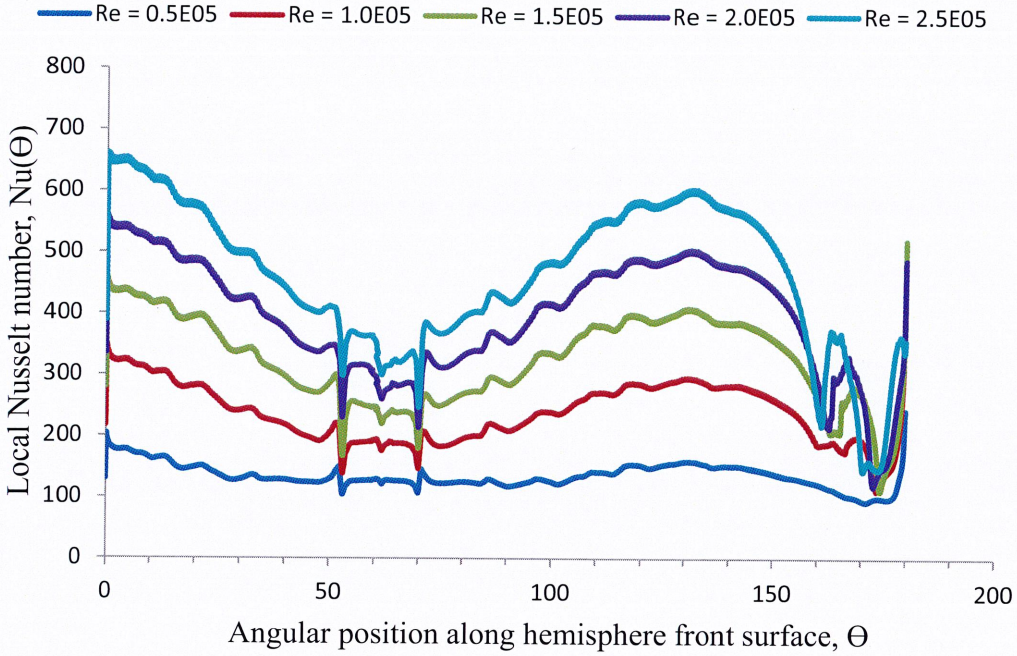


Figure 58: Local Nusselt number variations along hemisphere stream-wise front surface at α = 30°

At tilt angle α = 52°, the trends of local Nusselt number, Nu_θ in Figure 59 shows that the stagnation and separation points have moved further towards the leading edge compared to the previous configurations α (0°, 30°). The stagnation point takes place at θ ≈ 47° and the boundary layer separation at highest Re occurs approximately at $\theta \approx$ 146°. It is also observed that highest heat transfer enhancement occurs at the point near the leading edge (downwind) θ ≈ 0.15° just before separation, which is found to be higher than that in the previous configurations α (0°, 30°) by about 49 % and 30 %, respectively, and these variations are evaluated at the highest Reynolds number, Re = 2.5×10^5. In contrast, the heat transfer enhancement at the upwind face of the hemisphere towards the trailing edge has experienced a lesser amount

in heat dissipation compared to the previous configurations α (0°, 30°) by about 9.7 % and 5 %, respectively, at Re = 2.5×10^5. A prominent region can be observed after flow separations near the trailing edge in which the multi-peaks of Nu_θ increase due to an early transition of separated shear layer to turbulence, which is in addition induced by mixing phenomenon in the wake region.

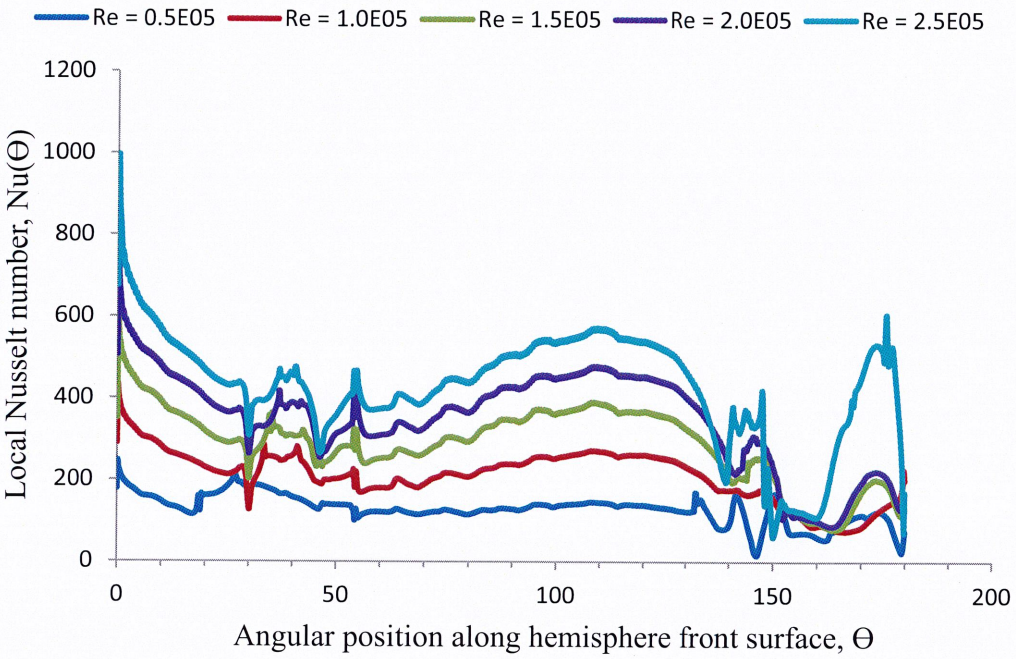


Figure 59: Local Nusselt number variations along hemisphere stream-wise front surface at α = 52°

4.2.3.2 Back Surface of the Hemisphere

Figure 60 depicts the local Nusselt number variations, Nu_y on the back surface of the hemisphere tilted at α = 0°. It may be observed that there is symmetry in Nu_y distribution on the back surface for $0 \leq y \leq$ 0.0325 and $0 \geq y \geq$ -0.0325 at upper and lower half section, respectively. Also it is observed that the values of Nu_y increase with Reynolds number. It can be noticed that for all Re values the lowest heat transfer

rate occurs at the middle of back surface ($y = 0$) due to decrease in the velocity magnitude as well as flow mixing. Furthermore, the value of Nu_y along the surface fluctuates and takes low and high peaks from the centre towards leading and trailing edge, which can be related to presence of flow recirculation phenomena at the back of the hemisphere. It may be also noted that the highest heat transfer rate occurs near the leading and trailing points (y = -0.0325, 0.0325), respectively, and this is due to the presence of strong recirculation flows and large velocity magnitude.

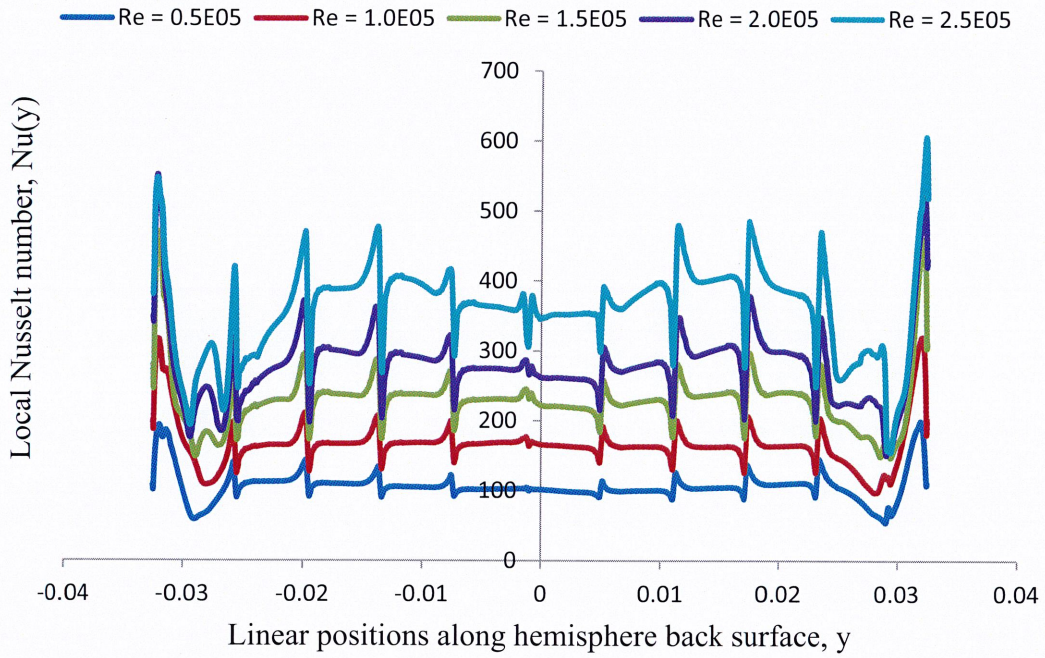


Figure 60: Local Nusselt number variations along hemisphere back surface at α = 0°

At larger tilt angle, namely at α = 30° as shown in Figure 61, it is observed that the local Nusselt number, Nu_x on the back lower surface from the center towards the leading edge for $0 \geq x \geq$ -0.01625 increases gradually and reaching a maximum value just before the tip of the edge. The above behavior is owing to high recirculation flows on the leading edge back surface, that is enhanced by the delay of boundary layer

separation on the front surface in the downwind face that occurs at $\theta = 0°$. In contrast, on the upper back surface from the center towards the trailing edge for $0 \leq x \leq 0.01625$, has shown lower heat transfer rate in comparison with the lower surface from the center towards the leading edge, this is attributed to an early boundary layer separation that occurs on the front surface near trailing edge of the upwind face which in turn reduces flow momentum beyond the separation point, and hence the recirculation phenomenon at the upper half section of back surface reduces as well.

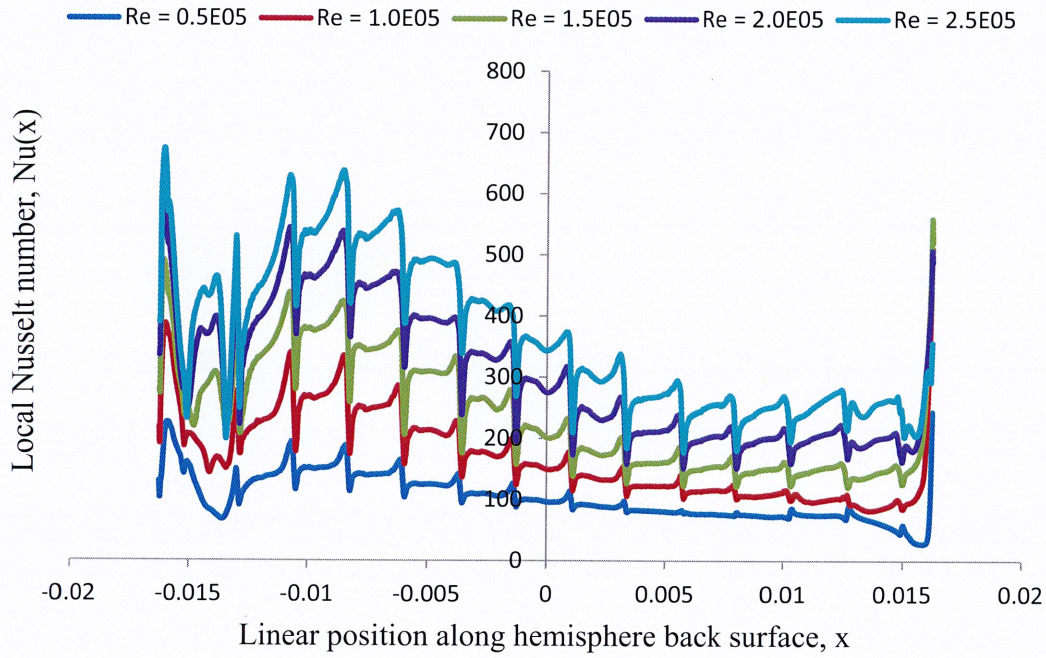


Figure 61: Local Nusselt number variations along hemisphere back surface at $\alpha = 30°$

With further increase in the tilt angle of the hemisphere specifically at $\alpha = 52°$, has shown that the values of local Nusselt number, Nu_x increase more on the lower surface for $0 \geq x \geq -0.02571$ as shown in Figure 62, this is attributed to further increase in the velocity magnitude of the fluid over front surface from stagnation point towards the leading

point, which in turn contributes to generate a region of strong recirculation downstream of lower surface. The result of the aforementioned behavior is more pronounced at larger Reynolds number $Re = 2.5\times10^5$, wherein a highest value of local Nusselt number ($Nu_x = 1261.41$) takes place at (x = -0.01337 m). On the other hand, the variation of Nu_x decreases further at the upper surface for $0 \leq x \leq 0.02571$, due to an earlier flow separation on the trailing upwind face of the hemisphere. Thereby the flow momentum and recirculation reduce further in the wake region at the upper back surface.

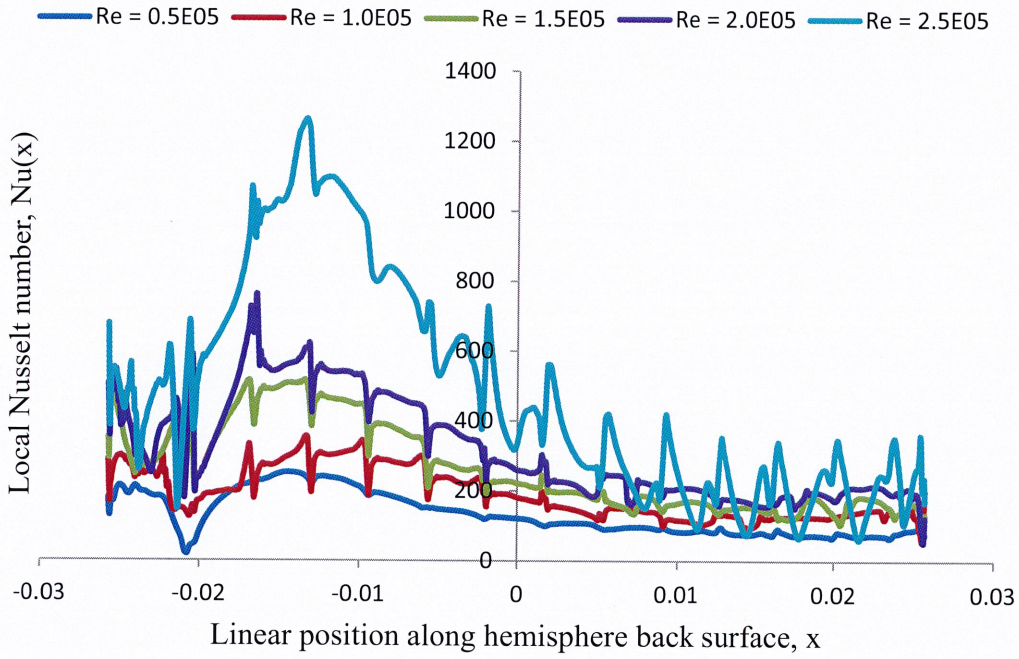


Figure 62: Local Nusselt number variations along hemisphere back surface at α = 52°

4.2.4 Average Nusselt Number

Figure 63 demonstrates average Nusselt number, $\overline{Nu_f}$ over hemisphere stream-wise direction of front surface as a function of Reynolds number, for the three tilt angles, (α). It is observed that heat transfer rate is largest when the hemisphere is un-tilted where α = 0°, and

decreases as it is positioned to unfavorable angle of attack to the flow stream namely at $\alpha = 30°$ and $\alpha = 52°$. This decrease in heat transfer rate for the aforementioned tilted models is attributed to the presence of an early boundary layer separation as a result of adverse pressure gradient near the trailing edge of the front surface, in which the flow momentum in the wake region originated beyond the point of separation becomes low towards trailing point, thereby the heat transfer enhancement at this vicinity is sharply reduced. On the contrary, larger heat transfer rate from front surface for the un-tilted model is due to well-built velocity gradient over front surface starting from stagnation point towards both leading and trailing edges along with the absence of boundary layer separation over the surface. It is also noticed that heat transfer rate increases with an increase in Reynolds number.

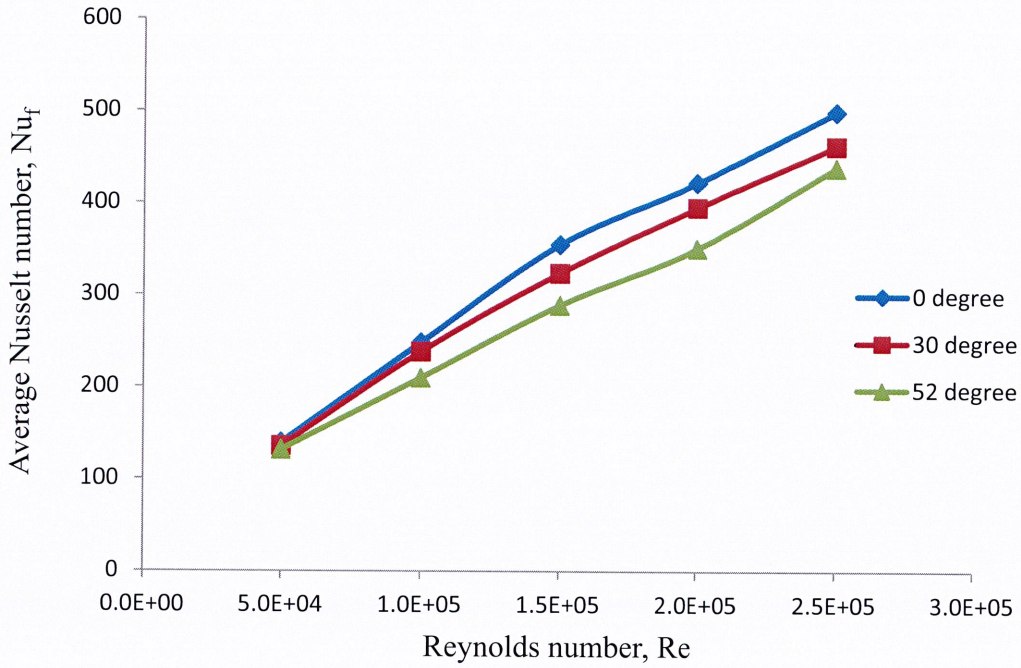


Figure 63: Variations of average Nusselt number, $\overline{Nu_f}$ with Reynolds number of the hemisphere stream-wise direction of front surface for three different orientations ($\alpha = 0°$, $\alpha = 30°$ and $\alpha = 52°$)

A correlations between front surface (stream-wise) average Nusselt number, $\overline{Nu}_f$ and Reynolds number, Re are obtained for the hemisphere at the three different configurations, ($\alpha = 0°$, $\alpha = 30°$ and $\alpha = 52°$) as shown in Figure 64. The slope of each configuration is determined for each linear plot and shown in the graph. As can be observed, that the results fall close to straight line which indicate a power law dependence of the average Nusselt number on the Reynolds number.

Figure 65 elucidates average Nusselt number, $\overline{Nu}_b$ over the back surface of the hemisphere as a function of Reynolds number at the three different tilt angles, (α). It can be noticed that the value of average Nusselt number, $\overline{Nu}_b$ increases with Reynolds values. However the heat transfer enhancement process is reversed on the back surface of the hemisphere in comparison to the front surface, wherein a highest trends of $\overline{Nu}_b$ is observed at higher tilt angle $\alpha = 52°$, while the heat transfer rate reduces with the decrease in the tilt angle, (α). The reason behind increasing of heat transfer rate at the back surface at the higher tilt angle ($\alpha = 52°$) is attributed to the strong recirculation flows and larger velocity magnitude specifically on the lower surface downstream of the hemisphere, in comparison to that observed at $\alpha = 0°$ and $\alpha = 30°$.

Figure 66 depicts the overall numerical average Nusselt number, $\overline{Nu}_{Total}$ over the entire surfaces of the hemisphere. In which, the total average Nusselt number is the sum of both stream-wise front surface and back surface average Nusselt numbers, ($\overline{Nu}_{Total} = \overline{Nu}_f + \overline{Nu}_b$). It is observed that the overall heat transfer rate yields a larger value at hemisphere tilt angle $\alpha = 52°$, namely at the highest Reynolds number, $Re = 2.5 \times 10^5$, where the increase in the heat transfer rate is more explicit in comparison to lower tilt angles, (α), in which the total average Nusselt

number found equal to, ($\overline{Nu}_{Total}$ = 956.6). The enhancement in the heat transfer rate in this condition is greater by an average of ≈ 9 % in comparison to that at α = 30° and ≈ 6 % to that at α = 0°.

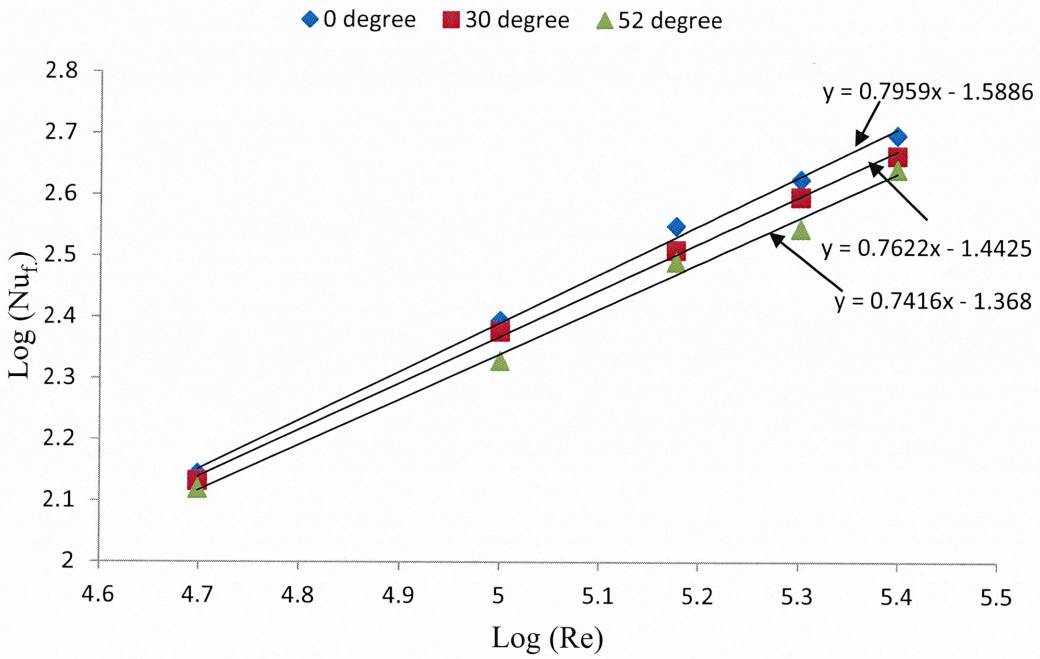


Figure 64: Correlation between stream-wise average Nusselt number, $\overline{Nu}_f$ and Reynolds number at different hemisphere tilt angle (α = 0°, α = 30° and α = 52°)

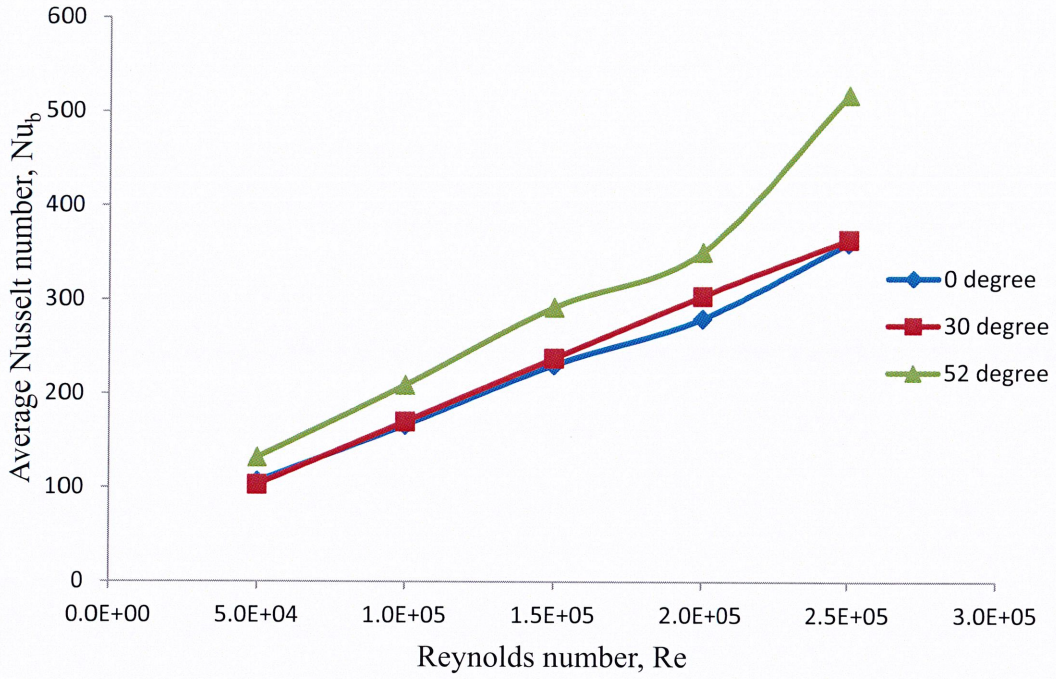


Figure 65: Variations of average Nusselt number, $\overline{Nu_b}$ with Reynolds number of the hemisphere back surface for three different orientations ($\alpha = 0°$, $\alpha = 30°$ and $\alpha = 52°$)

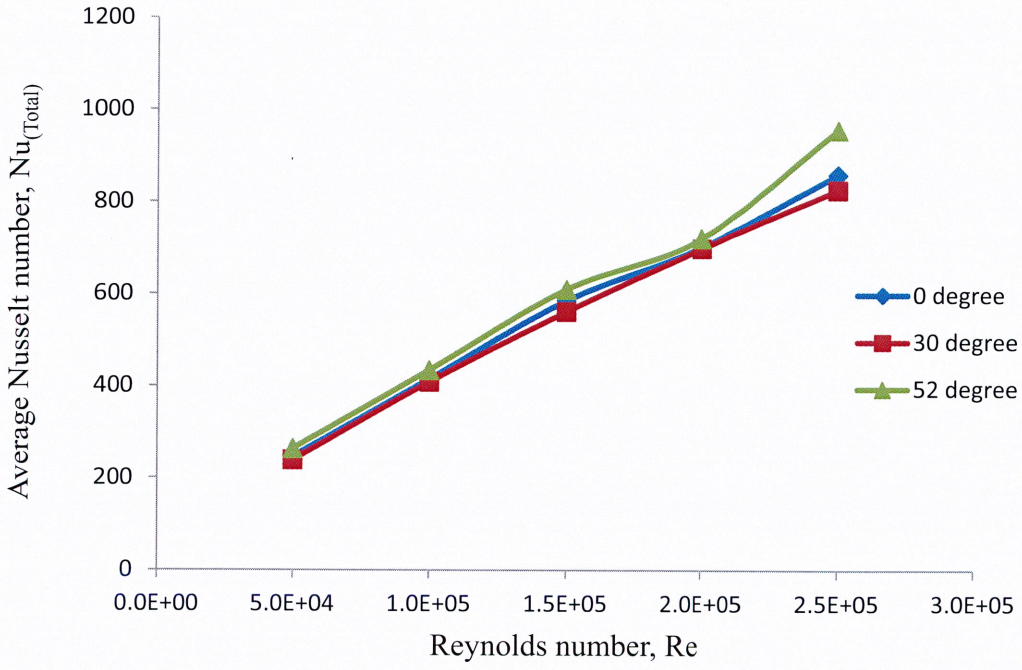


Figure 66: Variations of total average Nusselt number with Reynolds number over hemisphere front and back surface for three different orientations ($\alpha = 0°$, $\alpha = 30°$ and $\alpha = 52°$)

4.2.5 Velocity Contour

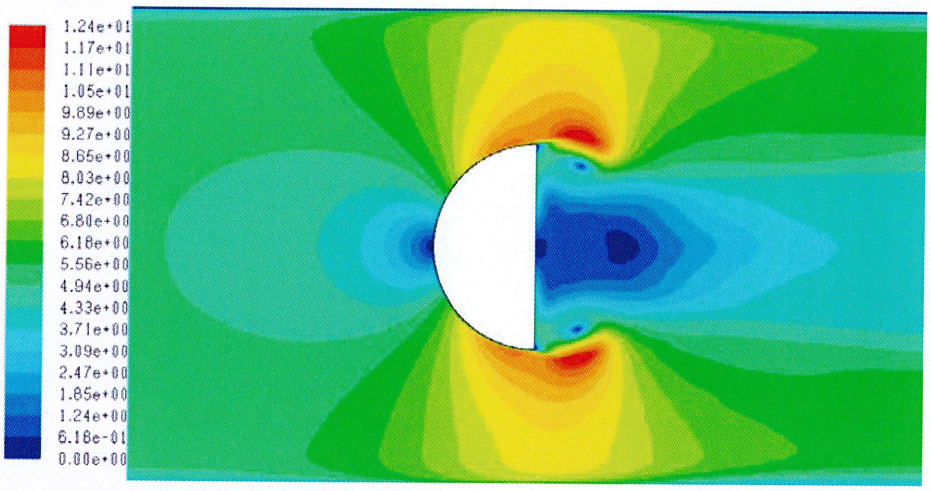
In order to provide a better understanding of the heat transfer enhancement over the hemisphere, velocity contours are presented. Figure 67 demonstrates the velocity magnitude over hemisphere stream-wise section at various Reynolds number for hemisphere tilted at $\alpha = 0°$. It can be seen in the Figure 67 from (a) to (e), that the increasing of the fluid velocity at the inlet boundary causes the fluid to accelerate rapidly over the obstacle front surface due to the existence of favorable pressure gradient, starting at minimal velocity value at stagnation point located at $\theta = 90°$ towards the leading and trailing edges, $\theta = 0°$ and $\theta = 180°$, respectively, in which a maximum local velocity over the obstacle is reported, as well as wherein the flow separation. It can be noticed that the higher velocity magnitude region is dominant in the upstream region of the hemisphere. Conversely, at the downstream of the hemisphere the lower velocity magnitude is observed more due to strong suction induced by recirculation flows downstream of the hemisphere. It is also noticed that as the velocity increases at the inlet boundary the flow momentum after fluid separation near the leading and trailing points increase, and accordingly, high recirculation flows take place in the wake region near the leading and trailing edge. Moreover, the reattachment length behind the hemisphere extends further far away from back surface as the incoming flow velocity increase, which is strongly dependent on the Reynolds number.

In Figure 68 (a-e), shows hemisphere positioned at tilt angle $\alpha = 30°$, it is shown that the stagnation point moves further towards the downwind side near the leading edge at $\theta \approx 63.8°$. In this orientation, the maximum local velocity magnitude is observed to occur only near the leading edge, due to no boundary layer separation to the fluid, in which it

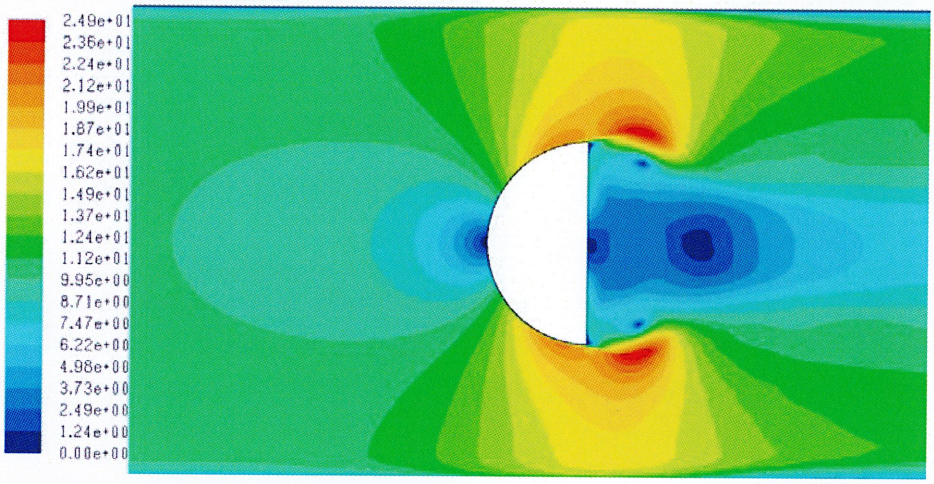
is expected to have higher cooling effect at this vicinity. In contrast, it's observed that a reverse flow near the trailing edge , which reveals the presence of flow separation, due to high adverse pressure gradient that results in fluid flow over the obstacle to lose its momentum causing it to separate, $\theta \approx 167.3°$. Moreover, the boundary layer separation is Reynolds number dependent, in which as *Re* increases an early flow separation is expected to occur. It can be noticed that minimal values of velocity magnitude take place behind hemisphere at upper half portion. Accordingly a lower heat transfer rate is reported in this region, this can be explained to an early boundary layer separation on the front surface. Conversely, strong flow recirculation found at the lower half portion behind hemisphere, due to high flow recirculation and mixing after flow separation which is noted at $\theta = 0°$, thus the heat transfer enhancement is higher in this region. The flow momentum near the leading edge in this configuration $\alpha = 30°$ increased by around 15.22% in comparison with no tilt condition $\alpha = 0°$ for the five *Re* values.

In Figure 69 (a-e), as the hemisphere is positioned at tilt angle $\alpha = 52°$, the stagnation point moves further towards the downwind side near the leading edge at $\theta \approx 47°$ as a result of model tilting. It is obvious that the boundary layer separation and the starting of the wake region occur earlier on the trailing edge in comparison to $\alpha = 30°$, and the flow separations in this configuration falls between $\theta \approx 157°$ and 146° in accordance to minimum and maximum *Re* values as shown in Figure 69 (a) and (e), respectively. Accordingly, it is observed that the velocity magnitude gradient from stagnation point to the trailing edge is lower in comparison to that in $\alpha = 0°$, $\alpha = 30°$, wherein the heat transfer rate has decreased in accordance to the reduction in the flow momentum. However, the value of velocity magnitude at the leading edge has

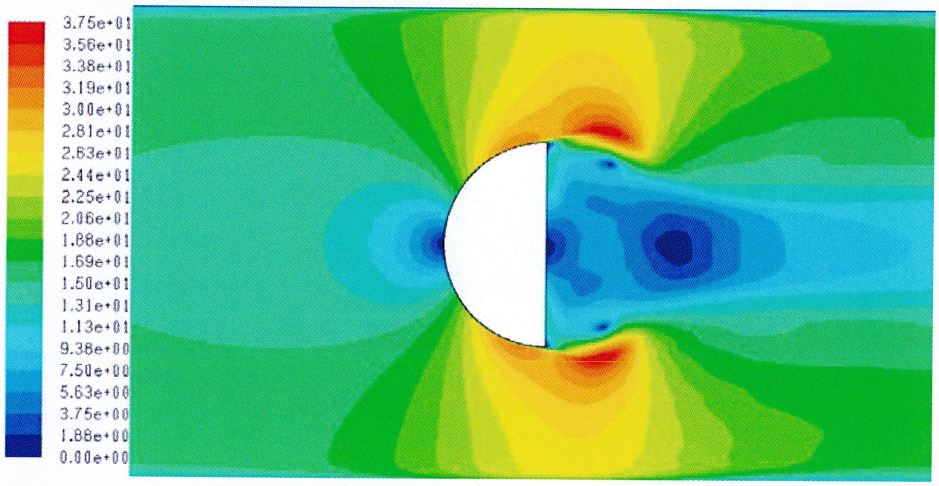
increased by a maximum of 1.94 % compared to that at $\alpha = 30°$, as reported at the high $Re = 2.5\times10^5$. It is also noticed that, the wake region behind hemisphere extended further and a strong flow recirculation and vortices are explicit for this configuration. Consequently, larger heat dissipation is reported at the lower half portion of back surface of the hemisphere due to high velocity magnitude as highlighted earlier, in section 4.2.4.



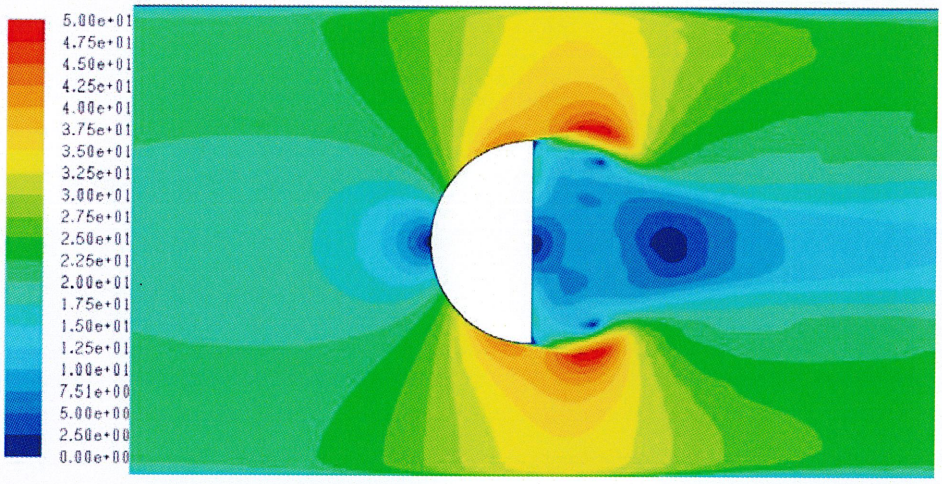
(a) $Re = 0.5 \times 10^5$



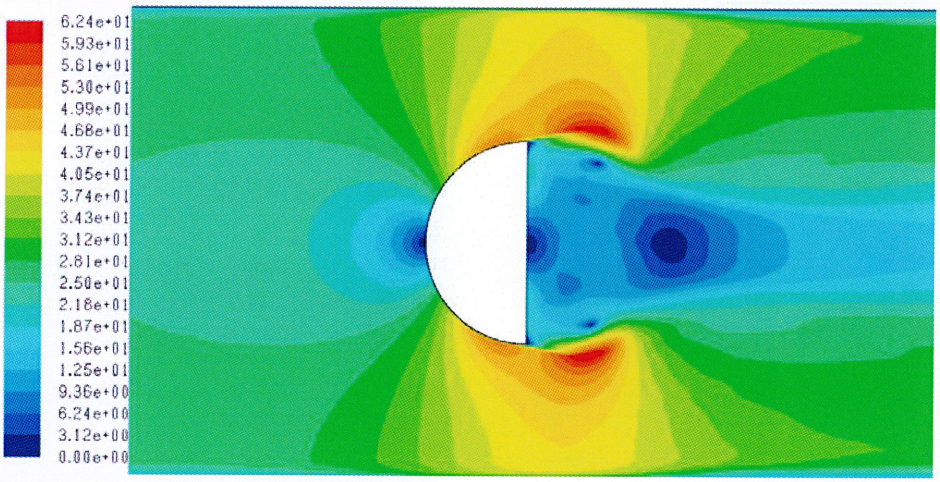
(b) $Re = 1.0 \times 10^5$



(c) $Re = 1.5 \times 10^5$

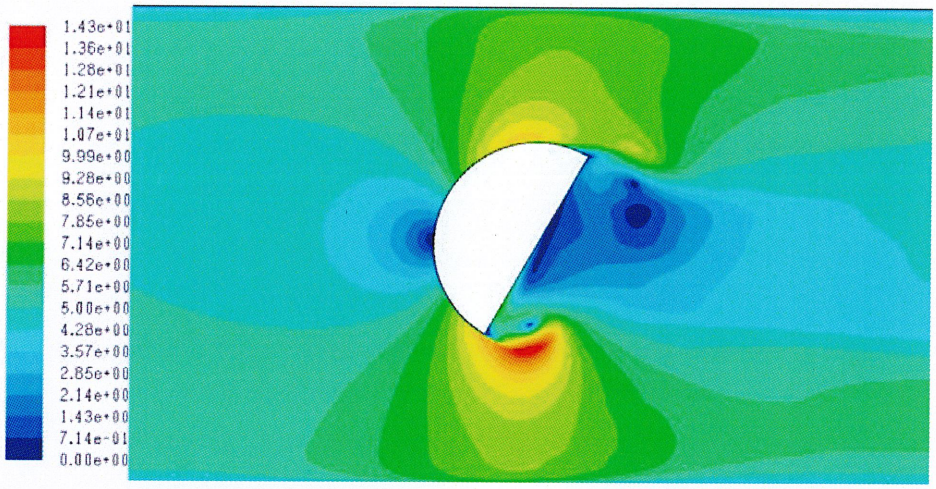


(d) $Re = 2.0 \times 10^5$

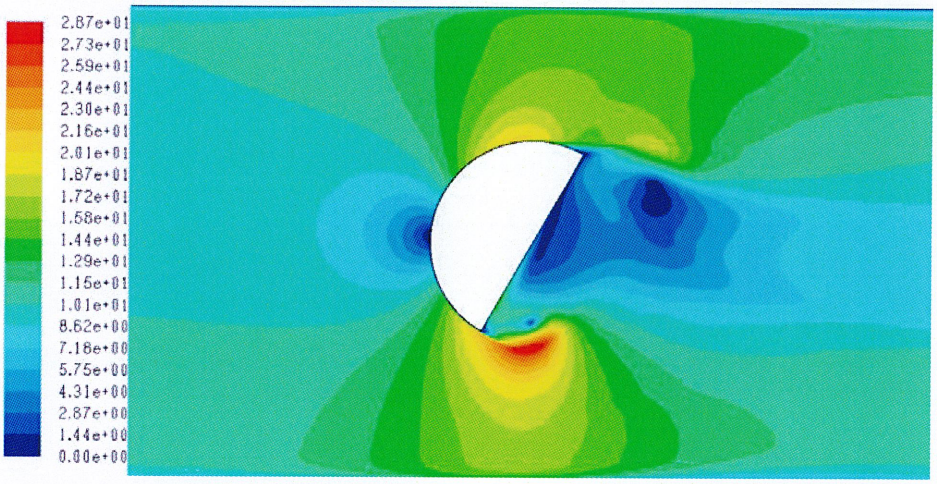


(e) $Re = 2.5 \times 10^5$

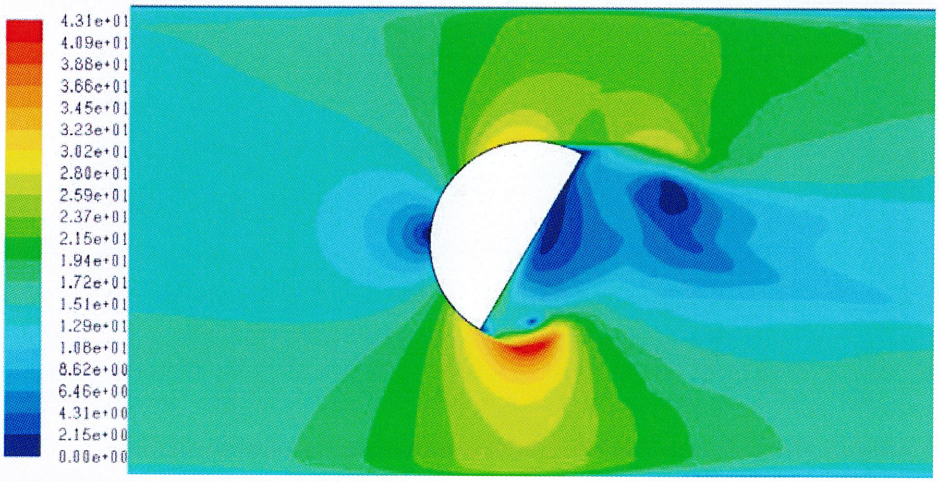
Figure 67: Velocity magnitude contours plot at various Reynolds number (a-e) for hemisphere positioned at $\alpha = 0°$ tilt angle



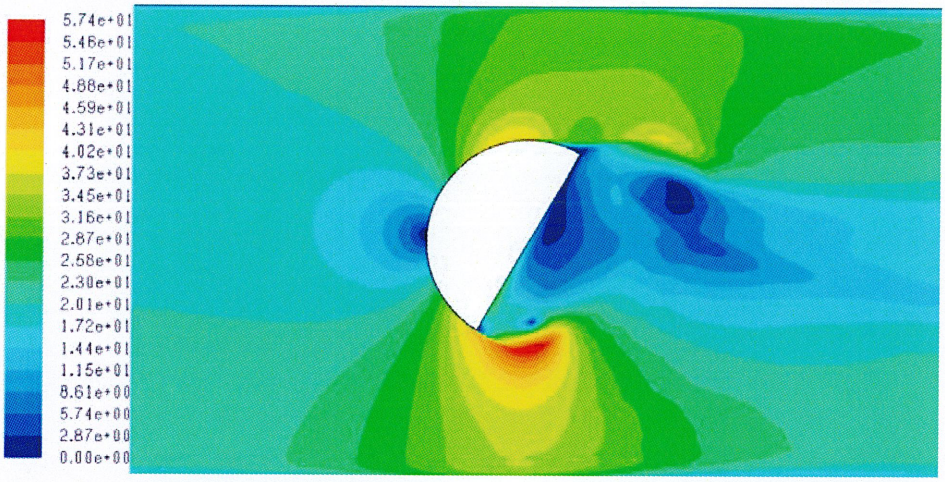
(a) $Re = 0.5 \times 10^5$



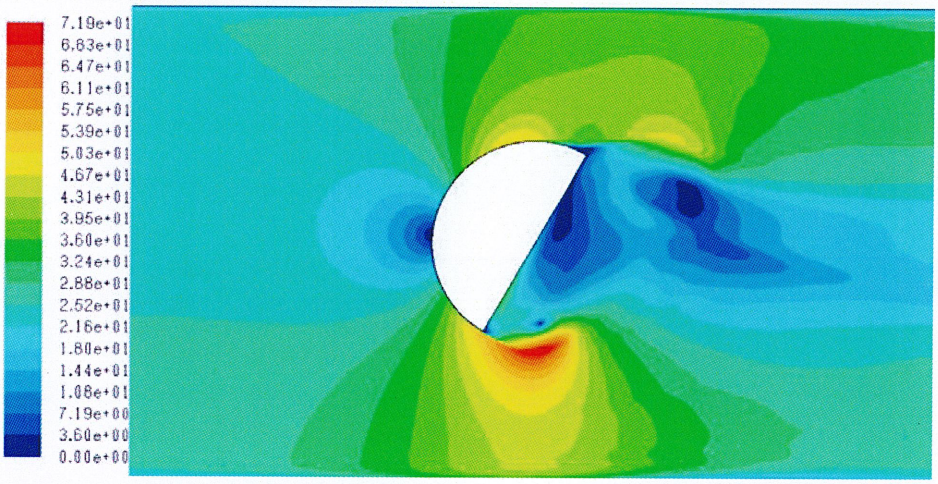
(b) $Re = 1.0 \times 10^5$



(c) $Re = 1.5 \times 10^5$

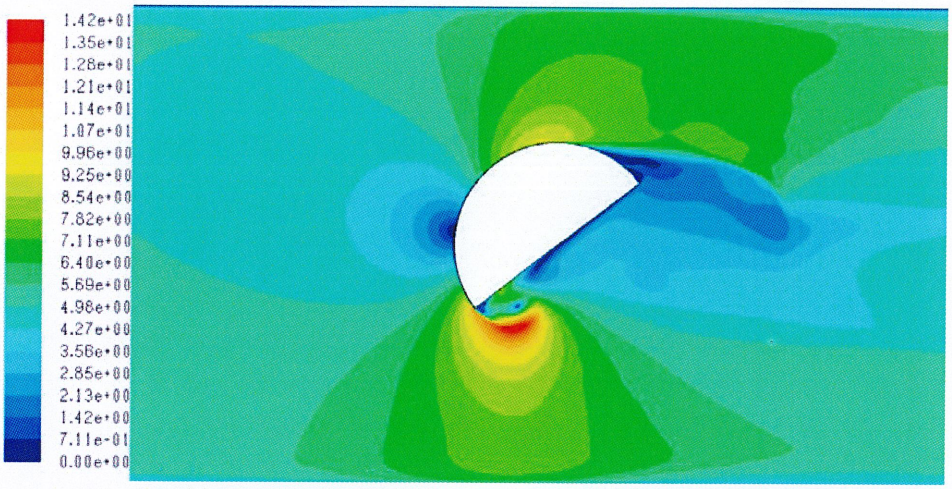


(d) $Re = 2.0 \times 10^5$

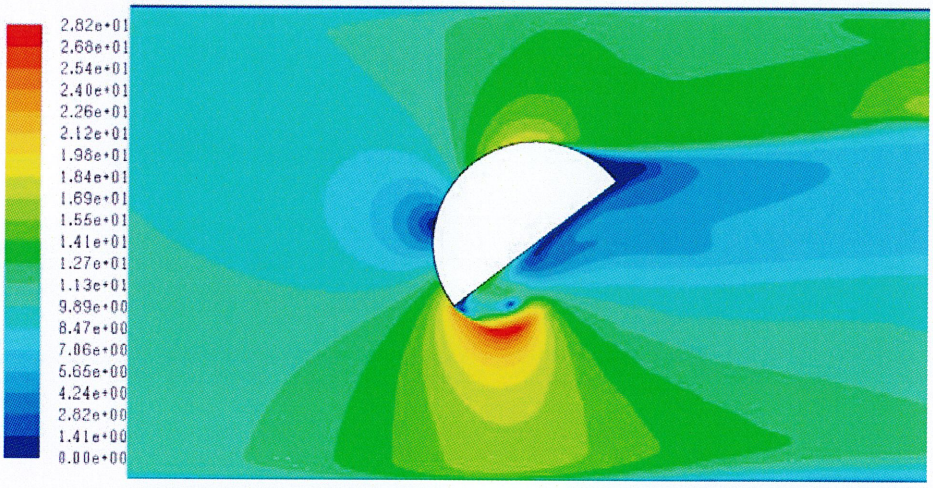


(e) $Re = 2.5 \times 10^5$

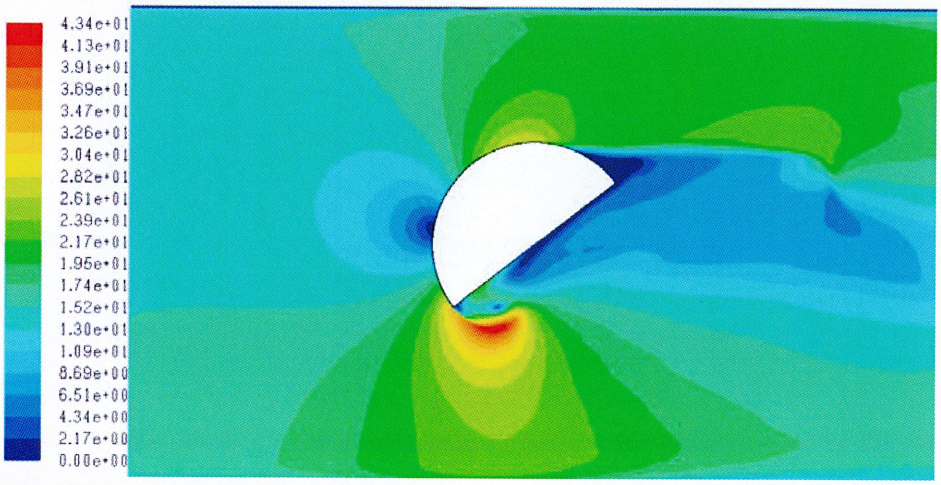
Figure 68: Velocity magnitude contours plot at various Reynolds number (a-e) for hemisphere positioned at $\alpha = 30°$ tilt angle



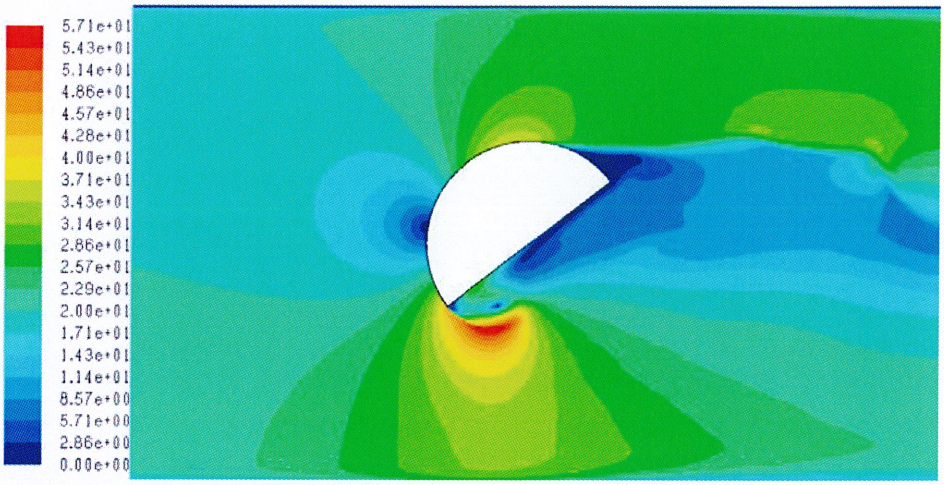
(a) $Re = 0.5\times10^5$



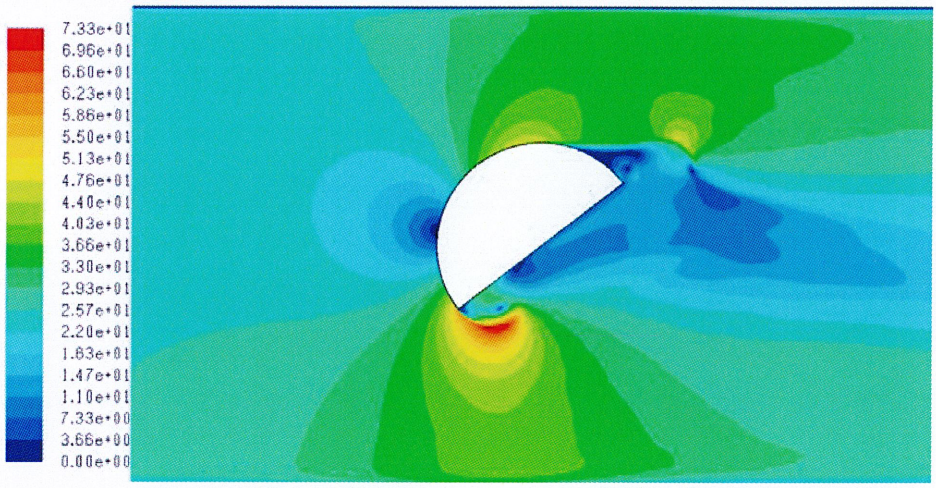
(b) $Re = 1.0\times10^5$



(c) $Re = 1.5\times10^5$



(d) $Re = 2.0\times10^5$



(e) $Re = 2.5\times10^5$

Figure 69: Velocity magnitude contours plot at various Reynolds number (a-e) for hemisphere positioned at $\alpha = 52°$ tilt angle

4.2.6 Validation of Numerical Results

The simulation work on the hemisphere front surface is validated with three correlations of average Nusselt number, specifically, the analytical works carried out by (Ahmed & Yovanovich, 1994), (Drake & Backer, 1952) and (Achenbach, 1978), where they developed analytical correlations for general model of forced convection heat transfer from isothermal sphere under specific range of Reynolds number and using fluid with Prandtl number less than unity (Pr < 1). The present results for heat transfer of the front surface of hemispherical model is compared to the results for sphere, since in the spherical bodies the overall heat transfer is identical due to symmetry for both isothermal and isoflux boundary conditions. The graphical representation of actual numerical average Nusselt number, $\overline{Nu}_f$ results obtained at ($\alpha = 0°$) are shown in Figure 70. The simulation work shows good improvement on heat transfer enhancement over (Ahmed & Yovanovich, 1994), (Drake & Backer, 1952) and (Achenbach, 1978). The results shown are within 27 % of (Ahmed & Yovanovich, 1994), 19.36 % with the correlation given by (Drake & Backer, 1952) and a maximum deviation of 12 % is observed from eq. (61) of (Achenbach, 1978). It is observed that at low range of Reynolds number (Re_D based on the hemisphere diameter, D) between $2.0\times10^4 \leq Re_D \leq 4.3\times10^4$, the numerical values of average Nusselt number are in a very good agreement with the three authors. However, at high range of Reynolds number between $6.5\times10^4 \leq Re_D \leq 1.07\times10^5$, the trend of the numerical values deviates from the trends of the correlations. However, the trends of (Achenbach, 1978) are much closer to the present numerical values of average Nusselt number from the front surface of the hemisphere. The aforementioned deviation in numerical results are attributed to several factors, such as, considering the errors involved in

any numerical study and in addition to discretization and round off errors in the simulation, this could be the main reasons of errors. However, this comparison is relatively satisfactory.

(Ahmed & Yovanovich, 1994)

$$Nu_D = 2 + 0.775\, Re_D^{1/2} Pr^{1/2} \qquad (0 \leq Re_D \leq 1.0 \times 10^5) \qquad (59)$$

(Drake & Backer, 1952)

$$Nu_D = 2 + 0.459 Re_D^{0.55} Pr^{0.333} \qquad (0.1 \leq Re_D \leq 2.0 \times 10^5) \qquad (60)$$

(Achenbach, 1978)

$$Nu_D = 2 + (0.25 Re_D + 3 \times 10^{-4} {Re_D}^{1.6})^{1/2} \; (100 \leq Re_D \leq 2.0 \times 10^5) \qquad (61)$$

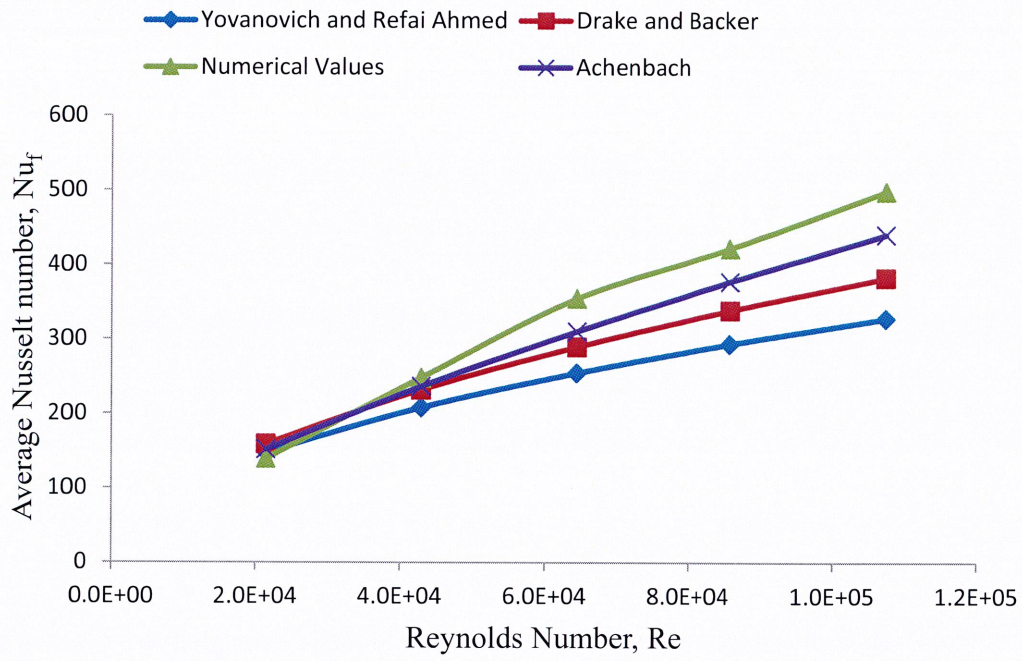


Figure 70: Numerical average Nusselt number over front surface compared with (Drake & Backer, 1952), (Ahmed & Yovanovich, 1994) and (Achenbach, 1978) for different Reynolds number at hemisphere tilt angle $\alpha = 0°$

4.2.7 Comparison of Numerical and Experimental Average Nusselt Number

The experimental results of total average Nusselt number are compared with the numerical results obtained over the hemisphere at three different angles of attack. As can be observed in Figure 71 for hemisphere tilt angles α = 0°, 30° and 52°, respectively, that there is moderate deviation between experimental and numerical results specifically at low range of Reynolds number, however at high range of *Re* the variation becomes insignificant and the values are considerably match. In the tilt angle α = 0°, the difference found to be at it is lowest value of ≈ 0.83 % at high *Re* = 2.5×10^5, while the higher difference was found ≈ 41% at low *Re* = 0.5×10^5. As the tilt angle increase to α = 30°, the experimental value of $\overline{Nu}_{Total}$ is a little bit increased in comparison to the numerical value by approximately ≈ 5.4% at high range of *Re,* and at low Reynolds number namely at *Re* = 0.5×10^5 the deviation found at it is maximum value around ≈ 50 %. At high tilt angle wherein as α = 52°, it is observed that the numerical values of $\overline{Nu}_{Total}$ at higher *Re* increased by around ≈ 7.9 % over the experimental value, and the maximum variation at low *Re* is found approximately ≈ 52 %.

The divergence found between numerical and experimental $\overline{Nu}_{Total}$ values could be perhaps attributed to several factors such as the propagation error associated with the experimental work in addition to the human errors. Moreover, the present calculation of experimental $\overline{Nu}_{Total}$ is based on an estimation that there is a 15% losses from the total heat input obtained from the power supply (as performed in Appendix-C), while in actual condition, it is possibly greater than what we estimate since the increase in the percentage losses of heat input reduces the

experimental value of $\overline{Nu}_{Total}$, although it is difficult to estimate exact value for the heat input losses. Therefore it is not surprising to have a deviation between numerical and experimental works; in general based on the previous estimation this comparison is quite satisfactory.

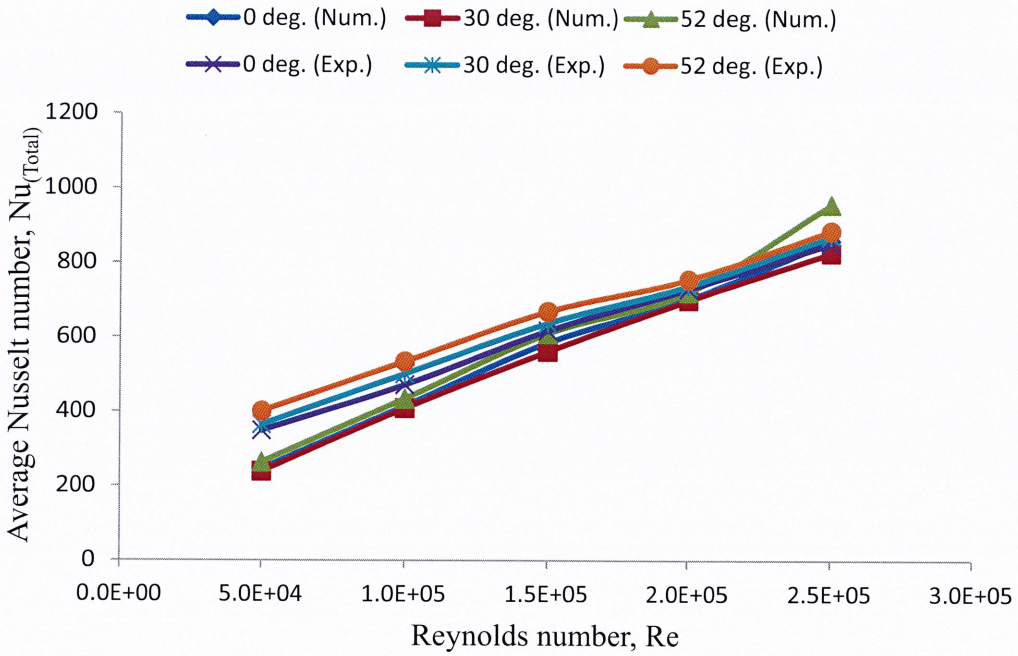


Figure 71: Comparison between numerical and experimental total average Nusselt number over hemisphere (front and back) for different Reynolds number at hemisphere tilt angle $\alpha = 0°$, $\alpha = 30°$ and $\alpha = 52°$

Chapter 5

Conclusions and Recommendations

5.1 Conclusions
5.2 Recommendations
5.3 Publication

CHAPTER 5: CONCLUSIONS AND RECOMMENDATIONS

5.1 Conclusions

An investigation of the fluid flow structures and forced convection heat transfer phenomena for a hemisphere supplied with a constant heat flux positioned at three different tilt angles immersed in air flow in a subsonic wind tunnel are determined using experimental and numerical schemes. The results presented are calculated for Reynolds number range $0.5\times10^5 \leq Re \leq 2.5\times10^5$, increased with an increment of 0.5×10^5. A review of some of the literature published on research conducted for a hemisphere and sphere models in the field of fluid flow and heat transfer was accomplished. A detailed validation analysis against previously published correlations for average Nusselt number was performed and the comparison shows good agreement with the present results of average Nusselt number.

1. Experiments were conducted on an aluminium hemisphere that has a hollow body and it was covered by a circular disc with the same material and thickness. The hemisphere diameter and wall thickness tested were 65 mm and 2 mm, respectively. The method of heat application employed in the heat transfer experiments was by means of a resistance heater element connected with power supply to provide a constant heat flux condition.
2. The experimental results for drag coefficient have shown dependency on the hemisphere inclination in which the larger values of C_D were observed at $\alpha = 52°$, as a result of an early

boundary layer separation. The drag coefficient becomes Reynolds number independent above $Re = 1.5\times10^5$ for cold condition, whereas in the hot condition the values of C_D becomes invariant at $Re = 2.0\times10^5$ and above credited to larger boundary layer thickness. For the values of lift coefficient, C_L in cold condition, it has been shown that C_L values are mainly dependent on the hemisphere inclination α. As α increase the pressure distribution between upper and lower surface becomes asymmetric due to an early boundary layer separation over upper half surface which caused C_L to increase.

3. The experimental results of wake pressure have shown dependency on Reynolds number above 1.5×10^5 for all the three cases, and the variations were insignificant below this *Re*. It is observed that beyond 123.61 mm from the leading edge of the back surface, the wake region has diminished and free stream conditions exist when the hemisphere was tilted at $\alpha = 52°$.
4. The numerical investigation has shown that maximum positive value of pressure coefficient, *Cp* was observed at the stagnation points, $\theta = 90°$, $\theta \approx 63.8°$ and $\theta \approx 47°$, corresponding to hemisphere tilt angle $\alpha = 0°$, $\alpha = 30°$ and $\alpha = 52°$, respectively. The minimum values at the point of boundary layer separations, $\theta = 167.3°$ and $\theta = 146.8°$ were reported at high $Re = 2.5\times10^5$ for $\alpha = 30°$ and $\alpha = 52°$, respectively.
5. The simulation has shown that the transition of separation flow occurs on the trailing surface of the hemisphere where the drag is minimum.
6. The experimental study and numerical simulation have shown that the heat transfer rate is large on the front leading surface of

the hemisphere. This occurred as a result of large local velocity magnitude, attributed to absence of boundary layer separation over the surface which generates a thin boundary layer and thus more effective cooling on this zone. However on the trailing surface, the overall heat transfer is lower due to low velocity magnitude and the commencement of the separation zone, namely for configurations, $\alpha = 30°$ and $\alpha = 52°$. Similar behavior on heat transfer rate has also been noted on the back surface of the hemisphere.

7. The numerical simulation has shown that the minimum value of heat transfer is observed in the separation zone on the front stream-wise direction near the trailing edge. The separation zone comprised of different minima and maxima peaks of heat transfer as a result of flow separation, recirculation and unsteady flow conditions.

8. The tilted hemisphere configurations under study have shown that the front and back surfaces are effective in heat transfer enhancement and they can complement each other. The larger heat transfer dissipation from front surface was found at an angle of attack $\alpha = 0°$, due to the absence of boundary layer separation on the front surface, and it is decreased as α increased, due to an early commence of the wake region. In contrast, an effective heat transfer enhancement at the back surface was observed at larger tilt angle $\alpha = 52°$.

9. The comparison study was done between obtained experimental and numerical total average Nusselt number over entire surfaces of the hemisphere (front and back) and the comparison results show good agreement namely at higher range of Reynolds number. The major finding from both investigations have shown

that the overall large heat transfer dissipation for front and back surfaces was observed at higher tilt angle $\alpha = 52°$, where its increased by around (5% ~ 9%) in comparison to that in $\alpha = 30°$, and by (6% ~ 8.3%) to that in $\alpha = 0°$.

10. Consequently, depends upon which application that the hemisphere will be utilized for, if only front surface will be subjected to a certain flow for cooling purposes its recommended to employ the tilt angle $\alpha = 0°$. However, when it is intended to use the overall model surfaces for heat dissipation, we suggest choosing the configuration of $\alpha = 52°$.

5.2 Recommendations

It is suggested that the temperature be measured at more locations i.e. by installing more thermocouple tapping points over stream-wise and span-wise directions in order to obtain better trends of heat dissipation from the hemisphere front surface, thereby the separation and stagnation points can by examined precisely. In addition, it is recommended to reduce the blockage ratio in the tunnel by reducing the hemisphere diameter to optimum size in order to reduce the possibility of interference of the upper and bottom walls of the tunnel working section during experimental and numerical investigations. Furthermore, the effective heat transfer on the hemisphere surface can be optimized by studying flow at more different inclinations and the results can be compared afterwards. Also, different materials and surface finish can be investigated to optimize the preferable hemispherical surface in terms of heat dissipation.

5.3 Publication

The work was partly published in the Journal of International Science and Technology Conference (ISTEC), for hemisphere tilt angle $\alpha = 52°$ as shown in appendix (D).

LIST OF REFERENCES

Achenbach, E. (1972). Experiments on the Flow Past Spheres at Very High Reynolds Numbers. *Journal of Fluid Mechanics , (54),(3)*, 565-575.

Achenbach, E. (1978). Heat Transfer From Spheres up to Re = 6 x 10^6. In Proc. *6th International Heat Transfer Conference , (5)*, 341-346.

Ahmed, G. R., & Yovanovich, M. M. (1994). Approximate Analytical Solution of Forced Convection Heat Transfer from Isothermal Spheres for all Prandtl Numbers. *ASME Journal of Heat Transfer , (116)*, 838-843.

Ahmed, G. R., & Yovanovich, M. M. (1970). Experimental Study of Forced Convection from Isothermal Circular and Square Cylinders and Toroids. *ASME Journal of Heat Transfer , (119)*, 70-79.

Beckwith, T. G., Marangoni, R. D., & Lien, J. H. (2007). Mechanical Measurments (6th Edition ed.). NJ: Pearson Prentice Hall.

Beg, S. A. (1975). Forced Covection Mass Transfer Studies from Spheroids. *Warme- und Stoffubertragung , (8)*, 127-135.

Castro, I. P., & Fackrell, J. E. (1978). A Note on Two-Dimensional Fence Flows, With Emphasis on Wall Constraint. *Journal of Wind Engineering and Industrial Aerodynamics , (3)*, 21-38.

Cheng, C. M., & Fu, C. L. (2010). Characteristic of Wind Loads on a Hemispherical Dome in Smooth Flow and Turbulent Boundary Layer Flow. *Journl of Wind Engineering and Industrial Aerodynamics , (98)*, 328-344.

Dhole, S. D., Chhabra, R. P., & Eswaran, V. (2006). A Numerical Study on the Forced Convection Heat Transfer From an Isothermal and Isoflux Sphere in the Steady Symmetric Flow Regime. *International Journal of Heat and Mass Transfer , (49)*, 984-994.

Drake, R. M., & Backer, G. H. (1952). Heat Transfer from Spheres to a Rarefied Gas in Supersonic Flow. *Trans. ASME , (74)*, 1241-1249.

Fluent, I. (2006). Standard RNG and Realizable k-ε Models Theory. *Fluent User Guide Manual.* Retrieved from www.ansys.com/.

Good, M. C., & Joubert, P. N. (1968). The Form Drag of Two Dimensional Bluff-Plates Immersed in a Turbulent Boundary Layer. *Journal of Fluid Mechanics , (3)*, 547-582.

Incropera, F. P., & DeWitt, D. P. (2002). Fundamentals of Heat and Mass Transfer (5th Edition ed.). Hoboken: John Wiley & Sons.

Kendoush, A. A. (1995). Low Prandtl Number Heat Transfer to Fluids Flowing Past an Isothermal Spherical Particle. *International Journal of Heat and Fluid Flow , (16)*, 291-297.

Lewandowski, W. M., Kubski, P., & Khubeiz, J. M. (1992). Laminar Free Convection Heat Transfer from an Isothermal Hemisphere. *Recent Advances in Heat Transfer , (2)*, 606-620.

Lewandowski, W. M., Kubski, P., Khubeiz, J. M., Bieszk, H., Wilczewski, T., & Szymanski, S. (1996). Theoretical and Experimental Study of Natural Convection Heat Transfer from Isothermal Hemisphere. *International Journal of Heat and Mass Transfer , (40)*, 101-109.

Maher, F. J. (1965). Wind Loads on Basic Dome Shapes. *Journal of the Structural Division , (91), ASCE No. ST3*, 199-213.

Manhart, T. (1998). Vortex Shedding from a Hemisphere in a Turbulent Boundary Layer. *Journal of Theoretical and Computational Fluid Dynamics , (12)*, 1-28.

Meroney, R. N., Letchford, C. W., & Sarkar, P. P. (2002). Comparison of Numerical and Wind Tunnel Simulation of Wind Loads on Smooth, Rough and Dual Domes Immersed in a Boundary Layer. *Journal of Wind and Structures , (5)*, 347-358.

Ogawa, T., Nakayama, M., Murayama, S., & Sasaki, Y. (1991). Characteristics of Wind Pressures on Basic Structures with Curved Surfaces and their Responce in Turbulent Boundary Flow. *Journal of Wind Engineering and Industrial Aerdynamics , (38)*, 427-438.

Range Raju, K. G., Loeser, J., & Plate, E. J. (1976). Velocity Profiles and Force Drag for Turbulent Boundary Layer along Smooth and Rough Flat Plates. *Journal of Fluid Mechanics , (76)*, 383-399.

Richter, A., & Nikrityuk, P. A. (2011). Drag Forces and Heat Transfer Coefficients for Spherical, Cuboidal and Ellipsoidal Particles in Cross Flow at Sub-critical Reynolds Number. *International Journalof Heat and Mass Transfer , (55)*, 1343-1354.

Sakamoto, H., Moriya, M., & Arie, M. (1975). A Study on the Flow around Bluff Bodies Immersed in Turbulent Boundary Layers: Part 1, On the Form Drag of the Normal Plates. *Bulletin of the Japan Society of Mechanical Engineers , (18)*, 1126-1133.

Sakamoto, H., Moriya, M., & Arie, M. (1977). A Study on the Flow around Bluff Bodies Immersed in Turbulent Boundary Layers: Part 2, On the Pressure Forces of Inclined Plates. *Bulletin of the Japan Society of Mechanical Engineers , (20)*, 71-78.

Sakamoto, H., Moriya, M., & Arie, M. (1977). A Study on the Flow around Bluff Bodies Immersed in Turbulent Boundary Layers: Part 3. *Transactions of the Japan Society of Mechanical Engineers , (42)*, 3224-3232.

Savory, E., & Toy, N. (1986). Hemisphere and Hemisphere Cylinders in Turbulent Boundary Layers. *Journal of Wind Engineering and Industrial Aerodynamics , (23)*, 345-364.

Savory, E., & Toy, N. (1986). The Flow Regime in the Turbulent Near Wake of a Hemisphere. *Journal of Experiments in Fluids , (4)*, 181-188.

Savory, E., & Toy, N. (1988). The Separated Shear Layers Associated with Hemispherical Bodies in Turbulent Boundary Layers. *Journal of Wind Engineering and Industrial Aerodynamics , (28)*, 291-300.

Tamura, T., Kuwahara, K., & Suzuki, M. (1990). Numerical Study of Wind Pressures on a Domed Roof and Near Wake Flows. *Journal of Wind Engineering and Industrial Aerodynamics , (36)*, 1001-1010.

Tavakol, M. M., & Yaghoubi, M. (2010). Experimental and Numerical Analysis of Turbulent Air Flow around a Surface Mounted Hemisphere. *Transaction B: Mechanical Engineering , (17)*, 480-491.

Tavakol, M. M., Yaghoubi, M., & Motlagh, M. M. (2010). Air Flow Aerodynamic on a Wall Mounted Hemisphere for Various Turbulent Boundary Layers. *Journal of Experimental Thermal and Fluid Science , (34)*, 538-553.

Taylor, T. J. (1991). Wind Pressures on a Hemispherical Dome. *Journal of Wind Engineering and Industrial Aerodnynamics , (40)*, 199-213.

Toy, N., Moss, W. D., & Savory, E. (1983). Wind Tunnel Studies on a Dome in Turbulent Boundary Layers. *Journal of Wind Engineering and Industrial Aerdynamics , (11)*, 201-212.

Wedkind, G. L., & Kobus, C. J. (1996). Predicting the Average Heat Transfer Coefficient for an Isothermal Vertical Circular Disc with Assisting and Opposing Combined Forced and Natural Convection. *International Journal of Heat and Mass Transfer , (13)*, 2843-2845.

Whitaker, S. (1972). Forced Convection Heat Transfer Correlations for Flow in Pipes, Past Flat Plates, Single Cylinders, Single Spheres, and Flow Packed Beds and Tube Bundles. *Journal of American Institute of Chemical Engineers , (18)*, 361-371.

White, F. M. (2003). Fluid Mechanics (5th Edition ed.). New York: McGraw-Hill.

Youvanovich, M. M., & Vanoverbeke, C. A. (1988). Combined Natural and Forced Convection Heat Transfer from Isothermal Spheres. *AIAA, Thermophysics, Plasmadynamics and Lasers Conference, San Antonio, TX, , Paper No. (88)-2618*.

APPENDICES

APPENDIX (A): UNCERTAINTY ANALYSIS

APPENDIX (B): CONVERSION FROM LINEAR LOCATION TO ANGULAR LOCATION FOR STREAM-WISE SURFACE

APPENDIX (C): HEAT TRANSFER LOSSES CALCULATIONS THROUGH THE HEMISPHERICAL MODEL

APPENDIX (D): PUBLICATION PAPER IN THE JOURNAL OF INTERNATIONAL SCIENCE AND TECHNOLOGY CONFERENCE (ISTEC)

APPENDIX (A): UNCERTAINTY ANALYSIS

A.1 Uncertainty Associated with the Measurements of Local Temperatures over Hemisphere Surfaces

Type K thermocouples were used in this research to measure the temperatures difference over hemisphere front and back surfaces. The thermocouples were connected to a data acquisition system. Calibration was performed to the thermocouples, in which the readings from the data acquisition system were calibrated against the reading obtained from thermometer temperature scale installed in the Laboratory. A value of ± 0.1°C was estimated as precision uncertainty (A) for the thermometer scale, and the bias uncertainty (B) given for thermocouple type K is ± 1.5°C. Therefore the total uncertainty for the temperature measurement was calculated as follows;

$$U_T = \sqrt{B^2 + A^2} = \sqrt{(1.5)^2 + (0.1)^2} = \pm 1.503°C$$

A.2 Uncertainty Associated with the Hemisphere Projected Frontal Area

The hemisphere projected frontal area is used for the measurement of the drag and lift coefficients, and it is calculated as

$$A = \frac{\pi}{4} D^2 \qquad (\boldsymbol{A.1})$$

The uncertainty in A was calculated as follows

$$U_A = \sqrt{\left(\frac{\partial A}{\partial D} U_D\right)^2}$$

Where;

$$\frac{\partial A}{\partial D} = \frac{\pi}{2} D, \qquad and\ U_D = \pm 0.5\ mm$$

Thus, $U_A = \pm\, 5.1 \times 10^{-5}\ m^2$.

The total uncertainty in the hemisphere surface area is

$$\frac{U_A}{A} \times 100 = \pm\, 1.56\ \%$$

A.3 Uncertainty Associated with the static pressure at the inlet of working section and wake pressure behind hemisphere

The static pressure, P_s was measured using static pressure sensor installed at the inlet of working section wall, whiles the wake pressure, P_{wake} was measured by means of wake survey rake installed at the wake region behind hemisphere and pointed towards hemisphere back surface. The obtained differential heads, Δh were then converted to pressure measurement as follow;

$$\Delta P_{wake} = \Delta P_s = \rho_w . g . \Delta h \qquad (\boldsymbol{A.2})$$

The uncertainty in P_s and P_w were calculated as follows

$$U_{P_s} = \sqrt{\left(\frac{\partial P_s}{\partial \Delta h} U_{\Delta h}\right)^2}$$

$$U_{P_w} = \sqrt{\left(\frac{\partial P_{wake}}{\partial \Delta h} U_{\Delta h}\right)^2}$$

Where

$$\frac{\partial P_s}{\partial \Delta h} = \rho_w . g, \qquad and\ U_{\Delta h} = \pm 0.1\ mm, and$$

$$\frac{\partial P_{wake}}{\partial \Delta h} = \rho_w . g, \qquad and\ U_{\Delta h} = \pm 0.1\ mm$$

Thus, $U_{P_{wake}} = U_{P_s} = \pm\ 0.981\ Pa.$

The total uncertainty in the static and wake pressure are

$$\frac{U_{P_s}}{P_s} \times 100 = \pm\ 0.261\ \%$$

$$\frac{U_{P_{wake}}}{P_{wake}} \times 100 = \pm\ 0.289\ \%$$

A.4 Uncertainty Associated with the Density of Air

The density of air was evaluated at the inlet of wind tunnel working section based on air inlet temperature and static pressure, and it is used for calculating the air velocity at the inlet. In order to, calculate Reynolds number in the tunnel. The ideal gas relation was used to determine, the density as follows;

$$\rho = \frac{P_{abs}}{RT_\infty} \qquad (\boldsymbol{A.3})$$

For tunnel inlet condition where, $T_\infty = 20.5$ °C and static pressure $P_s = 374.74\ Pa$, and the absolute pressure, $P_{abs} = 100.95\ KPa$. The uncertainty in ρ was calculated as follows;

$$U_\rho = \sqrt{\left(\frac{\partial \rho}{\partial P_{abs}} U_{P_{abs}}\right)^2 + \left(\frac{\partial \rho}{\partial T_\infty} U_{T_\infty}\right)^2}$$

Where

$$\frac{\partial \rho}{\partial P_{abs}} = \frac{1}{RT_\infty}, and\ U_{P_{abs}} = \pm 8.221\ Pa, and$$

$$\frac{\partial \rho}{\partial T_\infty} = -\frac{P_{abs}}{RT_\infty{}^2}, and\ U_{T_\infty} = \pm 0.1\ °C$$

Thus, $U_\rho = \pm 4.2 \times 10^{-4}\ kg/m^3$.

Therefore the total uncertainty in the calculated air density is

$$\frac{U_\rho}{\rho} \times 100 = \pm 0.035\ \%$$

A.5 Uncertainty Associated with the Air Flow Velocity at the Inlet of Working Section

The free stream air flow velocity at the inlet of working section is related to the static pressure inside the working section by the following relation that based on air inlet density. The velocity was defined as

$$V_\infty = \sqrt{\frac{2\Delta P_s}{\rho}} \qquad (\boldsymbol{A.4})$$

For $\rho = 1.202\ kg/m^3$, $P_s = 374.74\ Pa$, the uncertainty in V_∞ was calculated as

$$U_{V_\infty} = \sqrt{\left(\frac{\partial V_\infty}{\partial P_s} U_{P_s}\right)^2 + \left(\frac{\partial V_\infty}{\partial \rho} U_\rho\right)^2}$$

Where

$$\frac{\partial V_\infty}{\partial P_s} = \frac{1}{\sqrt{2\ P_s \rho}}, \qquad and\ U_{P_s} = \pm 0.981\ Pa, and$$

$$\frac{\partial V_\infty}{\partial \rho} = -\sqrt{\frac{P_s}{2\rho^3}}, \qquad and\ U_\rho = \pm 4.2 \times 10^{-4} kg/m^3$$

Thus, $U_{V_\infty} = \pm 0.033\ m/s$.

The total uncertainty in the inlet velocity, for instance at $V_\infty = 25$ m/s is

$$\frac{U_{V_\infty}}{V_\infty} \times 100 = \pm 0.132\ \%$$

A.6 Uncertainty Associated with the Drag Coefficient of Hemisphere

The drag coefficient at tilt angle zero $\alpha = 0°$ was calculated as follows

$$C_D = \frac{2F_D}{\rho\, V_\infty^2\, A \cos\alpha} \qquad (\boldsymbol{A.5})$$

For $\alpha = 0°$, $\rho = 1.202\ kg/m^3$, and at $V_\infty = 25\ m/s$ the drag force was $F_D = 0.74\ N$, the uncertainty in C_D was calculated as

$$U_{C_D} = \sqrt{\left(\frac{\partial C_D}{\partial F_D} U_{F_D}\right)^2 + \left(\frac{\partial C_D}{\partial \rho} U_\rho\right)^2 + \left(\frac{\partial C_D}{\partial V_\infty} U_{V_\infty}\right)^2 + \left(\frac{\partial C_D}{\partial A} U_A\right)^2}$$

Where

$$\frac{\partial C_D}{\partial F_D} = \frac{2}{\rho V_\infty^2 A \cos\alpha}, \qquad and\ U_{F_D} = \pm 0.005\ N,$$

$$\frac{\partial C_D}{\partial \rho} = -\frac{2F_D}{\rho^2 V_\infty^2 A \cos\alpha}, \qquad and\ U_\rho = \pm 4.2 \times 10^{-4}\ kg/m^3,$$

$$\frac{\partial C_D}{\partial V_\infty} = -\frac{4F_D}{\rho V_\infty^3 A \cos\alpha}, \qquad and\ U_{V_\infty} = \pm 0.033\ m/s, and$$

$$\frac{\partial C_D}{\partial A} = -\frac{2F_D}{\rho V_\infty^2 A^2 \cos\alpha}, \qquad and\ U_A = \pm 5.1 \times 10^{-5}\ m^2$$

Thus, $U_{C_D} = \pm 0.01$

The total uncertainty in the drag coefficient, for instance at $V_\infty = 25$ m/s is

$$\frac{U_{C_D}}{C_D} \times 100 = \pm 1.7\ \%$$

A.7 Uncertainty Associated with the Lift Coefficient of Hemisphere

The Lift coefficient at tilt angle zero $\alpha = 0°$ was calculated as follows

$$C_L = \frac{2F_L}{\rho\, V_\infty^2\, A \cos\alpha} \qquad (\boldsymbol{A.6})$$

For $\alpha = 0°$, $\rho = 1.202\ kg/m^3$, and at $V_\infty = 25\ m/s$ the drag force was $F_L = -0.03\ N$, the uncertainty in C_L was calculated as

$$U_{C_L} = \sqrt{\left(\frac{\partial C_L}{\partial F_L} U_{F_L}\right)^2 + \left(\frac{\partial C_L}{\partial \rho} U_\rho\right)^2 + \left(\frac{\partial C_L}{\partial V_\infty} U_{V_\infty}\right)^2 + \left(\frac{\partial C_L}{\partial A} U_A\right)^2}$$

Where

$$\frac{\partial C_L}{\partial F_L} = \frac{2}{\rho V_\infty^2 A \cos\alpha}, \qquad and\ U_{F_L} = \pm\, 0.005\ N,$$

$$\frac{\partial C_L}{\partial \rho} = -\frac{2F_L}{\rho^2 V_\infty^2 A \cos\alpha}, \qquad and\ U_\rho = \pm\, 4.2 \times 10^{-4}\ kg/m^3,$$

$$\frac{\partial C_L}{\partial V_\infty} = -\frac{4F_L}{\rho V_\infty^3 A \cos\alpha}, \qquad and\ U_{V_\infty} = \pm\, 0.033\ m/s, and$$

$$\frac{\partial C_L}{\partial A} = -\frac{2F_L}{\rho V_\infty^2 A^2 \cos\alpha}, \qquad and\ U_A = \pm\, 5.1 \times 10^{-5}\ m^2$$

Thus, $U_{C_L} = \pm\, 4.03 \times 10^{-3}$

The total uncertainty in the lift coefficient, for instance at $V_\infty = 25$ m/s is

$$\frac{U_{C_L}}{C_L} \times 100 = \pm\, 16.73\ \%$$

A.8 Uncertainty Associated with the Air Flow Reynolds Number

The air flow Reynolds number was calculated as follow

$$Re_D = \frac{\rho V_\infty D}{\mu} \qquad (A.7)$$

For $\rho = 1.202\ kg/m^3$, $V_\infty = 25\ m/s$, $\mu = 1.82 \times 10^{-5}\ kg/m.s$ and $Re_D = 107321$, the uncertainty in Re_D was calculated as follows

$$U_{Re_D} = \sqrt{\left(\frac{\partial Re_D}{\partial \rho} U_\rho\right)^2 + \left(\frac{\partial Re_D}{\partial V_\infty} U_{V_\infty}\right)^2 + \left(\frac{\partial Re_D}{\partial D} U_D\right)^2 + \left(\frac{\partial Re_D}{\partial \mu} U_\mu\right)^2}$$

Where

$$\frac{\partial Re_D}{\partial \rho} = \frac{V_\infty D}{\mu}, \qquad and\ U_\rho = \pm 4.2 \times 10^{-4}\ kg/m^3,$$

$$\frac{\partial Re_D}{\partial V_\infty} = \frac{\rho D}{\mu}, \qquad and\ U_{V_\infty} = \pm 0.033\ m/s,$$

$$\frac{\partial Re_D}{\partial D} = \frac{\rho V_\infty}{\mu}, \qquad and\ U_D = \pm 0.5\ mm, and$$

$$\frac{\partial Re_D}{\partial \mu} = -\frac{\rho V_\infty D}{\mu^2}, \qquad and\ U_\mu = \pm 4.5 \times 10^{-8}\ kg/m.s$$

Thus, $U_{Re_D} = \pm 879.42$

The total uncertainty in the air flow Reynolds number

$$\frac{U_{Re_D}}{Re_D} \times 100 = \pm 0.82\%$$

A.9 Uncertainty Associated with the Heat Transfer Rate Output from the Hemisphere

The heat transfer rate output from the hemisphere front and back surfaces, q_T is equal to the heater power dissipation, P and it was calculated as follows

$$q_T = P = V \times I \qquad (\boldsymbol{A.8})$$

For the voltage $V \approx 30$ and $I \approx 1.187\ Amps$ and $q_T \approx 35.505\ W$, the uncertainty in q_T was calculated as

$$U_{q_T} = \sqrt{\left(\frac{\partial q_T}{\partial V} U_V\right)^2 + \left(\frac{\partial q_T}{\partial I} U_I\right)^2}$$

Where

$$\frac{\partial q_T}{\partial V} = I, \qquad and\ U_V = \pm 0.05\ V,$$

$$\frac{\partial q_T}{\partial I} = V, \qquad and\ U_I = \pm 0.0065\ Amps,$$

Thus, $U_{q_T} = \pm\ 0.203\ W$

The total uncertainty in the heat transfer rate output, for instance at $V_\infty = 25$ m/s is

$$\frac{U_{q_T}}{q_T} \times 100 = \pm\ 0.57\ \%$$

A.10 Uncertainty Associated with the Total Average Nusselt Number Over Hemisphere Front and Back Surfaces

The total average Nusselt number over the entire hemisphere surfaces was calculated from Eq. (54) Ch.4, as follows

$$\overline{Nu}_{Total} = \frac{D}{kA_T}\left(\frac{q_T}{T_s - T_\infty}\right) \qquad (\boldsymbol{A.9})$$

For $D = 0.065\ m$, $k = 0.02538\ W/m°C$, $A_T = 0.00995\ m^2$, $q_T \approx 35.505\ W$, $T_s = 29.41°C$, $T_\infty = 20.5\ °C$ and $\overline{Nu}_{Total} = 852.2$ at ($\alpha = 0°$ and $V_\infty = 25$ m/s), the uncertainty associated with in $\overline{Nu}_{Total}$ was calculated as

$$U_{\overline{Nu}_T} = \sqrt{\left(\frac{\partial \overline{Nu}_T}{\partial D}U_D\right)^2 + \left(\frac{\partial \overline{Nu}_T}{\partial k}U_k\right)^2 + \left(\frac{\partial \overline{Nu}_T}{\partial A_T}U_{A_T}\right)^2 + \left(\frac{\partial \overline{Nu}_T}{\partial q_T}U_{q_T}\right)^2 + \ldots}$$

$$\ldots \sqrt{\left(\frac{\partial \overline{Nu}_T}{\partial T_s}U_{T_s}\right)^2 + \left(\frac{\partial \overline{Nu}_T}{\partial T_\infty}U_{T_\infty}\right)^2}$$

Where

$$\frac{\partial \overline{Nu}_T}{\partial D} = \frac{1}{kA_T}\left(\frac{q_T}{T_s - T_\infty}\right), \qquad and\ U_D = \pm 0.5\ mm,$$

$$\frac{\partial \overline{Nu}_T}{\partial k} = -\frac{D}{k^2 A_T}\left(\frac{q_T}{T_s - T_\infty}\right), \qquad and\ U_k = \pm 7.5 \times 10^{-5}\ W/m°C,$$

$$\frac{\partial \overline{Nu}_T}{\partial A_T} = -\frac{D}{kA_T^2}\left(\frac{q_T}{T_s - T_\infty}\right), \qquad and\ U_{A_T} = \pm 1.53 \times 10^{-4}\ m^2,$$

$$\frac{\partial \overline{Nu}_T}{\partial q_T} = \frac{D}{kA_T}\left(\frac{1}{T_s - T_\infty}\right), \qquad and\ U_{q_T} = \pm 0.203\ W,$$

$$\frac{\partial \overline{Nu}_T}{\partial T_s} = -\frac{D}{kA_T}\left(\frac{q_T}{(T_s - T_\infty)^2}\right), \qquad and\ U_{T_s} = \pm 1.5°C, and$$

$$\frac{\partial \overline{Nu}_T}{\partial T_\infty} = \frac{D}{kA_T}\left(\frac{q_T}{(T_s - T_\infty)^2}\right), \qquad and\ U_{T_\infty} = \pm 0.1°C,$$

Thus, $U_{\overline{Nu}_T} = \pm 173.9\ W$

The total uncertainty in the total average Nusselt number, for instance at $V_\infty = 25$ m/s is

$$\frac{U_{\overline{Nu}_T}}{\overline{Nu}_T} \times 100 = \pm 20.4\ \%$$

Table A -1: Uncertainty analysis results at an angle of attack, $\alpha = 0°$ for cold condition tests

Angle of attack, $\alpha = 0°$								
V_∞	U_{V_∞}		U_{C_D}		U_{C_L}		U_{Re_D}	
5 m/s	±0.159	0.64 %	±0.1	-	±0.1	-	± 707.2	3.29 %
10 m/s	±0.082	0.32 %	±0.025	25.1 %	±0.025	-	± 493.8	1.15 %
15 m/s	±0.054	0.22 %	±0.014	2.7 %	±0.011	-	± 571.1	0.88 %
20 m/s	± 0.04	0.16 %	±0.011	1.94 %	±0.006	-	± 716.2	0.83 %
25 m/s	±0.033	0.13 %	±0.01	1.68 %	±0.004	16.7 %	± 879.4	0.82 %

Table A -2: Uncertainty analysis results at an angle of attack, $\alpha = 30°$ for cold condition tests

Angle of attack, $\alpha = 30°$								
V_∞	U_{V_∞}		U_{C_D}		U_{C_L}		U_{Re_D}	
5 m/s	±0.159	0.64 %	±0.11	-	± 0.11	-	± 707.2	3.29 %
10 m/s	±0.082	0.32 %	±0.03	12.7%	±0.028	-	± 493.8	1.15 %
15 m/s	±0.054	0.22 %	±0.017	2.54%	±0.012	-	± 571.1	0.88 %
20 m/s	± 0.04	0.16 %	±0.013	1.92 %	±0.0072	25.5%	± 716.2	0.83 %
25 m/s	±0.033	0.13 %	±0.012	1.69%	±0.0046	12.6%	± 879.4	0.82 %

Table A -3: Uncertainty analysis results at an angle of attack, $\alpha = 52°$ for cold condition tests

Angle of attack, $\alpha = 0°$								
V_∞	U_{V_∞}		U_{C_D}		U_{C_L}		U_{Re_D}	
5 m/s	±0.159	0.64 %	±0.16	-	± 0.16	-	± 707.2	3.29 %
10 m/s	±0.082	0.32 %	±0.042	9.33%	± 0.04	54.1%	± 493.8	1.15 %
15 m/s	±0.054	0.22 %	±0.024	2.51%	±0.018	-	± 571.1	0.88 %
20 m/s	± 0.04	0.16 %	±0.018	1.98%	± 0.01	8.91%	± 716.2	0.83 %
25 m/s	±0.033	0.13 %	±0.017	1.7%	±0.007	4.18%	± 879.4	0.82 %

Table A -4: Uncertainty analysis results for total average Nusselt number, $\overline{Nu}_{Total}$ at an angle of attack, $\alpha = 0°, 30° \& 52°$ for hot condition tests

	$\alpha = 0°$		$\alpha = 30°$		$\alpha = 52°$	
V_∞	$U_{\overline{Nu}_T}$		$U_{\overline{Nu}_T}$		$U_{\overline{Nu}_T}$	
5 m/s	± 28.1	8.06 %	± 30.7	8.4 %	± 37	9.7 %
10 m/s	± 51.4	10.9 %	± 58.1	11.6 %	± 66.3	12.7 %
15 m/s	± 88.9	14.4 %	± 94.9	14.9 %	± 104.8	15.6 %
20 m/s	± 125.5	17.2 %	± 128.7	17.4 %	± 135.1	17.8 %
25 m/s	± 174	20.4 %	± 182.4	20.9 %	± 188.8	21.3 %

APPENDIX (B): CONVERSION FROM LINEAR LOCATION TO ANGULAR LOCATION FOR STREAM-WISE SURFACE

The surface heat flux is calculated at each x-location using the CFD code. The local x-location over the stream-wise front surface is converted into angular position, θ around the surface of the hemisphere. Therefore, the local Nusselt number Nu_θ is computed at each angular position (θ) on the hemisphere front surface. Hemisphere is analyzed at several portions for the conversion from linear to angular position which depend on the configuration as follow;

1. Hemisphere tilt angle, $\alpha = 0°$

   a. $0° \leq \theta \leq 90°$

$$x = \frac{D}{2}\cos(90 - \theta) \qquad \textbf{(B.1)}$$

   b. $90° \leq \theta \leq 180°$

$$x = \frac{D}{2}\sin(180 - \theta) \qquad \textbf{(B.2)}$$

2. Hemisphere tilt angle, $\alpha = 30°$

   a. $0° \leq \theta \leq 60°$

$$x = \frac{D}{2}\cos(60 - \theta) \qquad \textbf{(B.3)}$$

   b. $60° \leq \theta \leq 150°$

$$x = \frac{D}{2}\cos(\theta - 60) \qquad \textbf{(B.4)}$$

   c. $150° \leq \theta \leq 180°$

$$x = \frac{D}{2}\cos(240 - \theta) \qquad \textbf{(B. 5)}$$

3. Hemisphere tilt angle, $\alpha = 52°$

   a. $0° \leq \theta \leq 38°$

$$x = \frac{D}{2}\cos(38 - \theta) \qquad \textbf{(B. 6)}$$

   b. $38° \leq \theta \leq 128°$

$$x = \frac{D}{2}\cos(\theta - 38) \qquad \textbf{(B. 7)}$$

   c. $128° \leq \theta \leq 180°$

$$x = \frac{D}{2}\cos(218 - \theta) \qquad \textbf{(B. 8)}$$

APPENDIX (C): HEAT TRANSFER LOSSES CALCULATIONS THROUGH THE HEMISPHERICAL MODEL

The rate of heat input to the hemispherical model surfaces was maintained by means of external power supply connected to an internal filament heater fixed inside the hemispherical body. Applying the first law over the control volume over the time interval, there should be a balance between the amounts of all energy changes as shown in the following relation (Incropera & DeWitt, 2002).

$$E_{in} - E_{out} = \Delta E_{st} \qquad (\boldsymbol{C.1})$$

In practical condition, the amount of the inflow energy will be divided into three outflow of energy types including system losses, i.e. it's expected that, the outflow energy is not equal to the inflow energy. Hence, there is very strong heat loss from the filament heater by free convection to the enclosure air which is expected to dominant over radiation and conduction heat transfers. Also, a lesser amount of outflow energy by radiation will be exchanged with the hemisphere internal walls. Certainly, there will be certain amount of heat conduction through hemisphere walls but as the thickness is very small (2 mm), it will be ignored.

The out flow energy from the enclosure can expressed as follow

$$q_{out} = q_{conv} + q_{rad} \qquad (\boldsymbol{C.2})$$

In order to estimate amount of the outflow energy of free convection heat transfer inside the hemispherical body we will treat it as an enclosure body. By taking a cross section of the model we will have the following view, as shown in Figure C-1.

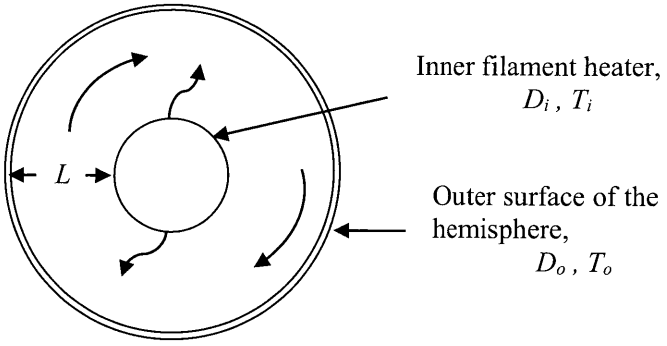


Figure C- 1: Free convection flow in the annular space between hemisphere internal surface and filament heater

A. Free Convection Heat Transfer Case:

The free convection flow is in the annular space between the concentric hemisphere internal wall and filament heater. The flow of heat in annular region is generated if the inner filament heater cylinder is heated and the outer hemisphere surface is at ambient temperature, i.e. ($T_i > T_o$), therefore, fluids will ascends and descends along the annular space. Where, the known data's are as follow:

D_i = 20 mm, D_o = 65 mm, T_i = 70 °C, T_o = 20 °C, L =22.5 mm.

The properties of air from table A-4 (Incropera & DeWitt, 2002), [$T_{film} = (T_i + T_o)/2$ = 318 K]:

$k = 0.02768\ W/m.K, \nu = 17.6 \times 10^{-6}\ m^2/s, \alpha = 25.27 \times 10^{-6}\ m^2/s,$

$\beta = 1/T_{film} = 0.00314\ K^{-1}, Pr = 0.704,$

The free convection heat transfer in the annular space between the concentric cylinders is expressed (Incropera & DeWitt, 2002) as

$$q_{conv} = \frac{2\pi k_{eff}}{\ln(D_o/D_i)}(T_i - T_o) \qquad (\boldsymbol{C.3})$$

Where the *effective thermal conductivity* k_{eff} is the thermal conductivity that a stationary fluid should have to transfer the same amount of heat as the moving fluid. The correlation for k_{eff} is express as (Incropera & DeWitt, 2002)

$$\frac{k_{eff}}{k} = 0.386\left(\frac{Pr}{0.861+Pr}\right)^{1/4}(Ra^*)^{1/4} \qquad (\boldsymbol{C.4})$$

Where

$$Ra^* = \frac{[\ln(D_o/D_i)]^4}{L^3(D_i{}^{-3/5} + D_o{}^{-3/5})^5}Ra_L \qquad (\boldsymbol{C.5})$$

$$Ra_L = \frac{g\beta(T_i - T_o)L^3}{\nu\alpha} \qquad (\boldsymbol{C.6})$$

$$Ra_L = \frac{9.8 \times 0.00314 \times (70-20)(0.0225)^3}{17.6 \times 10^{-6} \times 25.27 \times 10^{-6}} = 39405$$

It follows that

$$Ra^* = \frac{[\ln(0.065/0.02)]^4}{(0.0225)^3(0.02^{-3/5} + 0.065^{-3/5})^5}(39405) = 7199.5$$

Hence

$$\frac{k_{eff}}{k} = 0.386\left(\frac{0.704}{0.861+0.704}\right)^{1/4}(7199.5)^{1/4} = 3.612$$

The effective thermal conductivity is then

$$k_{eff} = 3.612 \times 0.02768 \approx 0.1$$

The heat loss due to free convection is

$$q_{conv} = \frac{2\pi(0.1)}{\ln(0.065/0.02)}(70-20) \approx 26.65\ W$$

B. Radiation Heat Transfer Case:

The heat loss from the filament heater by radiation exchange with the hemisphere internal walls can be expressed (Incropera & DeWitt, 2002) as

$$q_{rad} = \varepsilon A \sigma (T_i^4 - T_o^4) \qquad (\boldsymbol{C.7})$$

$$q_{rad} = 0.85(3\pi(0.0325)^2) \times 5.67 \times 10^{-8}(343^4 - 293^4) = 3.21\ W$$

Therefore the out flow energy from the control surface will be as follow

$$q_{out} = q_{conv} + q_{rad} = 26.65 + 3.21 \approx 29.86\ W$$

As the experimental measurement heat power input to the filament heater was $\approx 35.61\ W$, therefore the estimated lost in power dissipation is almost equal to $((29.86/35.61) - 1) \times 100 \approx 15\ \%$. Although there might be slight heat loss by conduction through the hemisphere walls and within the filament heater, but it was not considered in the calculation as the wall thickness of the hemisphere is very small and is equal to 2 mm.

APPENDIX (D): PUBLICATION PAPER IN THE JOURNAL OF INTERNATIONAL SCIENCE AND TECHNOLOGY CONFERENCE (ISTEC)

Experimental and numerical investigations of flow characteristics over half sphere positioned at unfavorable angle to the flow

Fadhel Abbas S. Al-Afoo; M. Bassam Wafa Nabhan
Department of Mechanical Engineering
College of Engineering, University of Bahrain
Isa Town, Kingdom of Bahrain

Abstract
The airflow characteristic over the smooth wall surface of a heated and tilted hemisphere immersed in a fully developed flow in a test wind tunnel is investigated experimentally and numerically. K-type thermocouples are used to analyze the flow structure for different regions of flow domain around the front and back surfaces of the hemisphere. The investigation is carried at air velocity of 25 m/s with corresponding Reynolds number of $2.5E^{+05}$. The total drag over the hemisphere is experimentally measured in the sub-sonic wind tunnel with electronic balance sensors at the test flow velocity. Corresponding numerical simulations using Fluent software code are also carried out to visualize the flow reversal, separation, horseshoe vortices, and recirculation zone downstream and back of the hemisphere and to validate the experimental results. The heat transfer enhancement exemplified by local Nusselt and Reynolds number on the hemisphere surface is also studied. It is shown that the flow characteristics vary on the stream-wise and back surfaces as the flow becomes unsteady.

Keywords: flow over isothermal hemisphere, forced convection, CFD simulation, heat transfer enhancement.

I. Introduction

The aerodynamic characteristics of a bluff body immersed in a turbulent boundary layer have attracted the attention of many investigators in the field of industrial aerodynamics. Most of the previous studies have concerned two-dimensional bluff bodies, such as normal plates [1-4], inclined plates [5], and semicircular cylinders [6]. The curved shape of a hemisphere structure makes the accurate estimation of the air pressure a difficult task due to Reynolds number effects. Several research papers have focused on this subject. Maher [7] reported that the Reynolds number becomes invariant when Reynolds number exceeds $1.4E^{+06}$. In addition Taylor [8] suggests that, when Reynolds number exceeds $2E^{+05}$ and turbulence intensity exceeds 4%, the pressure distribution becomes Reynolds number independent. Ogawa [9] indicates that for Reynolds numbers ranging from $1.2E^{+05}$ to $2.1E^{+05}$, level of turbulence has little effect upon the mean pressure distribution. Toy and Moss [10] have shown that, with increase of turbulence intensity, separation region and reattachment point move downstream.
Moreover, forced convection heat transfer from isothermal or isoflux external bluff surfaces is an important problem for aeronautic engineers. There are many engineering systems that are modeled using forced convection, such as electronic components on printed circuit boards placed in cabinets, hot-wire anemometers, transformers, heat sinks, thermal spreaders, and heat exchanger design. Several researchers have investigated forced convection from isothermal axi-symmetric bluff bodies, such as spheroids (Beg [11]), cylinders (Refai and Yovanovich [12]), and discs (Wedekind and Kobus [13]) using a variety of predictive methods as reviewed in (Yovanovich [14]). However, the number of studies from steady laminar and turbulent forced convection is limited on hemispherical bluff bodies, with most research restricted to experimental studies (Igarashi [15, 16]) leading to empirical correlations or detailed numerical procedures (Wong and Chen [17]).
The objective of this paper is to investigate air flow characteristics around a heated isothermal surface of a hemispherical body tilted at 52 degrees to the free stream air flow direction. Having the flow field, local pressure and heat flux distribution, recirculation zones, flow separation region, and reattachment locations will be investigated at Re $= 2.5E^{+05}$ using experimental measurements and numerical simulation.

II. Experimental Work

Experimental investigations are performed in a sub-sonic wind tunnel located in the Fluids Laboratory in the Mechanical Engineering Department at Bahrain University. The tunnel cross section is a transparent 150 mm square

working section with an overall length of 450 mm. Air is drawn in through a variable speed fan located at the discharge end of the tunnel to minimize turbulence inside the working section. A honeycomb type flow straightener and 9.4:1 contraction ratio ensure well developed air flow through the working section. An Electronic Balance and software, allows full electronic monitoring and recording of the measured drag and lift on the software mimic diagram of a suitable PC. The model being tested can be rotated on the mounting and the angle of rotation measured electronically. The operating range is nominally 0 – 32 m/s with no model installed in the working section. The maximum velocity achievable in the test section varies with the model type and the blockage created by the model. The air velocity is adjusted from the software by altering the fan speed. Fan speed is set as a percentage of the maximum speed, between 0% and 100%. The corresponding static head in the tunnel given as the differential head between the tunnel and atmosphere and air velocity in m/s are displayed on the software mimic diagram.

The experimental setup consists of a smooth suspended hemisphere in the test section tilted at 52 degrees to the vertical y-direction. The location of the model in the test tunnel and the reference coordinate system are shown in FIG.1.The experimental setup consists of a smooth immersed hemisphere of diameter 6.5 cm in the test section of the wind-tunnel. To avoid wall interference, the model is supported from the rear with an aluminium rod of 0.05D, where D is the diameter of the hemisphere. In addition, the tunnel blockage was overcome by reducing the Mach number value to below 0.1 as stipulated by Naumann (1953) (E. Achenback [18]). At, for instance, the maximum Reynolds number, which was obtained in the tunnel test section, the Ma number was even lower than 0.05.

A filament heater attached to an external power supply and embedded inside the hollow cavity of the hemisphere is used to raise the hemisphere surface temperature isothermally to 70 ^{O}C. A total of fifteen (15) K-type thermocouples are embedded in the front and back surfaces of the hemisphere and attached to a digital temperature recorder to detect the temperature readings at 25 m/s and various test air flow velocity. The temperature readings are taken in the stream-wise and back surfaces of the hemisphere as shown in FIG. 2.

III. Results

The flow characteristics of the 52° tilted model hemisphere are determined at the test air flow velocity. The total drag force is measured using an Electronic Balance of the wind tunnel and software on a mimic diagram of a suitable PC. The measurements were taken for cold model temperature of 20 °C and hot isothermal temperature of 70 °C. These results are shown in FIG.3. The total drag coefficient, Cd at the mean test velocity in the duct is calculated using the relationship;

$$Cd = \frac{\Sigma DT}{0.5\rho V^2 A \sin\alpha} \qquad (1)$$

The results of drag coefficient, Cd for cold and hot conditions are plotted against Reynolds numbers, Re as shown in FIG.3. In the cold condition the drag coefficient increases with Re up to Re = 1.5E^{05} and stays almost constant for larger Re values. Perhaps, this is a result of turbulent flow, boundary layer separation and reverse flow due to adverse pressure gradient and large pressure drag taking place at the same point on the upper surface of the hemisphere. Similar trend, however with larger values of Cd are noted for the hot hemisphere with invariant Cd values at Re = 2E^{+05} and above. This perhaps is attributed to the larger boundary layer thickness for the heated hemisphere surface. As a result, Cd is affected by many factors namely; the fluid viscosityμ, the flow velocity gradient $(\partial u/\partial y)_s$, and the thermal boundary layer temperature gradient $(\partial T/\partial y)_s$. An increase on the surface temperature will give rise to larger values of μ and a decrease in $(\partial u/\partial y)_s$ due to buoyancy effect for a mixed convection mode. Perhaps the increase in the viscosity is predominant factor in the drag equation. And thus the skin friction drag increases on the surface leading to larger total drag in comparison to the hemisphere surface cold condition. The total drag coefficient Cd for the inclined hemisphere can be written in the following form;

$$C_d = \frac{\Sigma(\Delta P + \tau)}{\frac{1}{2}\rho V^2 A \sin\alpha} = \frac{\Sigma(\Delta P + \mu\frac{\partial u}{\partial y})}{\frac{1}{2}\rho V^2 A \sin\alpha} \qquad (2)$$

The temperature distributions on the stream-wise and back cover of the hemisphere were measured at approximately equal locations using 15 K-type thermocouples connected to a digital temperature recorder. The temperature readings are taken at various air stream velocities, namely 5, 10, 15, 20, and 25 m/s with corresponding Reynolds numbers of 5E^{+04}, 1E^{+05}, 1.5E^{+05}, 2E^{+05}, and 2.5E^{+05}. The thermocouple locations are shown in FIG.2 (a),and (b).The temperature

readings are made dimensionless ($\Delta T/T_{atm}$) with respect to the hemisphere isothermal temperature T_s, of 70 °C and the wind tunnel temperature T_{atm}, of 20 °C.

FIG.4 shows the stream-wise temperature variations on the front hemisphere surface at increasing air flow velocities of 5, 10, 15, 20, and 25 m/s with corresponding Reynolds numbers of $5E^{+04}$, $1E^{+05}$, $1.5E^{+05}$, $2E^{+05}$, and $2.5E^{+05}$. It is noticed that the temperature variations ΔT increases at larger Re values.

This can be explained, as Re increases the dissipation of kinetic
energy on the surface increases.

At each Re value the temperature variation on the surface boundary of the hemisphere also changes. The boundary layer separation and reverse flow takes place due to a strong pressure gradient in the vicinity of the trailing front surface of the hemisphere at point 6 as illustrated in FIG.2 (a), where the velocity gradient $(\partial u/\partial y)_s \approx 0$ and ΔT is small due to low velocity magnitude , large boundary layer thickness and thus lower cooling effect on the surface ($\Delta T = Ts - T_{thermocouple}$). However on the leading edge of the front surface of the hemisphere, at point 1 of FIG.2 (a), the flow doesn't separate giving higher variations in ΔT due to effective cooling of the thermocouple tips as a result of thin boundary layer and strong flow momentum. At the stagnation point 3, ΔT is at its lowest value as shown.

Similar temperature variations trend is shown in FIG.5 on the back end cover. The lowest variation in ΔT takes place at $Re = 5E^{+04}$ and increases at larger Re values. At point 17, near the center of the hemisphere back plate, ΔT is at its lowest values for all Re values, perhaps due to lowest air flow velocity in this vicinity of the flow domain. The temperature variation increases from point 16 to 14 due to increased flow recirculation in this region. ΔT remains almost invariable towards the trailing edge from point 18 to 21. It is also noted in this graph and by comparison with the stream-wise temperature variation values; the rear surface of the hemisphere is also effective in enhancing the heat transfer mode.

IV. Numerical Results

Numerical simulation is performed using a discretized 2-dimensional Fluent code to study the flow field, pressure distribution, and heat transfer around an immersed mounted hemisphere in more detail; the numerical simulation is related to the experimental investigations performed on the tilted hemisphere in a sub-sonic wind tunnel at 52° to the vertical as shown in the schematic diagram in FIG.1. The origin of the coordinate system is located in the center of the hemisphere. Measured in units of the reference length of the flow problem (D is the diameter of the hemisphere), the dimensions of the computational domain are (x, y, z) = (0.15, 0.15, 0.45), and for the results presented we used a computational configuration that contained some 54787 cells, 112743 faces and 57956 nodes distributed over 6 face zones. Velocity inlet and pressure outlet were specified at the inflow and outflow boundaries, while top and bottom boundaries of the computational domain and the hemisphere front and back surfaces as wall. The inflow boundary conditions were chosen to match the velocity and turbulence profiles measured during the wind tunnel experiments. Outflow boundary conditions were chosen to maintain constant longitudinal rate of change of all dependent variables (constant slope). The governing equations of incompressible turbulent 2-D flow are solved using finite volume discretization method. To solve these equations numerically, SIMPLE algorithm which treats the coupling between velocity and pressure in the flow field is employed. Control volume cells for velocity components are staggered with respect to the main control volume cells. The Realizable κ - ε Turbulence model, which provides superior performance for flows involving boundary layers under strong adverse pressure gradients, separation, and recirculation, is used to study the numerical computation of the turbulent flow field around the hemisphere. The hemisphere is mounted on a hanger and its distance from the inlet plane in the computational domain is about 3.5 D. Non-uniform structured grid is used to discretize the governing equations. FIG.6 shows the grid generated for the numerical simulation. Finer grids are used adjacent to the obstacle where the velocity gradients are large and the recirculation is expected to develop in these regions. The grid spacing is large far from the hemisphere where the flow is without any considerable variation.

The numerical simulations were used to determine heat transfer and fluid flow in the region surrounding an isothermal hemisphere. The obstacle was modeled using four isothermal, no slip planes in contact with the fluid regions for the stream-wise, back, and top and bottom surfaces. A uniform inlet velocity U_∞ and uniform free stream temperature T_{atm} were applied at the upstream domain boundary, T_{atm} and atmospheric (zero) pressure at the downstream boundary and T_{atm} at the top and bottom wall boundaries. The hemisphere and ambient air temperature were set to T_s = 70 °C and T_{atm} = 20 °C respectively, and all air flow properties were evaluated at a mean film temperature of 318 K. In each of

the CFD simulations, the tilt angle of the obstacle was kept constant at 52° to the vertical. Numerical solution is simulated for Re = $2.5E^{+05}$. Converged solution is obtained where the values of residuals were less than 10^{-6}.
FIG.7 shows the mean centerline pressure coefficient, Cp distribution plotted versus the stream wise direction on the smooth tilted hemisphere at Re = $2.5E^{+05}$. The numerical simulations display negative pressure coefficients over the downwind face of the obstacle up to 15° angle (67° from vertical). Above this angle, the pressure coefficients indicate positive values up to 80° angle. Afterwards, the pressure coefficient displays again negative values over the upwind face of the hemisphere from 80° to 180° angle. The negative pressures gradually recover and reach a stable value at about 150° which indicates the point of separation on the trailing edge and beginning of the wake region. The separation point can also be observed in the velocity contour plot in FIG.8, the snap shot photo in FIG.9, and the shear stress plot in Fig.10. Moreover, in FIG.10, the multi-peaks phenomenon depicted at the beginning of the wake region at $\theta \approx 150°$ in the trailing edge suggests that transition of separated free shear layer occurred and that a separation bubble is formed at this stage, the first and second peaks indicate the locations of fore-separation and the reattachment/rear-separation. With increasing Reynolds number the magnitude of the peak suction continuously increases whilst, the wake suction and hence the overall drag coefficient decrease. Numerically computed drag coefficients are 0.9, 1.45 and 2.33 at Re = $5E^{+04}$, $1.5E^{+05}$ and $2.5E^{+05}$ respectively. Experimentally measured values of drag coefficient for the isothermally heated obstacle at these Re values are approximately; 0.4, 0.9 and 1. The differences noted are most likely due to the quality of the free stream and three dimensional effects (vortex shedding, etc.). There are several problems with our simulation: we are modeling a steady flow, even though the actual physical flow is unsteady; and we are using a turbulence model instead of resolving all the small eddies of the turbulent flow. Another significant source of error in our calculations is that the CFD code is run with turbulence turned on in order to reasonably model the wake region, which is turbulent; however the boundary layer on the surface of the hemisphere is still laminar. The predicted location of the separation point downstream of the top of the obstacle is more in line with turbulent boundary layer separation, which does not occur until much higher values of Reynolds number. The bottom line is that CFD codes have a hard time in the transitional regime between laminar and turbulent flow, and when there is a mixture of laminar and turbulent flow in the same computational domain. In fact, most commercial CFD codes give the user a choice between laminar and turbulent - there is no "middle ground." In the present calculations, we model the boundary layer as turbulent, even though the physical boundary layer is a mixed flow; it is not surprising, then, that the results of our calculations do not agree well with experiment. If we would have instead specified laminar flow over the entire computational domain, the CFD results would have been even worse (less physical). The maximum negative value of the pressure coefficient is noted at the hemisphere leading edge, where the flow velocity and shear stress are maximum, and the maximum positive value of Cp is observed approximately at $\theta = 45°$ (stagnation point) as depicted in FIG.7, the shear stress x-y plot in FIG. 10 and the velocity profile contour plot at Re = $2.5\ E^{+05}$ shown in FIG.8. Cp is minimum at the point of separation $\theta \approx 150°$.
The effectiveness of the experimental results to predict the rate of heat transfer from an isothermally heated hemisphere tilted at 52° to the vertical is assessed through comparison with numerical predictions using the finite volume model explained earlier. The heat transfer rate is calculated at Re = $2.5E^{+05}$, where Re is based on the approach velocity, the characteristics length and the kinematic viscosity at the free stream air temperature in the test section. The hemisphere and the ambient air temperature were set at Ts = 70° and T_{atm} = 20°, and all properties were evaluated at a film temperature of 318 K. As the turbulent boundary layer grows in thickness on the surface of the obstacle, the local rate of heat transfer Q_x and thus the local heat transfer coefficient, h_x will decrease. This relation can be expressed mathematically as;

$$Q_x = h_x (T_s - T_{atm}) \qquad (3)$$

$$Nu_x = \frac{hx\ x}{k} = \left\{\frac{Qx}{Ts - Tatm}\right\} \frac{x}{k} \qquad (4)$$

The local Reynolds Number is defined at each x location by;

$$Re_{(x)} = Re\ (x) \qquad (5)$$

In polar coordinates;

$$Nu(\theta) = \left\{\frac{Q\theta}{Ts - Tatm}\right\} \frac{D \sin(\theta + 52)}{2k} \quad (6)$$

$$Re(\theta) = Re\,(D/2)\,\sin(\theta + 52^{o}) \quad (7)$$

The surface heat flux is calculated at each x-location using the CFD code. The x-location is converted into angular position, θ around the hemisphere front surface. The local Nusselt number $Nu_{(\theta)}$ and Reynolds number $Re_{(\theta)}$ are computed at each angular position (θ) on the hemisphere front surface and linear location (x) on the hemisphere back surface for each wind tunnel test velocity. FIG.11 shows $Nu_{(\theta)}$ versus $Re_{(\theta)}$ plot at Reynolds number, $2.5E^{+05}$ on the front stream-wise direction. A polynomial best fit trend line of order 6^{th} is plotted to show behavior of the local heat transfer rate along the front surface. It is observed that heat transfer rate is largest on the leading edge, $\theta \approx 0.13^{o}$ ($Re_{(\theta)}$ = 6440 and $Nu_{(\theta)}$ = 630.8) due to maximum velocity magnitude and large kinetic energy dissipation and decreases afterwards as the flow moves upwards to the trailing edge. At $\theta \approx 127^{o}$, approximately 180° from the vertical y-angular position taken in the clock-wise direction ($Re_{(\theta)}$ = 0 and $Nu_{(\theta)}$ = 400), the rate of heat transfer starts to drop sharply until the separation point where heat transfer commences to fluctuate into low and high peaks of heat transfer due to Van Karman vortex and unsteady flow behavior. On the front stream-wise direction, the minimum value of heat transfer is observed in the separation zone at $\theta \approx 149.8^{o}$ ($Re_{(\theta)}$ = 3058.5 and $Nu_{(\theta)}$ = 59.85). Moreover, low values of heat transfer are noticed on the leading edge on and around the stagnation point $\theta \approx 45 \pm 3^{o}$ ($Re_{(\theta)}$ = 8001-8102 and $Nu_{(\theta)}$ = 272-296).

FIG.12 depicts the local heat transfer rate on the back surface of the hemisphere. It is observed that heat transfer is almost zero at the center of the back surface (x, y) = (0, 0) and increases in the opposite directions reaching a maximum value just before the tips of both the leading and trailing edges at $(x, y)_{leading}$ = (-24.93, -18.96) mm where, $Re_{(x)}$ = 6250 and $Nu_{(x)}$ = 240, and $(x, y)_{trailing}$ = (24, 19) mm, where $Re_{(x)}$ = 6300 and $Nu_{(x)}$ = 140 respectively as shown. It is also noticed that the rate of heat transfer on the lower surface from the center towards the leading edge has shown higher heat transfer rate in comparison with the upper surface from the center towards the trailing edge. The above behavior is due to strong recirculation flows and larger velocity magnitudes on the leading back surface compared to the trailing surface. The polynomial trend line shown on FIG.12 indicates that the local heat transfer rate on the back surface increases with increasing $Re_{(x)}$.

V. Conclusions

The main flow structures and forced convection heat transfer rate from a tilted isothermal hemisphere immersed in air flow in a subsonic wind tunnel are determined using experimental and numerical schemes. The results presented are for Reynolds number, $Re = 2.5E^{+05}$ show that:

(1) The Realizable κ - ε Turbulence model slightly overestimates the stream-wise total drag over the hemisphere to the values determined experimentally. The variations are a result of the unsteady flow behavior and 3-D effects on the obstacle, which could not be catered for in the 2-D CFD simulation.
(2) The numerical investigation has shown that maximum positive value of pressure coefficient, Cp is observed at the stagnation point, $\theta = 45^{o}$ and minimum value at the point of separation $\theta \approx 150^{o}$.
(3) The simulation has shown that the transition of separation flow occurs on the trailing surface of the hemisphere at $\theta \approx 150^{o}$ where the drag is minimum.
(4) The experimental work and numerical simulation have shown that the heat transfer rate is large on the front leading surface of the hemisphere. This occurred as a result of larger local flow velocity, which generates a thin boundary layer and thus more effective cooling on this zone. However on the trailing surface, the overall heat transfer is lower due to low velocity magnitude and the commencement of the separation zone at $\theta \approx 150^{o}$. Similar behavior on heat transfer rate has also been noted on the back surface of the hemisphere.
(5) The tilted hemisphere configuration under study has shown that the front and back surfaces are effective in heat transfer enhancement and they can complement each other.
(6) The numerical simulation has shown that the minimum value of heat transfer is observed in the separation zone at $\theta \approx 150^{o}$ on the front stream-wise direction. The separation zone comprised of different minima and maxima peaks of heat transfer as a result of flow separation, recirculation and unsteady flow conditions.

(7) The effective heat transfer on the hemisphere surface can be optimized by studying flow at different inclinations and the results can be compared afterwards. Also different materials and surface finish can investigated.

ACKNOWLEDGMENT

The author wishes to acknowledge the financial support of the Deanship of Research in the University of Bahrain under research project grant no.30/2011. The author appreciates this support and the comments of the reviewers.

REFERENCES

[1] M.C. Good and P.N. Joubert, 1968, The form drag of two dimensional bluff plates immersed in a turbulent boundary layer, J. Fluid Mech., 3, pp. 547-582.

[2] K.G. Range Raju, J. Loeser and E.J. Plate, 1976, Velocity profiles and force drag for turbulent boundary layer along smooth and rough flat plates, J.Fluid Mech., pp. 383-399.

[3] I.P. Castro, and J.E. Fackrell, 1978, a note on two-dimensional fence flows, with emphasis on wall constraint, J. Ind. Aerodyn., 3, pp.21-38.

[4] H.Sakamoto, M. Moriya and M. Arie, 1975, a study on the flow around bluff bodies immersed in turbulent boundary layers, Part 1, Bull. Jpn. Soc. Mech. Eng., 18, pp. 1126-1133 (in Japanese).

[5] H.Sakamoto, M. Moriya and M. Arie, 1977, a study on the flow around bluff bodies immersed in turbulent boundary layers, Part 2, Bull. Jpn. Soc. Mech. Eng., 20, pp 71-78 (in Japanese).

[6] H.Sakamoto, M. Moriya and M. Arie, 1977, A study on the flow around bluff bodies immersed in turbulent boundary layers, Part 3, Trans. Jpn. Soc. Mech. Eng., 42, pp. 3224-3232 (in Japanese).

[7] F.J. Maher, 1965, Wind loads on basic dome shapes, J. Struct. Div. ASCE ST3, pp. 219-228.

[8] T.J. Taylor, Wind pressures on a hemispherical dome, 1991, J. Wind Eng. Ind. Aerodn. 40, pp. 199-213.

[9] T. Ogawa, M. Nakayama, S. Murayama, Y. Sasaki, 1991, Characteristics of wind pressures on basic structures with curved surfaces and their response in turbulent flow, J. Wind Eng. Ind. Aerdyn. 38, pp. 427-438.

[10] N. Toy, W.D. Moss, E. savory, 1983, Wind tunnel studies on a dome in turbulent boundary layers, J. Wind Eng. Ind. Aerdyn. 1, pp. 201-212.

[11] Beg, S.A., 1975, Forced convection mass transfer studies from spheroids, Warme-und Stoffubertragung, 8, pp. 127-135.

[12] Refai-Ahmed, G., and Yovanovich, M. M., 1970, Experimental study of forced convection from isothermal circular and square cylinders and toroids, ASME J. Heat Transfer, 119, pp. 70-79.

[13] Wedkind, G. L., and Kobus, C. J., 1996, Predicting the average heat transfer coefficient for an isothermal vertical circular disc with assisting and opposing combined forced and natural convection, Int. J. Heat Mass Transfer, 39 , No. 13, pp. 2843-2845.

[14] Yovanovich, M. M., and Vanoverbeke, C. A., 1988, Combined natural and forced convection heat transfer from isothermal spheres, paper No. 88-2618, AIAA thermo-physics, Plasama-dynamics and Lasers conference, San Antonio, TX.

[15] Igarashi, T., 1985, Heat transfer from a square prism to an air stream, Int. J. Heat Mass Transfer, 28, No.1, pp. 175-181.

[16] Igarashi, T., 1986, Local heat transfer from a square prism to an air stream, Int. J. Heat Mass Transfer, 29, No.5, pp. 774-784.

[17] Wong, K. L., and Chen, C. K., 1986, Finite element solutions for laminar flow and heat transfer around a square prism, Journal of the Chinese institute of Engineers, 9, No.7, pp. 605-615.

[18] E. Achenback, 1972, Experiments on the flow past spheres at very high Reynolds numbers, J. Fluid Mech., vol.54, part 3, pp. 565-575.

Nomenclature

A	Projected surface area of hemisphere, m^2
Cd	Total drag coefficient
D_T	Total drag force, N
V	Free air stream velocity, m/s
P	Pressure, Pa
T_{atm}	Wind tunnel temperature, °C
T	Temperature recorded by thermocouples during tests, °C
T_s	Hemisphere isothermal temperature, °C
Re	Reynolds number in the test section
Re_x	Local Reynolds number
Q_x	Local rate of heat transfer, W
h_x	Local heat transfer coefficient, $W/m^2.K$
x	x-location on the surface of the hemisphere
θ	Angular location on stream-wise surface
ρ	Air flow density, kg/m^3
α	Hemisphere inclination with the horizontal
ΔT	$(T_s - T)$ °C
μ	Air dynamic viscosity, kg/m.s
$(\partial u/\partial y)_s$	Velocity gradient on the surface, s^{-1}
$(\partial T/\partial y)_s$	Thermal boundary layer temperature gradient, °C/m
τ_{wf}	Shear stress along front hemisphere surface, Pa

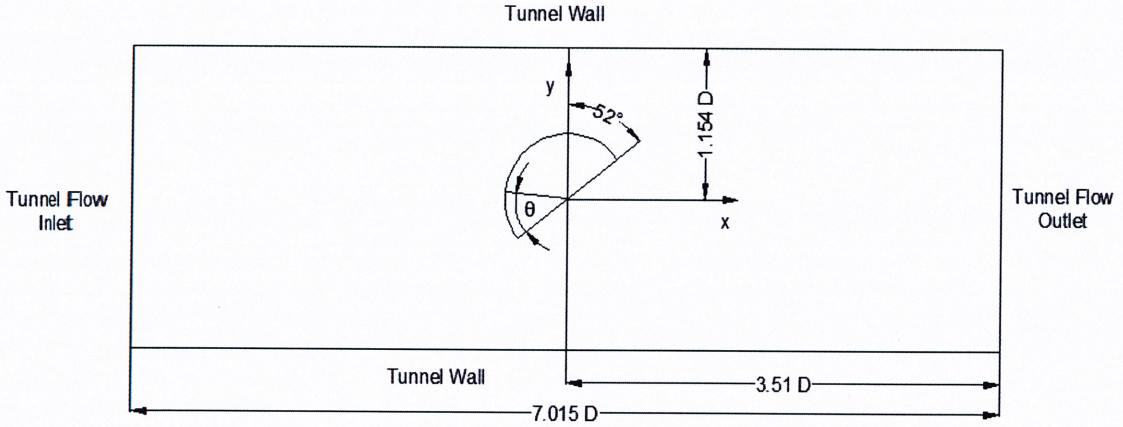
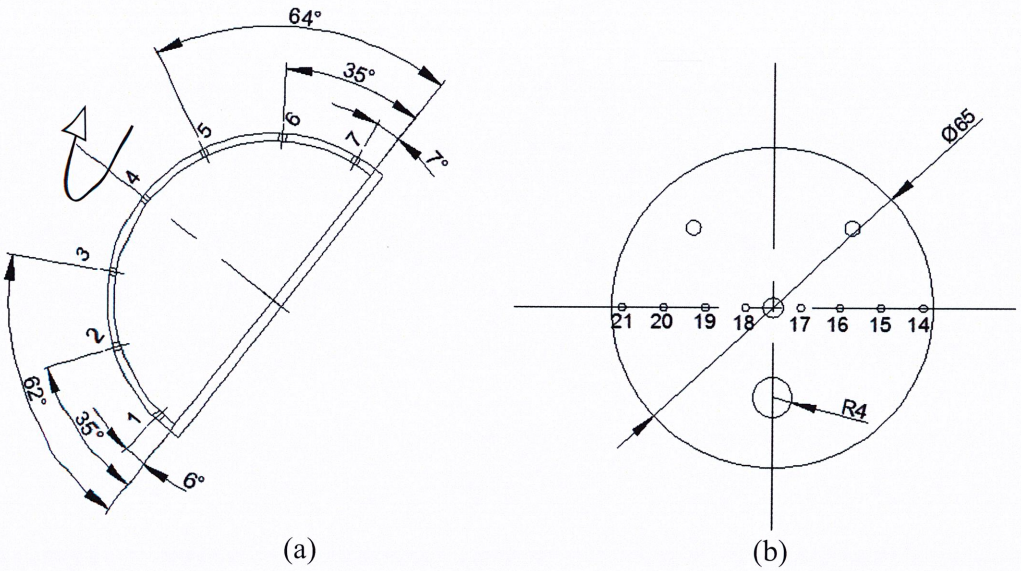


Fig.1 Schematic of the model hemisphere in the test tunnel with reference coordinates system



(a) (b)

Fig.2 Hemisphere at 52 degrees tilt angle showing thermocouple positions
(a) Thermocouples location in stream-wise direction, and (b) Back end cover

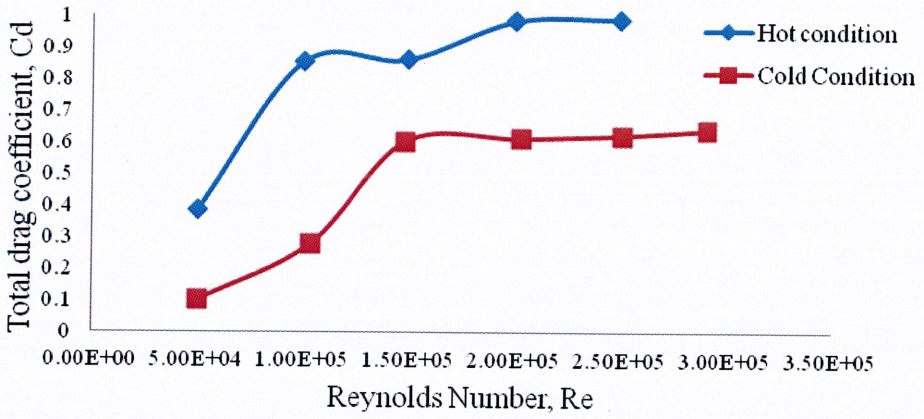


Fig.3 Drag coefficients for hemisphere versus Reynolds number at cold and hot condition

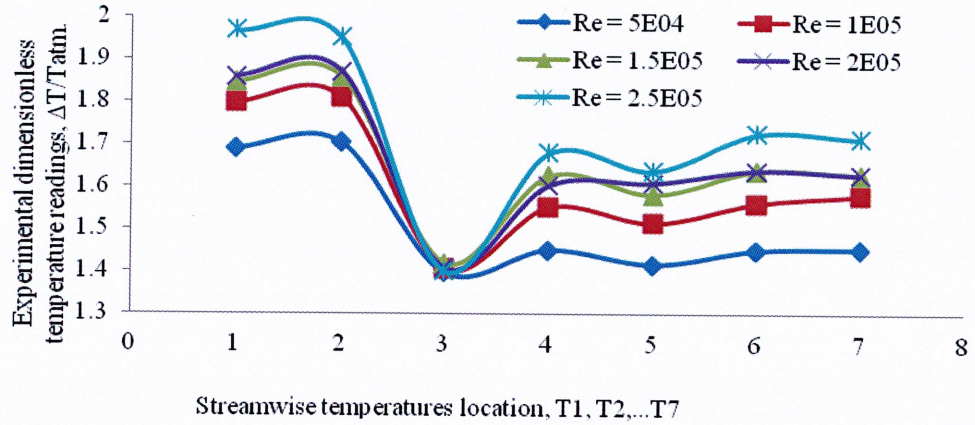


Fig.4 Frontal hemisphere stream-wise dimensionless temperature variations at 52 deg. tilt angle

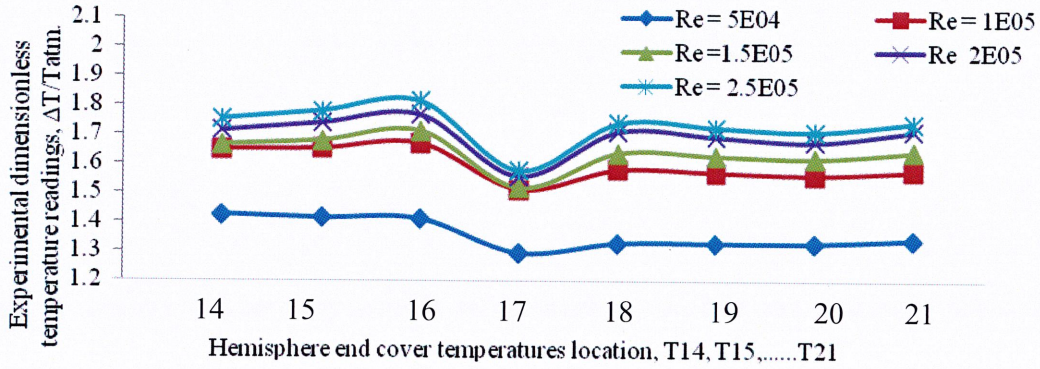


Fig.5 Hemisphere back end dimensionless temperature variations

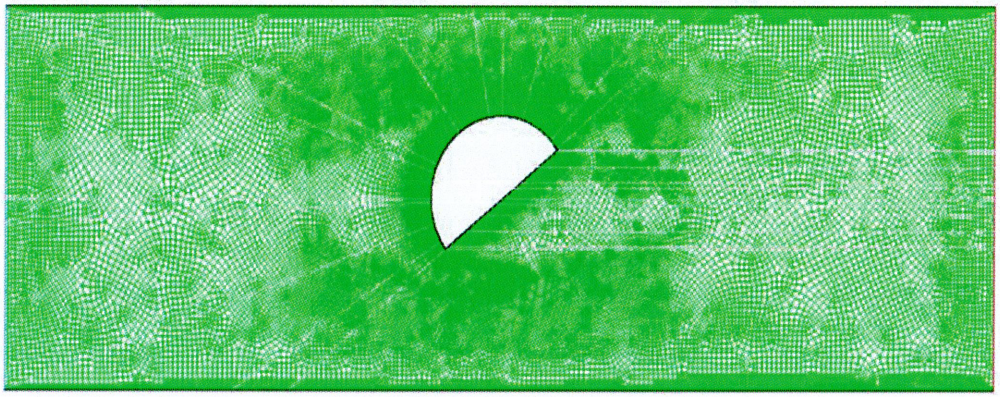


Fig.6 Grid arrangement

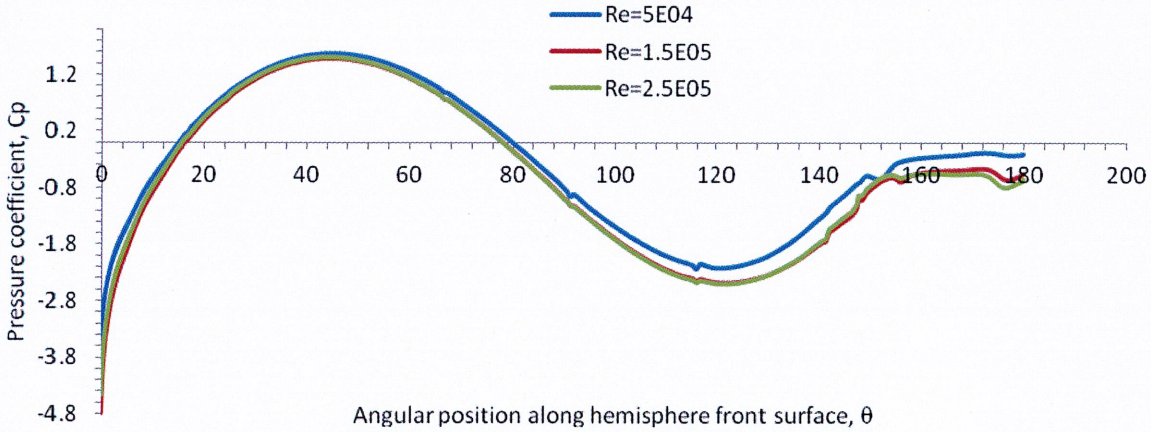


Fig.7 Pressure Coefficient, Cp along hemisphere front surface

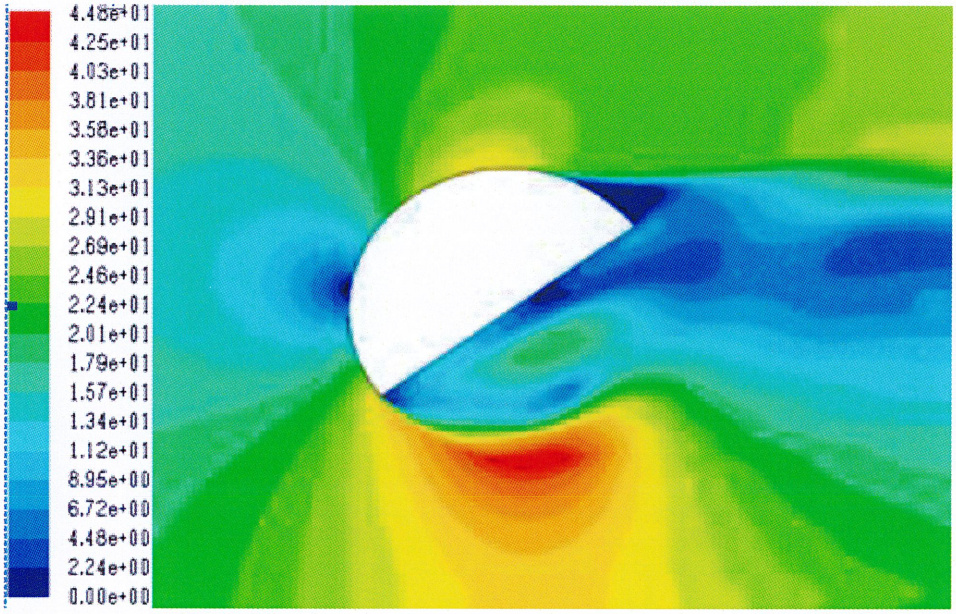


Fig.8 Velocity magnitude contour plot at Re = 2.5 E^{+05}



Fig.9 Smoke generated flow around hemisphere showing separation flow on the trailing surface, Re = $2.5E^{+05}$

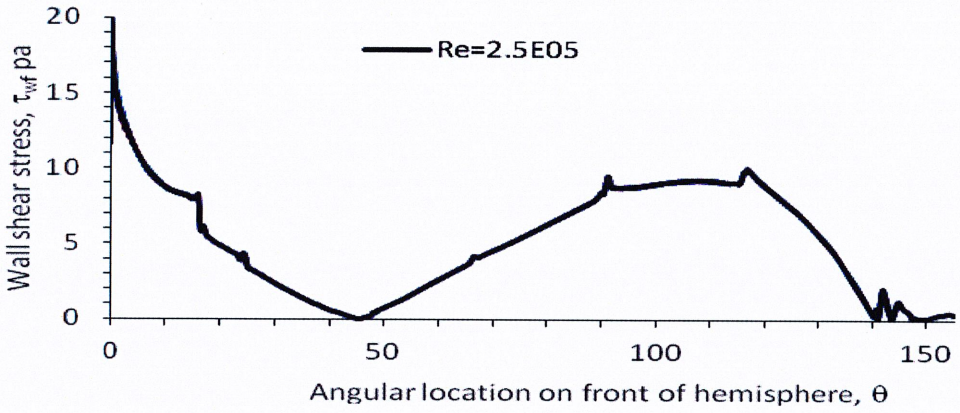


Fig.10 Shear stress, τ_{wf} along hemisphere front surface

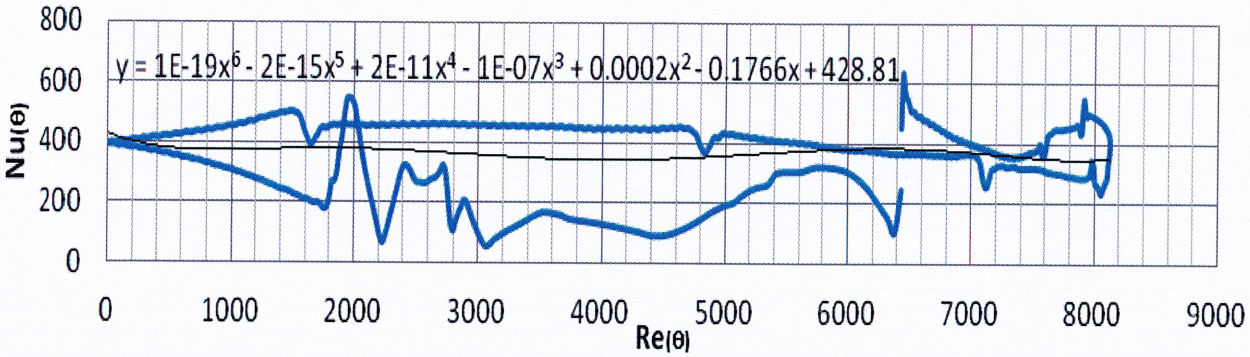


Fig.11 Local Nusselt and Reynolds numbers on front of hemisphere, Re = $2.5E^{+05}$

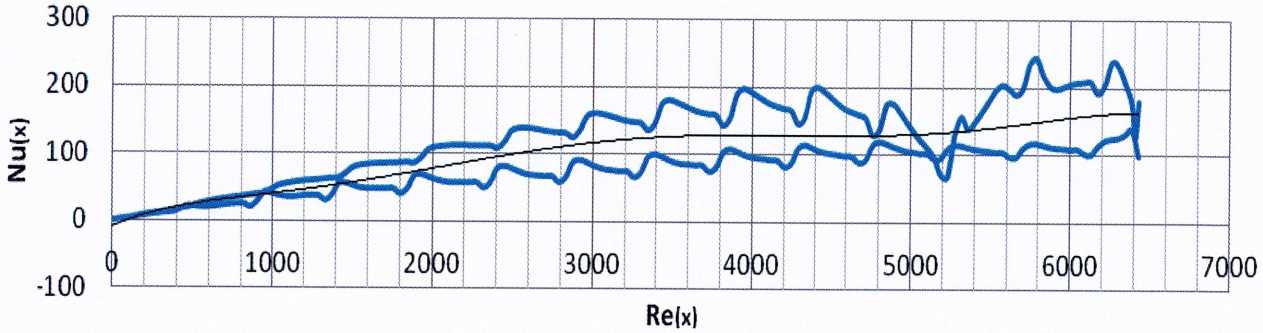


Fig.12 Local Nusselt and Reynolds numbers on back of hemisphere, Re = $2.5E^{+05}$

جامعة البحرين
المكتبة
LIBRARY
UNIVERSITY OF BAHRAIN

ملخص البحث

تم التحقيق تجريبيا و عدديا في خصائص تدفق الهواء والأنتقال القسري للحرارة بالحمل على سطح جدار املس من الالمنيوم من جسم نصف كروي مسخن ومدور, ومغمور في تدفق هواء متكامل في نفق تجارب الرياح.

تمة دراسة الجسم النصف كروي عند ثلاث درجات ميلان مختلفة, بالتحديد ($\alpha = 0°, 30°$ و $52°$), مائلة عموديا على المحور الصادي (ص). و انجز التحقيق عند سرعات تدفق هواء تتراوح من 5 إلى 25 م/ث, بزيادات 5 م/ث. تتضمن التجارب المختبرية على طريقة الحفاظ على تدفق حراري ثابت على أسطح نصف الكرة بواسطة جهاز ناقل للطاقة وسخان ملفوف بسلك كهربائي. وتم إستخدام مزدوجات حرارية من نوع (K) لتحليل تركيبة التدفق عند مناطق مختلفة من مجال التدفق حوالي السطح الامامي والخلفي من المجسم. وتم عرض النتائج التي تم الحصول عليها على هيئة توزيع درجات الحرارة اللابعدية على كل من السطح الأمامي في الأتجهان (الطولي والعرضي), وعلى السطح الخلفي. تم ايضا قياس إجمالي قوى السحب والرفع تجريبيا على مدى نصف الكرة في نفق الهواء بواسطة اجهزة استشعار إلكترونية عند سرعة تدفق الهواء. وقد أظهرت نتائج معاملات السحب والرفع الاعتماد على ميلان نصف الكرة (α). تم ايضا قياس قيمة الضغوط في المنطقة الخلفية من نصف الكرة في نفق الهواء بواسطة مقياس ضغط الكتروني. تصبح نتائج تغيرات الضغط ذو اهمية عند ارتفاع عدد الرينولدز, $Re \leq 2\times 10^5$. وتم أيضا انجاز تقنية تصوير تدفق الدخان من أجل الحصول على معلاومات نوعية بشأن هيكلية التدفق المتاخم لأسطح النموذج.

تم أعتماد نموذج عددي ثنائي الأبعاد (2D) لديناميكية السوائل الحسابية (CFD) لمحاكات مجال تدفق السائل وانتقال الحرارة, وتصوير إنعكاس التدفق, الأنفصال, دوامات حدوة الحصان, ومنطقة إعادة التدوير عند السطح الخلفي من نصف الكرة, وللتحقق أيضا من صحة النتائج التجريبية. وتبين أن خصائص التدفق تختلف عند الأتجاه الطولي من السطح الأمامي والسطح الخلفي كلما أصبح التدفق انتقالي وغير مستقر. ووجد ايضا كلما زاد عدد الرينولذ, يزداد في المقابل عدد النسلت المحلية على السطحان الأمامي والخلفي. وتبين أن عدد النسلت المحلية والمتوسطة تعتمد بشكل كبير على قدوم سرعة تدفق الهواء. ووجد ان إجمالي معدل إنتقال الحرارة على أسطح نصف الكرة (الأمامي و الخلفي) يعزز كلما زادة زاوية الميل للمجسم (α). حيث وجد ان الزيادة تكون حوالي (6% ~8.3%) و (5% ~ 9%) بالمقارنة مع زوايا الميل ($\alpha = 0°, 30°$), على التوالي. وتم إنجاز مقارنة بين نتائج متوسط عدد النسلت التجريبية والعددية على السطح الكلي لنصف الكرة, وتتطابق النتائج بشكل وثيق تحديدا عند نطاق عدد الرينولدز, بين ($2\times 10^5 \leq Re \leq 10^5 \times 2.5$). وتم أيضا التحقق من النتائج التي تم الحصول عليها في عمليات المحاكات العددية من خلال المقارنة مع العلاقات المنشورة.